Politecnico di Torino

Politecnico di Torino

Master's Degree in Energy and Nuclear Engineering
Academic Year 2022 - 2023
Graduation session march - april 2023

Hydrogen fuel cell vehicles (HFCVs)

Fire scenarios within confined spaces: road tunnels

Supervisor:
Prof. Davide Papurello

Candidate:
Andrea Pistillo
290815

A nonno Raffaele,

volato in cielo solo pochi giorni
prima di questo traguardo, al
quale non sarebbe voluto e
dovuto mancare.

Abstract

In the current and future context, vehicles powered by alternative fuels are of increasing interest, being an option for the future zero-emission transport sector. In particular, hydrogen fuel cell vehicles (HFCVs), which represent the latest generation of electric vehicles, are spreading very rapidly in recent years. This revolutionary technology is powered by the chemical reaction that occurs between hydrogen and oxygen within fuel cells, rather than the typical combustion of fossil fuels that occurs in conventional engines. The issues related to safety and management of HFCVs connected risks must be thoroughly studied, especially in confined spaces, such as road tunnels, and indoor car parks. In fact, while in open environments an accidental hydrogen release is rapidly dispersed in the air, causing no particular safety concerns, in restricted ones the accumulation of hydrogen could lead to an explosion, in case of a delayed ignition, or to a hydrogen fire if an immediate ignition occurs. In the present study computational fluid dynamics (CFD) simulations of a hydrogen fire inside a road tunnel are carried out using PyroSim, a software program based on the Fire Dynamic Simulator (FDS) approach. The circumstances caused by the fire of a HFCV are critically analysed taking into consideration several parameters such as the heat release rate (HRR) during the burning process, the temperatures reached in the road tunnel, the visibility and concentration of hot smokes. Subsequently, this scenario is compared to the one produced by a traditional fossil fuels powered car, to make reference in the analysis of fire related safety hazards. In the end some mitigation techniques, such as longitudinal ventilation strategies, are investigated to try to reduce the critical issues triggered by the hydrogen fire inside the road tunnel.

Ringraziamenti

Desidero innanzitutto ringraziare il mio relatore, il professor Davide Papurello, per la grande disponibilità dimostratami in questi mesi, durante i quali mi ha fornito un prezioso supporto concedendomi sempre piena fiducia.

I ringraziamenti più emozionati e commossi vanno alla mia famiglia. Senza l'affetto di mamma, i consigli risoluti di papà e la premura di Gianna, sarebbe stato impossibile raggiungere questo traguardo. Spero di avervi reso, e di rendervi sempre, orgogliosi di me.

Ringrazio Roberta, entrata quasi per caso nella mia vita, della quale è ora una componente imprescindibile, sostenendomi in tutto ciò che faccio.

"Non sei fregato veramente finché hai da parte una buona storia e qualcuno a cui raccontarla". Un grazie speciale a Peppe, Virginio e Gabriele, ai quali ho raccontato in questi anni qualunque cosa succedesse nella mia vita e, ancor più importante, con i quali ho condiviso alcune delle pagine più belle e spensierate di essa.

Un sentito ringraziamento va anche a Luca e Simone, per l'appoggio morale e materiale in questa attività di tesi.

Contents

List of Tables

List of Figures

Introduction

1.1 Hydrogen context

Sustainable development is not only a need, but also a commitment to the society and environment in which we live. With the target to reduce the emissions of pollutants and mitigate climate change, for an increasingly sustainable future, numerous and solid innovative energy strategies have been spreading in recent years. In particular, renewable and low-carbon gases have been indicated by the International community as carriers that can contribute to the decarbonization of the energy system in a complementary manner to the use of electricity produced from RES (Renewable Energy Sources) in end uses. Renewable gases are all the combustible gases that come from a renewable resource, therefore those gases that can be used as a clean energy source which does not produce any additional emissions during the burning process. Nowadays the main renewable gases are biomethane (which derives from agricultural and agro-industrial biomass, and from the Organic Fraction Municipal Solid Waste) and renewable hydrogen.
In particular, the exploitation of hydrogen in the energy scenario is constantly growing, and it is establishing as a possible game changer for the energy transition, acting as an efficient mean to produce energy as well as to favor the decarbonization of industrial and transport sectors. The reasons that make it so attractive from an energy point of view are due to its suitability for all energetic needs (also as a fuel for transportation), but at the same time to its programmability (it may already in place transportation and storage facilities) as well as efficiency (suitable even for distribution purposes) [1]. European commission intends to support the development of hydrogen from renewable sources increasing the capacity of electrolysers up to 2x40 GW by 2030, with the aim of having up to 13-14% of hydrogen in the final consumption mix by 2050 and up to 75% of renewable gases in the total consumption of European gas by 2050 also [2]. The development of hydrogen from RES can mobilize up to 470 billion euros of investments by 2050, and the development of low-carbon hydrogen, in particular, up to 18 billion euros, having as potential entry markets mainly industrial end uses as well as mobility [3]. Once described the reference energy context, it is necessary to focus on the ways in which hydrogen is produced and used in the energy sector. It is the most widespread chemical element in nature, of which it occupies about 75%. It is absent in pure form in the atmosphere, but it is present as a constituent component of water and in the vast majority of known organic materials, such as in living beings, oil, and minerals. Hydrogen can be produced by several physical and chemical processes, among which the main pathway is from natural gas for industrial uses, through a thermochemical conversion process with resulting CO_2 production (grey hydrogen production). This “grey hydrogen” can be further manipulated thanks to carbon dioxide capture and storage technologies (including pre-combustion, post-combustion, and oxyfuel combustion processes) to obtain a decarbonized hydrogen, the so called “blue hydrogen”. The key conversion reactions for steam reforming to obtain the latter type of mentioned hydrogen from the grey one are reported below:

$$CH_4 + H_2O \rightarrow CO + 3H_2 \qquad (1.1.1)$$

$$CO + H_2O \rightarrow CO_2 + H_2 \tag{1.1.2}$$

Another pathway to produce hydrogen is given by the electrolysis. In this process water is broken down into its constituent elements, i.e. hydrogen and oxygen, through the use of electricity from renewable energy sources according to the reaction:

$$H_2O \rightarrow H_2 + \frac{1}{2}\, O_2 \tag{1.1.3}$$

Electricity is thus transformed into chemical energy and stored in the form of hydrogen. Depending on the hydrogen requirement, it can be used in fuel cells for propulsion of vehicles or even be converted back into electric energy. This process does not lead to the formation of carbon dioxide, therefore the hydrogen produced through it is called “green hydrogen”. It is important to underline that in the current energy context the 75% of produced hydrogen is obtained from natural gas, hence it is the blue or grey-type one, while almost the rest (23%) is produced from coal gasification (brown-type hydrogen), with only 2% of green hydrogen [4]. This scenario will be completely reversed starting from 2028, when green hydrogen will become competitive with hydrogen produced from fossil fuels, to then see its market to take off in the energy mix, settling down as the main hydrogen type among those available [5]. To properly understand the expected evolution of renewable hydrogen a scheme reporting the global low carbon hydrogen production in the period 2020-2050 is attached below.

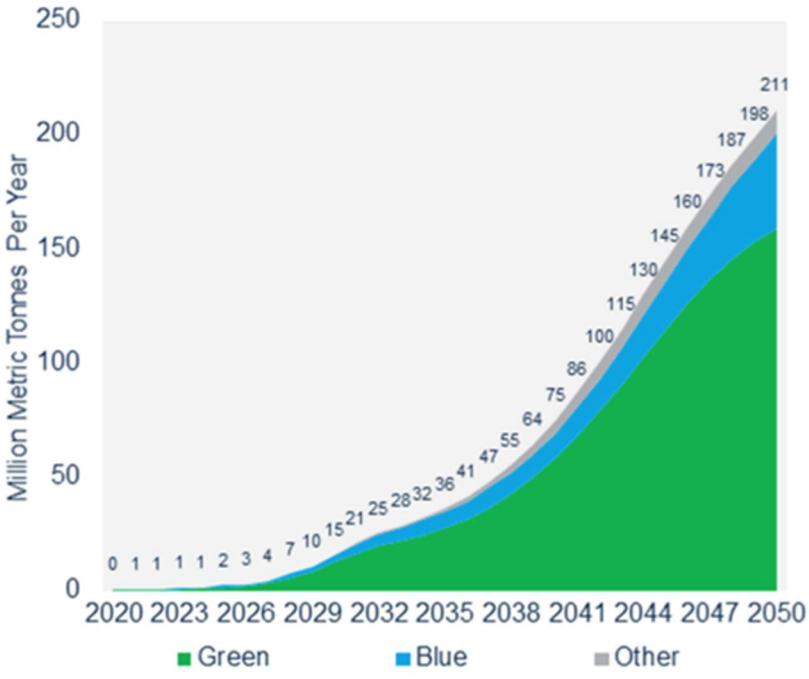

Fig. 1.1.1. Low carbon hydrogen evolution in 2020-2050.

The reason of the increasing share of renewable hydrogen in the future energy context lies in the fact that the use of hydrogen as a fuel is not really sustainable if it is produced from fossil fuels, therefore among the types of production mentioned above, the one through electrolysis (green hydrogen) is undoubtedly the best choice for the environment sustainability. The production of "green" hydrogen is in fact the only one that takes place in an eco-friendly manner and totally free of CO_2 emissions starting from renewable energy (e.g. hydroelectric energy or photovoltaic), guaranteeing no type of pollution in all stages of manufacturing.

1.2 Hydrogen for mobility: HFCVs

As previously mentioned, one of the energy sectors that plays a key role in the decarbonization process, to be developed for a more sustainable future, is that of transport and mobility. Fossil fuels, in fact, conventionally used to power most of the vehicles circulating on the planet, are one of the factors responsible for climate change. During their combustion process harmful substances, greenhouse gases and particulate matter end up in the air and contribute to global warming as well as to a whole series of negative consequences for our health causing syndromes and diseases such as asthma, allergies, cancer. In this regard, electromobility is establishing itself as a valid and more eco-compatible alternative to the use of internal combustion engine powered vehicles, representing one of the most promising projects for the sustainable mobility of the future. Electromobility frees us from fossil fuels; the same, in addition to be limited, are difficult to access, often representing one of the favorites modalities to finance wars and terrorism, also causing serious environmental damage and pollution during their extraction process from the subsoil and their transport for final uses (i.e. “collateral damage” in tanker wrecks) [6]. Environmentally friendly and future-oriented electromobility is made possible by electric vehicles, including both batteries and fuel cells based ones, marked by a variety of positive characteristics in terms of environmental and climate protection. Electric vehicles, thanks to the reduction of air ad acoustic pollution, improve the quality of life and public health, being carbon and other toxic substances emissions-free and not producing any noise during their operation. From a social point of view the progressive abandonment of fossil fuels allows the reduction of struggles for the procurement of resources, as well as of the number of “climate refugees” through the containment of climate change. Moreover, electromobility makes it possible to create and guarantee innovative and high quality jobs, reducing dependence on petroleum-derived fuels and therefore on the politically unstable countries that export them, thus contributing significantly to energy and economic self-sufficiency. Finally, it is worth mentioning that through batteries and hydrogen it is possible to give an important contribution to long-term stability of the energy network, also allowing to use and no longer waste the excess of renewable energy, storing it for example in the form of hydrogen.

As anticipated above, electric vehicles category includes both “traditional battery vehicles” and Hydrogen Fuel Cell Vehicles (HFCVs). In both cases the principle of converting energy into motion is carried out by an electric motor: the differences among them can be seen by comparing the energy source, refueling times and autonomy. While a traditional battery vehicle gets its energy from a battery, as the name suggests, a HFCV gets it from a hydrogen-based fuel cell. What will matter in the future will not be the type of electric vehicle to choose, but to opt to drive an electric vehicle, whether it is battery powered, fuel cell or a combination thereof. In this sense the task of the Public

Administration is to promote all forms of electromobility, creating the related infrastructure for refueling or recharging and raising awareness among the population, thus ensuring a sustainable future for our planet.
The fuel cell technology used to power vehicles, which actually represents the latest generation of electromobility currently available, is the focus of the present work, which aims to deal with hydrogen fuel cell vehicles both by describing their technical and operational characteristics, and in particular by analyzing their safety in specific contexts. HFCVs, besides not being polluting, must have the same characteristics of traditional vehicles in terms of comfort and practical benefits provided. Moreover, they must be able to head out on long distances, have guaranteed performances, and their filling stations must be well distributed throughout the territory, ensuring refueling and maintenance in short times. A HFCV fulfills all of these criteria, in addition to the already described total absence of noise and harmful emissions. Numerous hydrogen fuel cell vehicle models are available on the market, including for example Honda Clarity FC, Mercedes-Benz GLC F-CELL, Hyundai NEXO, and Toyota Mirai. Among them the case of the Toyota Mirai is now examined, not so much because it differs from the others in terms of characteristics and technology, since all hydrogen fuel cell vehicles are marked by the same operating principle, rather because on the basis of its technical specifications it is carried out the case study analyzed starting from chapter three.

Fig. 1.2.1. Toyota Mirai.

In a HFCV the oxygen contained in the air that hits the vehicle during motion enters from the front of the bodywork and reaches the fuel cells. A fuel cell has a structure, as depicted in fig. 1.2.2, which consists of two electrodes, a positive electrode (cathode) and a negative one (anode), separated by an electrolyte. A single fuel cell, being only few millimeters thick and producing a small amount of power, is connected in series with other tenths or hundreds fuel cells, and all of them are stacked together to constitute a fuel cell stack. The anode is fed by the fuel, that is hydrogen, while in the cathode it is introduced the aforementioned oxygen. In addition, a catalyst is placed between these two electrodes, and it causes electrons to travel through an external circuit, being responsible of power generation [7]. In particular, fuel cell stack adopted in the Toyota Mirai model is characterized by a power density per unit volume of $3.1\ \frac{kW}{l}$, with a maximum power of 128 kW.

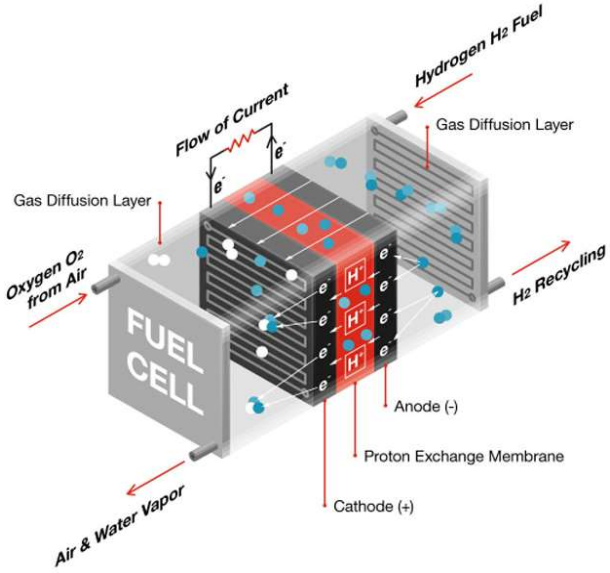

Fig. 1.2.2. Hydrogen fuel cell stack.

In the fuel cell stack oxygen and hydrogen react through a chemical reaction, producing electricity, heat, and water vapor according to:

$$H_{2(g)} + \frac{1}{2}O_{2(g)} \rightarrow H_2O_{(g)} \tag{1.2.1}$$

The water vapor produced is expelled from the exhaust pipe of the vehicle, accompanied at most by few drops of liquid water in case of low ambient temperatures and nothing else, thus being the reason for which hydrogen fuel cell vehicles are so sustainable and eco-friendly. The hydrogen needed to feed the anode of the stack, hence the fuel of this innovative technology, is provided by a high pressure tank installed in the rear of the car, able to contain up to 142.2 l of compressed hydrogen. This tank stores the gaseous hydrogen to a nominal working pressure of 70 MPa, also

being light and compact, and guaranteeing an incredible concentration equal to 5.7 wt%. The electricity produced by the fuel cell stack is exploited by an electric driven motor, having maximum power and maximum torque of, respectively, 134 kW and 300 Nm. This component is the responsible of the vehicle final motion by actually operating it, and is also supported, if necessary, by a battery. The latter stores the energy recovered under braking and supplies more energy to the fuel cells during acceleration, accompanying the operation of the electric motor in case of greater power needs. Other key components of a HFCV are the control unit and the auxiliary transformer. The control unit constantly monitors both the performance of the fuel cell stack, in all driving conditions, and the battery state of charge. The auxiliary transformer, compact and highly efficient, carries the fuel cells voltage to a suitable value for the operation process, i.e. 650 V. A scheme of the main components included in a hydrogen fuel cell vehicle is reported in fig. 1.2.3.

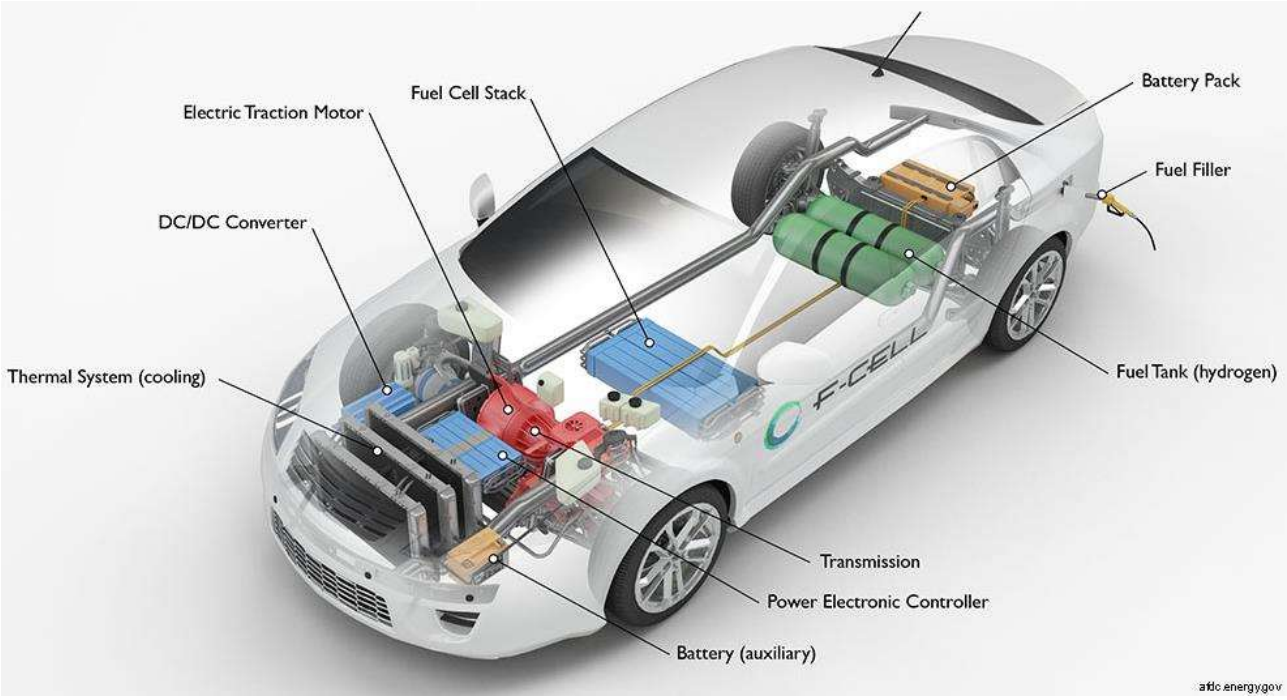

Fig. 1.2.3. HFCV scheme of main components.

Another pros of hydrogen fuel cell vehicles is represented by the speed with which they can be refuelled, as well as by their incredible autonomy. Refueling a HFCV is in fact a very quick operation, lasting about 4 minutes, hence being much faster than the case of a traditional electric vehicle. Moreover, hydrogen refueling is not only fast, but also simple, as it takes place in normal refueling stations very similar to conventional ones for traditional vehicles. In addition, compared to fossil fuels and traditional electric powered cars, HFCVs are characterized by an outstanding autonomy, arriving to cover up to 650 km with a full tank. This translates into the possibility of going further, for a longer time, and without the need to continuously stop to refuel the vehicle, even due to the high efficiency of the electric driven motor embedded in the Mirai, which uses only 0.79 kg of hydrogen to travel 100 km [8].

Up to now the description of HFCVs focused mainly on cars, being the target of the case study developed in the present activity, but it is worth mentioning that hydrogen is also ideal as an alternative fuel for large vehicles, such as hydrogen buses, trolleys forklifts, garbage trucks, and construction vehicles airport transportation. The fuel cells technology is in fact mature enough to be able to power almost all the types of vehicles available on the market, without any distinction. To conclude, given that considerable attention has been paid in terms of high ecology, efficiency, and autonomy of HFCVs, it is legitimate to wonder why we have not been traveling on them for some time already. The are various answers to this question. First of all, it takes time to build the appropriate infrastructure, as well as to make the prices of hydrogen vehicles competitive through the production of an adequate number of pieces. Subsequently, car manufactures want to take the most and for as long as possible advantage from the resulting gains of petrol and diesel vehicles. Therefore, up to now the interest of car manufacturers has also been limited, and the progress of technique has not been accelerated or however proceeds slowly. In the end, it must be considered that even the political global change accompanied by the transition from fossil fuels to alternative ones, and from a monopoly economy of few countries and industrial groups to one energy source that can be produced anywhere, cannot happen overnight and without any resistance. For this reason it is important to remain tenaciously linked to the topic of sustainable mobility, and gradually move towards the direction of electromobility.

Safety assessment of HFCVs

2.1 Safety requirements on HFCVs

In the previous chapter the technology behind hydrogen fuel cell vehicles was treated in detail, together with the main advantages that characterize them, but nothing was said about their relative safety during operation. HFCVs safety is at the heart of the current debate about the shift towards alternative fuels, since hydrogen, to meet the goal of a sufficient energy density to be reached in the vehicle, must be stored at much higher pressures compared to methane and LPG. In fact, for methane and LPG powered vehicles the operating pressure of the fuel is, respectively, around 200 bar and 8 bar. For HFCVs, instead, this value is much greater, being the hydrogen with which the car is fueled stored at 700 bar [9]. For this reason special precautions must be followed for the manufacturing of the tanks they are equipped with, around which the safety of all this kind of technology revolves. For what concerns gaseous hydrogen properties, it is a very light gas, about 14.4 times lighter than air. It means that, in case of an accidental leakage from the storage tank, it would disperse very quickly in the surrounding environment, making it more difficult to ignite with respect to diesel or petrol, which instead would create a highly flammable pool. However, it must be pointed out that hydrogen is characterized by a large flammability range (intended as the percentage of fuel required to initiate a combustion process), assessing from 4% to 75%. Having a wide flammability range means to obtain more easily the conditions for which the gas mixture, in the case of HFCVs hydrogen-air, can burn. Other gases typically have a much smaller flammability range (for example from 4% to 15% in the case of methane), making them less dangerous from this point of view with respect to hydrogen. This statement suggests that particular attention must be paid in the design of hydrogen containing tanks for automotive applications, a schematic of which is available in fig. 2.1.1. The pressure vessels used for the tanks installed in the Toyota Mirai, and in general in the majority of HFCVs, are commonly called COPV (composite overwrapped pressure vessel). They consist of three layers: a polymeric interior, an intermediate layer in carbon fiber capable of withstanding high tractions, and an outer one in steel able to protect the system from mechanical and corrosive damage [10].

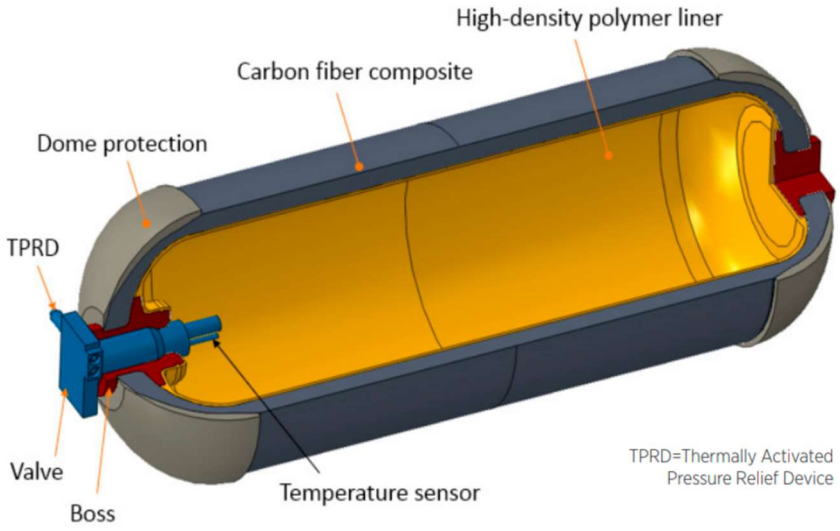

Fig. 2.1.1. Hydrogen storage tank in HFCVs.

The main strength of COPV lies in the carbon fiber, on which a fiberglass layer is also made, which does not contribute to the solidity of the tank, but serves to verify its integrity, for example if the vehicle were to be involved in an accident. In addition, the entire tank is lined with plastic to hermetically seal the hydrogen. To guarantee the safety of HFCVs storage tanks, in compliance with the actual law, several strict standards must be met. In particular, Toyota conducts the following tests on its pressure vessels for hydrogen automotive applications:

- Burst test: the tanks are tested applying a pressure equal to 225% the operating one.
- Seal test: used to ensure that the tank has no gas leakages.
- Fatigue test: during which the tank is filled and emptied thousands of times, thus being subjected to a pulsating fatigue cycle from 0 to 700 bar.
- Fire test: the vessel is exposed to a direct flame, a circumstance which could occur in the case of road accidents. With the temperature increase induced by the flame, the pressure inside the tank would proportionally increase. Hence, to avoid an explosion in these circumstances, the tank gradually releases the gas contained within in through the TPRD (Thermally Activated Pressure Relief Device), in order to lower the pressure.

If that was not enough, in the event of a hydrogen leakage, the Mirai is also equipped with highly sensitive sensors that detect even the smallest amount of hydrogen. They are installed in strategic positions inside the car, to immediately detect the presence of the gas, closing the safety valves and shutting down the vehicle in case of emergency.

2.2 Safety reasons behind the case study

In the previous subchapter it was mentioned that the low density of hydrogen, equal to $0.084\ \frac{kg}{m^3}$ in standard conditions, is a point in favour of the technology behind HFCVs. About that, its high buoyancy means that, in case of an accidental leakage from the storage tank, the gas disperses and spreads rapidly in open environments, therefore reducing efficaciously its concentration to a safe level below the lower flammability level [11]. On the other hand, in confined and semi-confined spaces, such as road tunnels and underground parks, the story is completely different. Indeed, in this kind of scenario, the risks induced by a leakage from the vehicle fuel system are much more problematic than outdoors, thus must be carefully evaluated. In fact, if an accident occurs to a HFCV while it is passing through a confined space a hazard of accumulation and/or ignition of the snared gaseous hydrogen comes to create, with the possibility to lead to harsh consequences such as flash fires or explosions [12]. In addition to that, it is worth remembering that hydrogen fuel cell vehicles are an emerging technology in the current energy context, being a recent solution to contribute to the decarbonization of the transport sector. It implies that, having no precise statistical data about the frequency of HFCVs accidents in road tunnels, it is necessary an effective and appropriate safety analysis as well as a risk assessment, crucial for their public integration [13]. This is even more so because the characteristics and properties of hydrogen vary considerably from those of traditional fuels embedded in agreed upon cars. Moreover, regardless the type of technology used to power the vehicle travelling in the road tunnel, it must be highlighted that the consequences of a fire in a confined space are always more serious than outdoors. This is due to the higher temperatures that can be reached, as well as due to the difficulty in expelling smoke and harmful gases produced by

combustion, together with the reduced visibility especially in case of lighting fails. To aggravate everything, panic and fear that are generated in a closed place must be taken into account too. For all these reasons, the aim of the present work is to understand the impact of a possible fire scenario taking place in a road tunnel caused by an accidental release of hydrogen from the HFCV. Hydrogen leakage from the storage tank of a HFCV can occur due to a release from the TPRD, or due to a small pinhole rupture. The latter case is very unlikely due to the strict standards adopted by manufacturers in the tank construction, while releases of gaseous hydrogen are designed to occur only in the presence of a heat source, such as an external fire due to a serious crash involving a HFCV, which activate the TPRD [14]. In the case of immediate ignition, for example caused by this same heat source, the gas release may burn, resulting in a highly transient jet flame with fire development, the most common fire risk concerning hydrogen fuel cell vehicles. Hydrogen jet fires, in fact, are responsible of high-temperature flames, connected with the possibility to cause burns to the human body, as well as responsible of oxygen deficiency as a result of hydrogen combustion, a dangerous matter for human health. However, this scenario is not the only possible one since the hydrogen leakage ignition might not even happen immediately. In case of delayed ignition, in fact, with an accumulation of the released hydrogen inside the range of flammability limit, an explosion occurs, producing even worse hazards with respect to jet fire, being less controllable. This possibility, although more dangerous, is also much more remote than that of jet fire development. A summary of the possible consequences produced by a hydrogen leakage from a HFCV is reported in fig. 2.2.1.

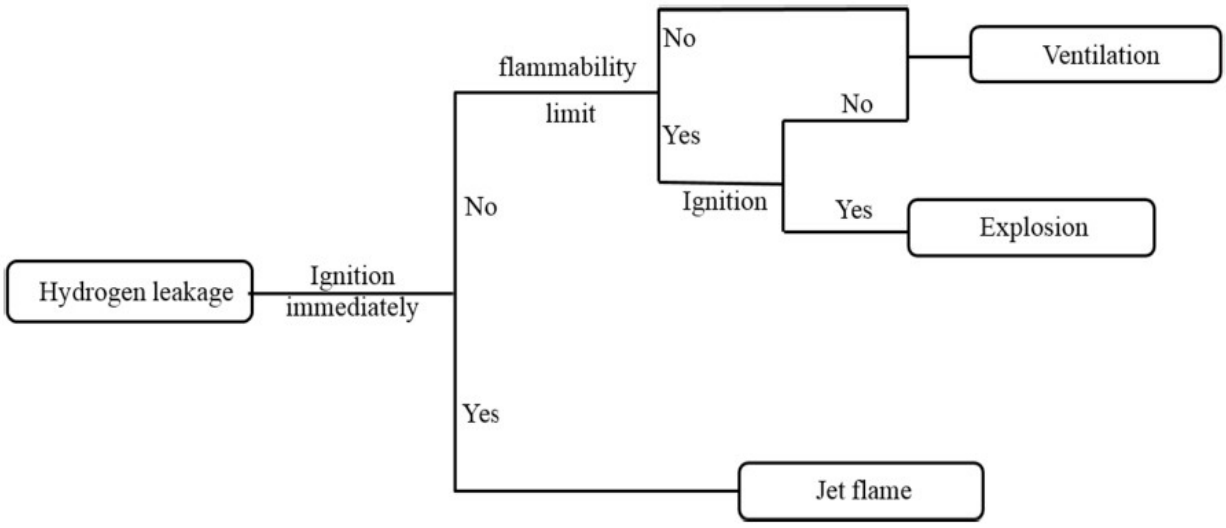

Fig. 2.2.1. Safety issues for hydrogen leakages in a confined space.

As detailed above, in real-case scenario involving hydrogen fuel cell vehicles, the gas is released from the high-pressure storage tank, producing a high-velocity hydrogen jet. This is followed by a fire development in the case of immediate ignition, or an explosion in the case of delayed one. As it is possible to imagine the processes just mentioned are very complex, and focusing on all the aspects that characterize them would be impossible. On this regard, the aim of the present work concerns

the study of a hydrogen fire taking place in a road tunnel, and not hydrogen release from a high-pressure storage tank, thus the case study carried out is built using hydrogen heat release sources. Once the discussion about the possible consequences of a HFCV fire in a road tunnel is over, it is now important to understand the order of magnitude of the frequency with which this kind of accident can occur, essential for an appropriate risk analysis. Having no significant statistical data about hydrogen releases from hydrogen fuel cell vehicles in confined spaces, an approximation is made assuming that the accident rate involving HFCVs might be similar to the one of traditional fossil fuels powered cars, at least as a first approximation. The number of vehicle transits in a tunnel located in a medium-high population area can be estimated in $35 \cdot 10^6$ per year, of which 720 are involved in accidents and only 12 catch fire [14]. It results that the frequency of fires per transit in a road tunnel is roughly $3.3 \cdot 10^{-7}$ that, referred to an average between 1 and 100 transits per year for an average car, becomes from $3 \cdot 10^{-7}$ to $3 \cdot 10^{-5}$ for a single vehicle per year. For what concerns hydrogen fuel cell vehicles, it is worth remembering that the thermally activated pressure relief device is not activated by all kinds of fire in road tunnels, hence the hydrogen ignition and its resulting fatality is not a consequence happening in all fire scenarios for HFCVs. In particular, the individual fatality risk from fires caused by HFCVs in confined spaces is estimated from $2 \cdot 10^{-7}$ to $3 \cdot 10^{-5}$ per year, a frequency range which does not lead to a significant increase in individual risk to people if compared to the one deriving from all types of accidents in everyday life, being the latter around $5 \cdot 10^{-4}$ per year (referred to United States of America population) [15]. The data just discussed suggest therefore that hydrogen fuel cell vehicles are a safe technology for motorists and for the people who interface with them, certainly no more dangerous than traditional fossil fuels powered cars. However, given that the consequences, albeit remote, of a possible accident involving a HFCV in a confined space are quite sever due to hydrogen characteristics and its method of storage in the vehicle pressure vessel, it is necessary to conduct an in-depth study to accurately evaluate the issues related to safety and management of their connected risks. The motivation for which the present work takes place is in fact exactly this one.

Case study statement and methodology

As anticipated in the previous chapter, this work critically analyses the circumstances caused by the fire of a hydrogen fuel cell vehicle taking place in a road tunnel, simulating a real fire event, and estimating its probabilistic evolution on the basis of some predetermined conditions. Subsequently, this scenario is compared to the one caused by a traditional gasoline-powered car, to make reference in the analysis of fire related safety hazards. In the end some mitigation strategies are investigated to try to reduce the critical issues triggered by the fire itself.

3.1 Problem approach with PyroSim and FDS

All the simulation procedure was carried out using PyroSim, a fire dynamic and smoke control simulation software based on the FDS platform. The latter (Fire Dynamic Simulator) is a computational fluid dynamic software developed by NIST (The National Institute of Standards and Technology) and based on the high-definition computer language "Fortran 90". FDS solves numerically a form of the Navier-Stokes equations appropriate for low-speed, thermally driven flow, with emphasis on smoke and heat transport from fires. Established the spatial and temporal grids, needed to solve the fire-driven fluid flow problem, the temperature, density, pressure, velocity, and chemical composition within each numerical grid cell at each discrete time step are computed. The typical output physical quantities of the Fire Dynamic Simulator software are the gas phase temperature, gas phase velocity and species concentration, space pressure, heat release rate per unit volume as well as visibility estimation [16]. The classical equations developed by FDS follow.

Continuity equation (conservation of mass):

$$\frac{\partial \rho}{\partial t} + \nabla \cdot \rho u = \dot{m}_b''' \tag{3.1.1}$$

with ρ density $\left(\frac{kg}{m^3}\right)$, t time (s), u velocity $\left(\frac{m}{s}\right)$, $\dot{m}_b'''$ net heat flux from thermal conduction and radiation $\left(\frac{kg}{m^3 s}\right)$.

Newton's second law (conservation of momentum):

$$\frac{\partial}{\partial t}(\rho u) + \nabla \cdot \rho u\, u + \nabla p = \rho g + f_b + \nabla \cdot \tau_{ij} \tag{3.1.2}$$

with p pressure (Pa), g gravity acceleration vector $\left(\frac{m}{s^2}\right)$, f_b external body force $\left(\frac{N}{m^3}\right)$, τ_{ij} stress tensor $\left(\frac{N}{m^2}\right)$.

First law of thermodynamics (conservation of energy):

$$\frac{\partial}{\partial t}(\rho h) + \nabla \cdot \rho h u = \frac{Dp}{Dt} + \dot{q}''' - \dot{q}_b''' - \nabla \cdot \dot{q}'' + \varepsilon \tag{3.1.3}$$

with h enthalpy $\left(\frac{J}{kg}\right)$, $\dot{q}'''$ heat release rate per unit volume $\left(\frac{W}{m^3}\right)$, $\dot{q}_b'''$ energy transferred to the evaporating droplets $\left(\frac{W}{m^3}\right)$, $\dot{q}''$ heat flux vector $\left(\frac{W}{m^2}\right)$, ε dissipation rate $\left(\frac{W}{m^3}\right)$.
As anticipated before, the FDS resolutive model uses an approximate form of the Navier-Stokes equations, valid for low Mach numbers. This approximation can be applied since the flow velocities reached in a fire are quite low compared to the speed of sound, allowing the use of not too small time steps, which are instead necessary for the resolution of a system of equations in discretized form with streams travelling at speeds comparable to the one of sound [17]. Following the work of Rehm and Baum concerning the flows with low Mach numbers and subjected to heat sources, in the development of the FDS software it is considered an approximation of the equation of state in which the pressure is decomposed into a background term and a perturbation term [18]. It is assumed that the background component of pressure may vary from one compartment to another; in this way for example the pressure in the m-th zone is a linear combination of its background component and the perturbation induced by the flow according to:

$$P(x, y, z, t) = \bar{P}_m(z, t) + \tilde{P}(x, y, z, t) \tag{3.1.4}$$

with $\bar{P}_m(z, t)$ background pressure, function of the vertical spatial coordinate z and time t, and $\tilde{P}(x, y, z, t)$ perturbation component of the pressure. The aim of this decomposition is that, for low Mach number flows, it can be assumed that the temperature and density are inversely proportional, hence the equation of state (in the m-th pressure zone) can be approximated as:

$$\bar{P}_m = \rho T R \sum_{\alpha} \frac{Z_\alpha}{W_\alpha} = \frac{\rho T R}{\bar{W}} \tag{3.1.5}$$

with Z_α mass fraction of lumped species α. The pressure in the state and energy equations is replaced by the background pressure $\bar{P}_m$ to filter out sound waves that travel at speeds that are much faster than typical flow speeds expected in fire applications. The assumption of low Mach numbers has two main aims. The first is connected to the fact that the filtering of acoustic waves entails that the time step in the algorithm is bound only by the flow speed as opposed to the speed of sound, while regarding the second purpose the modified state equation enables a reduction of one dependent variable in the reference system of equations. The equation (3.1.3) is not explicitly solved, but rather its source terms are included in the expression of the flow divergence: when the

velocity field satisfies the specified thermodynamic divergence, the conservative form of the sensible enthalpy equation is satisfied by construction [19]. In the applications that concern us there is only one background pressure, denoted as $\bar{P}_0(z,t)$, and assumed as the atmospheric pressure stratification that is used as both the initial and boundary condition for the governing equations. It is calculated thanks to the following equation:

$$\frac{d\bar{P}_0(z,t)}{dz} = -\rho_0(z)\, g \tag{3.1.6}$$

with $\rho_0(z)$ background density and $g = 9.81\ \frac{m}{s^2}$. It must be specified that the subscript zero points out the exterior of the computational domain, and not time zero. Taking advantage of the equation (3.1.5), the equation of state, the background pressure can be expressed as a function of the background temperature, $T_0(z)$:

$$\bar{P}_0(z) = P_\infty\, e^{-\int_{z_\infty}^{z} \frac{\bar{W} g}{R T_0(z')} dz'} \tag{3.1.7}$$

in which the subscript infinity generally refers to the ground. In the expression (3.1.7) it is possible to define a linear stratification of the background temperature such that:

$$T_0(z) = T_\infty + \Gamma z \tag{3.1.8}$$

with T_∞ temperature at the ground and Γ lapse rate (e.g., $\Gamma = -0.0098\ \frac{K}{m}$ is the adiabatic lapse rate). Once the term $T_0(z)$ is known, the background pressure is estimated with the integral expression (3.1.7), and it is the constant quantity to which the perturbation term is then added.

3.2 Road tunnel modelling

The road tunnel chosen for the purpose of the present work is “Virgolo”, located on the route of the A22 motorway (Autostrada del Brennero) near the km 77 in the autonomous province of Bolzano in Italy. It consists of 2 tubes, each of which is 887 m long and with 2 lanes both running in the same direction of traffic: Brennero direction for the north tube and Modena direction for the south one. The latter is the one considered as the setting for the fire scenario being analysed. Virgolo road tunnel has 2 by-pass rooms having an area of about 40 m^2 each, spaced 250-310 m and accessible from both tubes [20].

Fig. 3.2.1. Virgolo road tunnel.

Fig. 3.2.2. Virgolo road tunnel south tube zoomed view.

A top view map of Virgolo is attached below to display the configuration of the road tunnel under investigation.

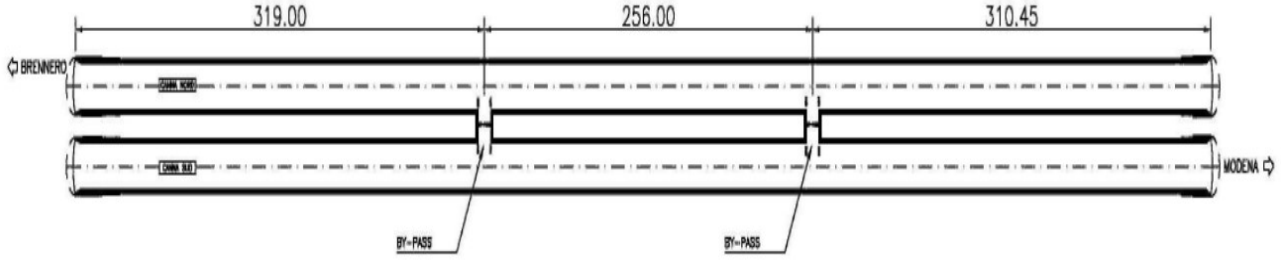

Fig. 3.2.3. Top view map of Virgolo road tunnel.

The straight type section of the south tube of Virgolo, in 1:50 scale, is shown in fig. 3.2.4. On its basis a 2D CAD was created using the software AutoCAD®. The two dimensional perspective drawing reproduced was subsequently given in input to the software Rhinoceros to build the 3D CAD of the prototype road tunnel, faithful representative of the actual Virgolo road tunnel. In particular, the model was built with a length of 250 m, in such a way to simulate the stretch of the tunnel between the two by-pass rooms, represented in fig. 3.2.3, given the impossibility to simulate the road tunnel in its entirely size for computational reasons. The meaning of this choice lies in the fact that, obviously, the most critical point in which an accident can occur in a road tunnel is in its central part, as it is the furthest from the entrance and exit, thus making it difficult to rescue the occupants. The set target was therefore to consider the worst scenario in which the fire could occur.

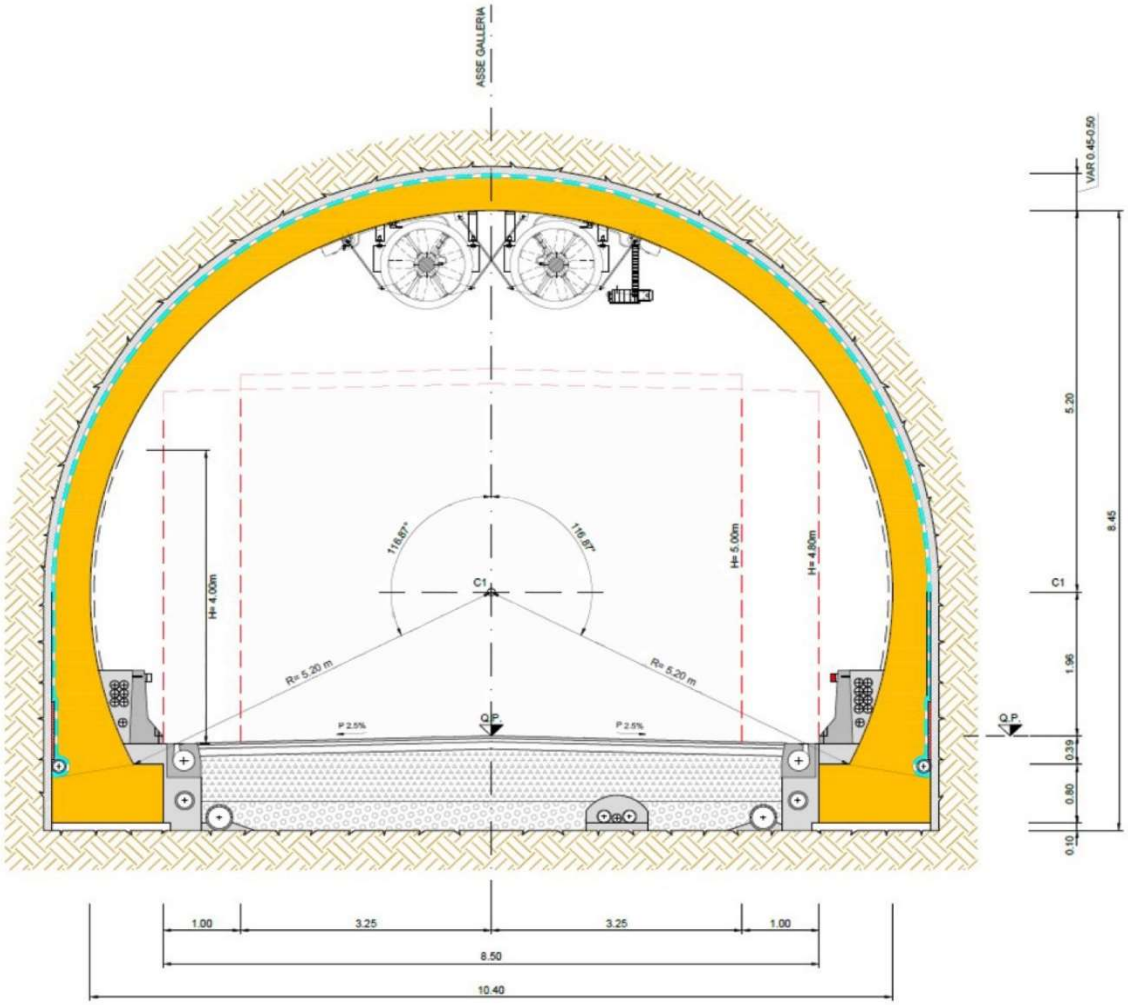

Fig. 3.2.4. Straight section of Virgolo road tunnel.

As it is shown by fig. 3.2.4 both lanes of Virgolo have a slope with respect to the horizontal of 2.5%, while the altitude difference between entrance and exit of the tunnel is 0.2% [21]. Although the values of these slopes are not particularly high, they have nevertheless been taken into account in the creation of the road tunnel CAD model. The latter, used to conduct all the simulations object of the present work, is depicted in the following figures: top 2D (fig. 3.2.5), front 2D (fig. 3.2.6), side 3D view (fig. 3.2.7). The pale blue cube included within them represents the burning car object of the analysis, that will be characterized in detail in the next subchapter. Inside the road tunnel the car was assumed to be located in the centre of the right-hand lane, the traffic one, exactly in the middle of the considered control volume, therefore at 125 m from the entrance. This is to have a realistic representation of the car driving in the tunnel as well as symmetrical geometries upstream and downstream of the fire source.

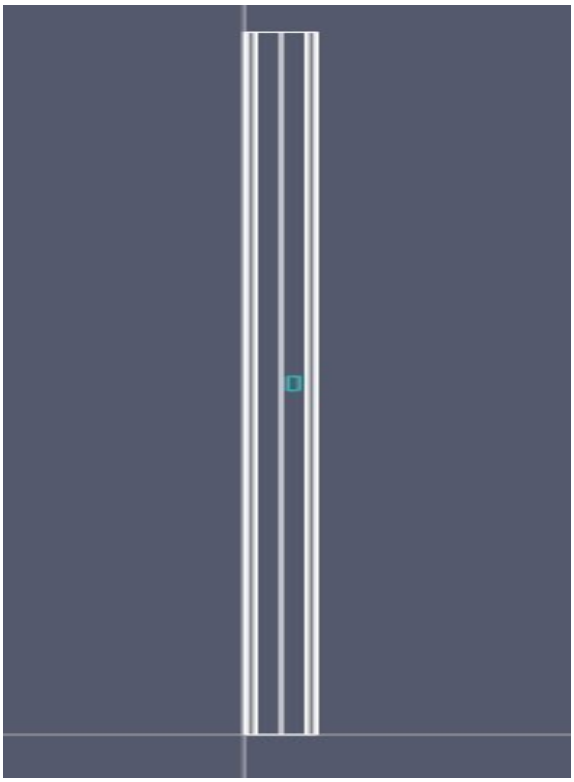

Fig. 3.2.5. Top 2D CAD model view.

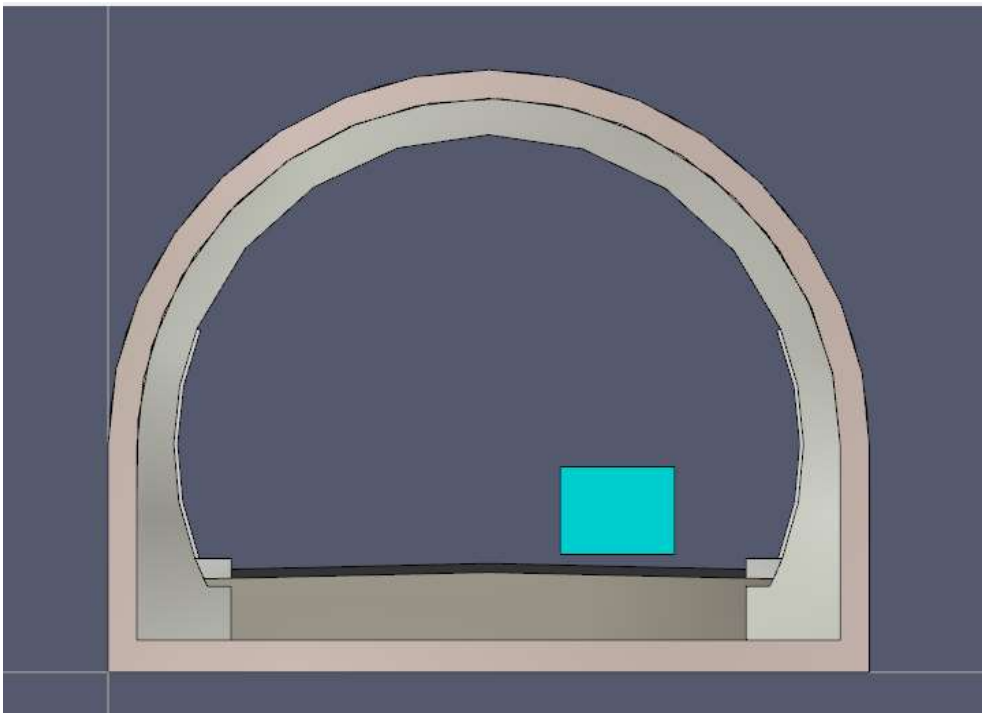

Fig. 3.2.6. Front 2D CAD model view.

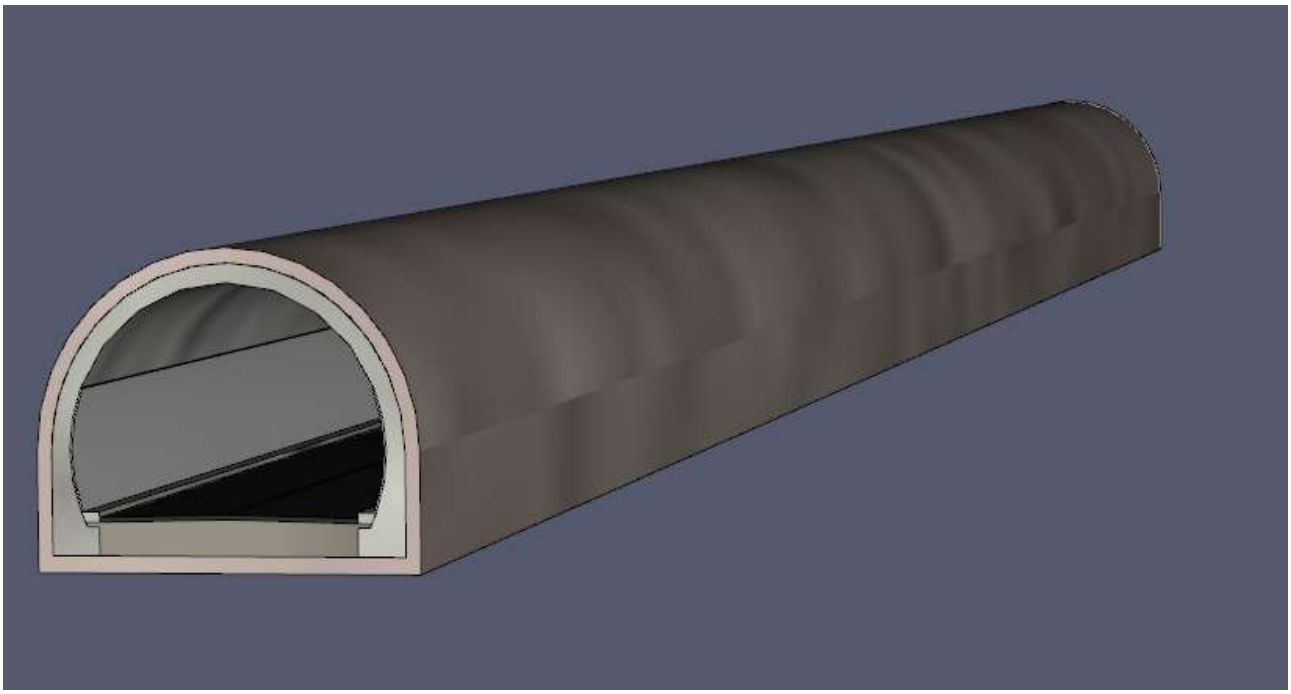

Fig. 3.2.7. Side 3D CAD model view.

Looking at the previously reported representations of the developed CAD, the aim now is to explain the criteria used for the assembly of the road tunnel model. A geomorphological analysis was conducted on the site where the tunnel is located, to properly characterize the natural environment surrounding the Virgolo. The area between Bolzano and Trento ("Atesino volcanic complex") marks mainly by volcanic rocks, especially rhyolites and rhyodacites, which are rocks of felsic composition, with aphanitic shape [22], [23]. To consider this occurrence in the modelling, an outer layer of volcanic rock with thickness 0.5 m was included all around the tunnel profile. As regards the construction materials of the road tunnel prototype, it was used a conformal concrete coating with circular arc, not reinforced. Of the same material was made the verge at both sides of the lanes. The internal lining of the tunnel, up to a height of 4m from the road surface, was made of porcelain steel in prefabricated panels, which allow a greater internal brightness (high reflectance), incombustibility, thermal and chemical resistance, and particular ease of cleaning [24]. The road surface was modelled considering a first thick underlying layer of deposition gravel, essential for the pavement construction phase, topped with a second thin layer of real asphalt. The latter was modeled as a conglomerate of calcium carbonate (85% mass fraction) and natural bitumen (15% mass fraction) [25]. Taking advantage of fig. 3.2.8, nothing but the front 3D CAD model representation, it is possible to view and fully understand the structural components of the road tunnel prototype described above.

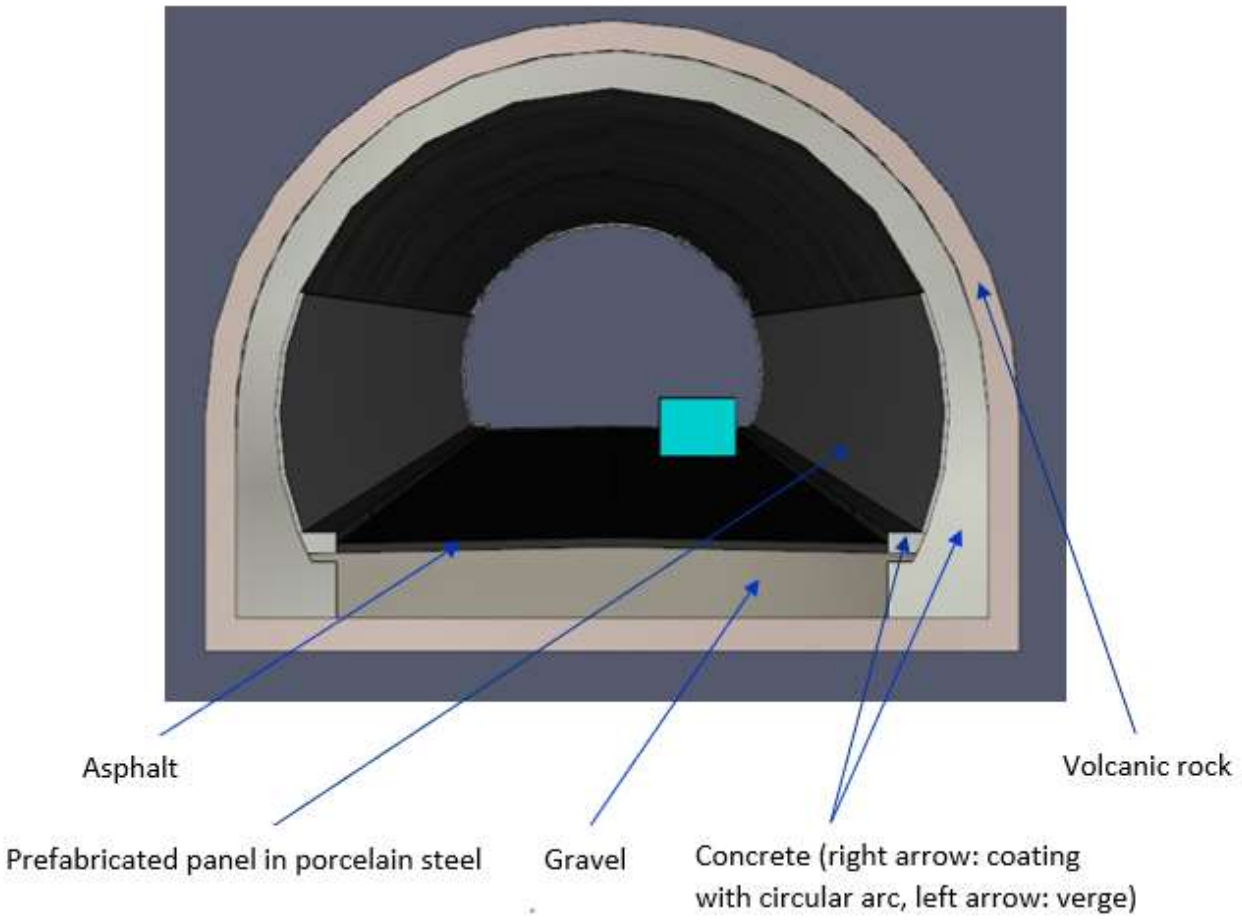

Fig. 3.2.8. Front 3D CAD model view with highlighting of the tunnel structural components.

A summary of the thermophysical properties of the materials constituting the road tunnel model is available in tab. 3.2.1.

	Density $\rho\left(\frac{kg}{m^3}\right)$	**Thermal conductivity** $k\left(\frac{W}{m\,K}\right)$	**Specific heat** $c_p\left(\frac{kJ}{kg\,K}\right)$	**Emissivity** $\varepsilon\ (-)$
Volcanic rock	2600	3.3	0.808	0.93
Gravel	1850	0.665	0.85	0.95
Asphalt	2100	0.756	0.921	0.90
Concrete	2280	1.8	1.04	0.88
Porcelain steel panels	2800	0.84	0.84	0.92

Tab 3.2.1. Thermophysical properties of the materials constituting the road tunnel.

Regarding other input data of the simulation set up, the entrance and exit vents of the road tunnel model were treated as open surfaces, applying a constant pressure gradient, while the pressure perturbation at the boundary was set to zero. The atmospheric conditions of the environment inside

it were set as follows: ambient pressure $1.01325 \cdot 10^5\ Pa$, ambient temperature $20\ °C$, relative humidity $40\ \%$, ambient oxygen mass fraction $0.232\ kg/kg$, ambient carbon dioxide mass fraction $5.95 \cdot 10^{-4}\ kg/kg$, specific gravity $9.81\ \frac{m}{s^2}$.

3.3 Car modelling

Once the discussion of the road tunnel model structure is over, it is time now to deal with the modelling in the simulation setup of the hydrogen car to be investigated. The car model chosen as the paradigm to analyse fire and safety scenarios in the present work is “Mirai”, produced by the Japanese company Toyota starting from 2015. An extract from its technical datasheet is shown in tab. 3.3.1 [26].

DIMENSIONS	
Length (mm)	4975
Width (mm)	1885
Height (mm)	1470
Minimum ground clearance (mm)	150
Number of seats	5
Fuel tanks capacity (kg)	5.6
Fuel tanks volume (l)	142.2
WEIGHTS	
Unladen mass (kg)	1900
CELLS PACK	
Model code	FCB 130
Fuelling	Fuel cell
Number of cells	330
Maximum power (kW/cv)	128/174
Power density	5.4
MOTOR GENERATOR	
Model code	3KM
Typology	Permanent magnet synchronous
Maximum power (kW/cv)	134/182
Maximum torque (Nm)	300
BATTERIES	
Typology	Lithium ions
Number of cells	84
Nominal voltage (V)	310.8
Capacity (Ah)	4

Tab. 3.3.1. Technical datasheet extract of Toyota Mirai.

Taking into account the actual dimensions of the car listed above, the latter was modelled as a parallelepiped-shaped geometric obstruction 4.975x1.885x1.470 m, having ground clearance of 150 mm (with respect to the asphalt level), thickness of 1.1 cm and made up of a single material representative as accurately as possible of all the materials a real car is made of. The thickness value just mentioned has been obtained taking advantage of the equation (3.3.1), in which t_{car} is the car thickness, M_{car} the car unladen mass, S_{car} the car total surface and ρ_{car} the car density.

$$t_{car} = \frac{M_{car}}{\rho_{car} \cdot S_{car}} \tag{3.3.1}$$

As anticipated before, in reality a car is not made up of a single material, but of a set of materials in variable types and percentages depending on the specific model in question. This matter made it necessary to carry out an in-depth study of the structural composition of a motor vehicle, not only to evaluate the car constituting material density value required in the equation (3.3.1), but also to fully characterize all the other thermophysical properties of the geometrical obstruction single component material adopted to shape the Toyota Mirai in the road tunnel. After an analysis conducted on a sample of 7 vehicles, it turned out that, on average, a car is made up of 76 different chemical elements, distributed in 2539 compounds. Given the high amount of numbers involved, these compounds are grouped into main macro-categories of belonging. As it is reasonable to expect, ferrous metals like steel (for plate, rims, frame structural components and suspensions) and cast iron (for the manufacturing of engine, brakes and transmission components), and non ferrous metals like aliminum (for some parts of chassis and body) are the most present by mass of the car: more than 73%. In the second instance there are also considerable quantities of polymers and elastomers, about the 21%, mainly used for finishing of external parts and for the interiors, as well as for the shell, on-board electronics, tank and tyres. In the end, reduced percentages of glass and textiles are included too [27]. A detailed report of the materials involved in the investigated car structure, intented as percentage of the car unladen mass, is attached below.

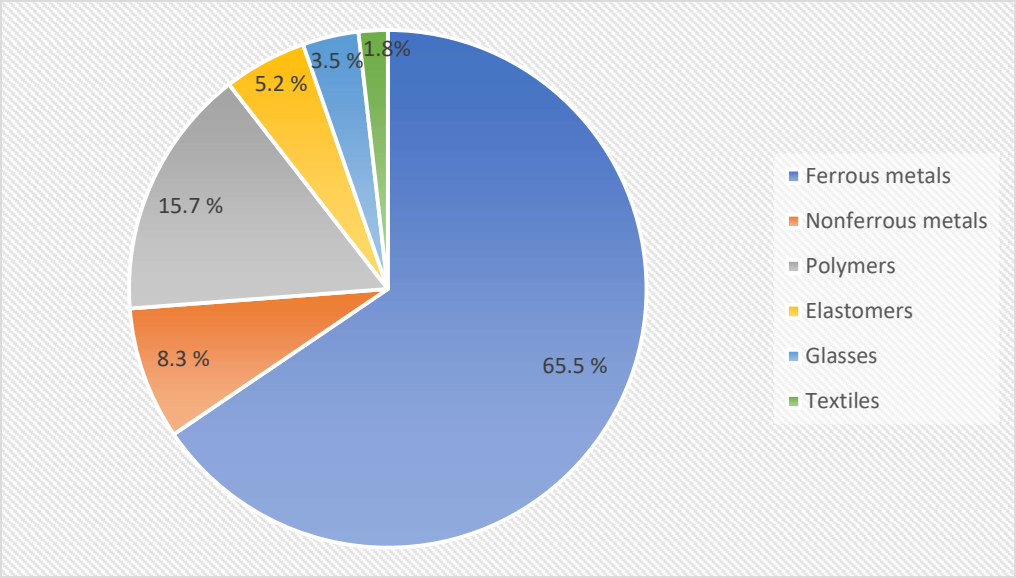

Fig. 3.3.1. Component materials of the reference car model.

The thermophysical properties of the macro-categories to which the materials constituting the car belong, reported as the most representative values for the category itself, are listed in tab. 3.3.2.

	Density $\rho\ \left(\frac{kg}{m^3}\right)$	**Thermal conductivity** $k\ \left(\frac{W}{m\ K}\right)$	**Specific heat** $c_p\ \left(\frac{kJ}{kg\ K}\right)$	**Emissivity** $\varepsilon\ (-)$
Ferrous metals (steel, cast iron)	7850	45.8	0.46	0.95
Nonferrous metals (aluminum)	2700	204	0.896	0.3
Polymers	1380	0.163	1.44	0.95
Elastomers	900	0.13	1.88	0.95
Glasses	2500	1	0.84	0.85
Textiles	100	0.1	1	0.87

Tab. 3.3.2. Thermophysical properties of the materials constituing the car.

Taking advantage of the thermophysical properties of the materials constituting the actual car (tab. 3.3.2), as well as of their percentage mass fraction (fig. 3.3.1), the density ρ_{car} , specific heat $c_{p,car}$, thermal conductivity k_{car} and emissivity ε_{car} of the single component material used to model the car are get. This by simply performing the weighted average on mass basis of the real making up materials, as expressed by equation (3.3.2).

$$\Psi_{car} = \sum_{i=1}^{N} \Psi_i \cdot n_i \tag{3.3.2}$$

The value of the thermophysical property of interest of the generic material is denoted with Ψ_i, while n_i is its corresponding mass fraction with respect to the unladen mass of the car and N is equal to six. The results obtained are the followings:

$$\rho_{car} = 5718.6\ \frac{kg}{m^3}$$

$$c_{p,car} = 0.747\ \frac{kJ}{kg\ K}$$

$$k_{car} = 47\ \frac{W}{m\ K}$$

$$\varepsilon_{car} = 0.891$$

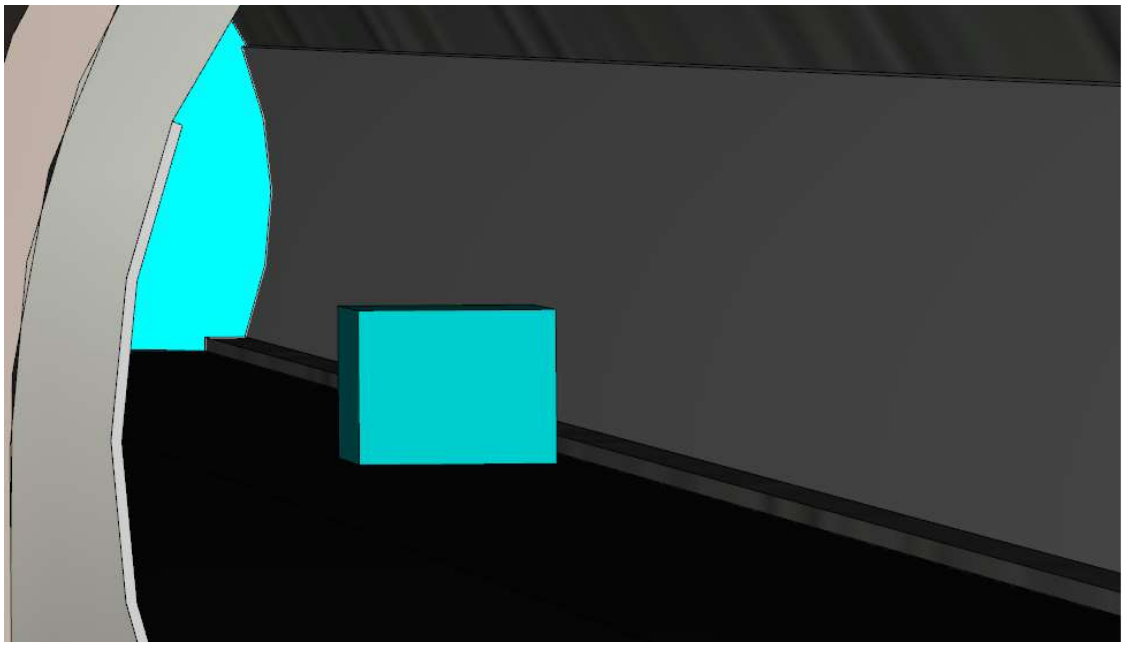

Fig. 3.3.2. Car visualization inside the road tunnel.

The car model assembly described in the previous pages is referred to the hydrogen powered car based simulation, being the latter the focus of the present study. However, since the sizes of the Toyota Mirai are perfectly comparable to those of any traditional fossil fuels-powered car, and that the considerations made for the construction materials apply to any motorcar of medium manufacture, the same setup was used to model the gasoline powered car. Obviously, changes were made in terms of fire modelling and combustion reactions characterization, the real crucial points in the difference between a traditional car fire and a hydrogen powered one.

3.4 Fire modelling

The most important parameter to analyse the potential hazards posed from a fire event is the heat release rate (HRR) of the fire itself, on which the environmental consequences of the event in a confined space depend in large measure. Therefore, the quantitative description of the fire consequences cannot be able to leave the heat release rate of combustible items out of consideration, defined from a theoretical point of view as the product of the fuel weight loss and the heating value of a unit mass of fuel. Typically, the heat release rate of combustible items is determined in laboratory experiments basing on various types of techniques, such as open-burning HRR calorimeters, room fire tests (for the measurement of full-scale HRR), and Cone calorimeters (for small-scale HRR). However, it must be specified that real fire experiments on a combustible item, or on groups of them, are often infeasible due to costs and time required for the tests. Thus, some approximations in the characterization of the HRR are necessary, and for this purpose HRR conventional curves are of incredible support.

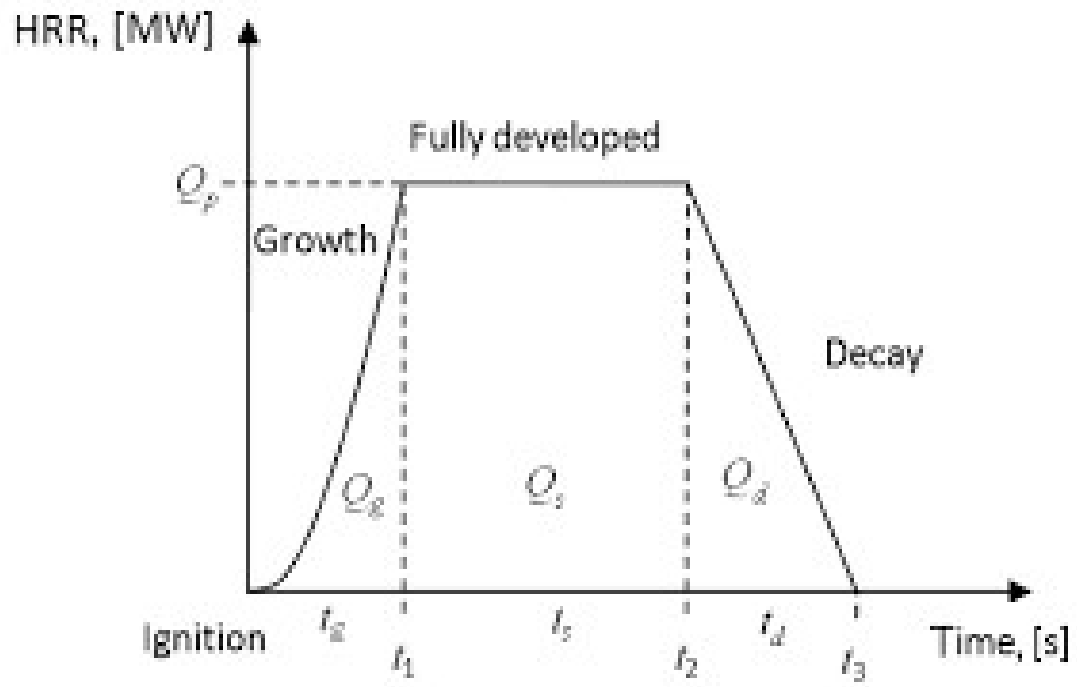

Fig. 3.4.1. HRR conventional curve.

The conventional HRR curve, as reported in fig. 3.4.1, is characterized by four phases: pre-growth, initial growth, steady or maximum burning, and decay. Among them, the initial growth, maximum steady, and decay phases are the key parts, since the pre-growth one is affected by a lot of uncertain factors and is hence typically neglected [28].

The most common way to describe the HRR during the growth stage is with the time squared or t^2 parabolic equation, given by:

$$HRR(t) = \alpha t^2 \tag{3.4.1}$$

with α fire growth coefficient $\left(\frac{kW}{s^2}\right)$, and t time (s). The fire growth coefficient values are connected to the specific growth rates as well as times to reach a conventional reference heat release rate of 1055 kW. The t-squared fire ramp in the HRR conventional curve is configured to grow until the maximum heat release rate is reached at t_1, and this interval of time can be assessed introducing the value of HRR_{max} in the equation (3.4.1) and solving for time t. The value of HRR_{max} depends on the characteristics of the burning object, like materials composition, thickness, burnable surface, as well as on the ventilation, which is the responsible of the transition from a fuel-controlled fire to a ventilation-controlled one. At this point, if automatic extinguishing systems are not envisaged in the activity, it is assumed that from the time t_1 to t_2 the thermal power produced by the fire stabilizes at the maximum value HRR_{max}, according to:

$$HRR(t) = HRR_{max} \tag{3.4.2}$$

The steady fire phase ends at time t_2, the starting time of the decay phase, in which it is assumed that the 70% of the initially available thermal energy has been released. The time t_3, after which the thermal power released by the fire disappears, is calculated considering that the remaining 30% of the initially available thermal energy is consumed in the decay phase. During the latter the trend of the power produced by the fire is linear, therefore it can be expressed as:

$$HRR(t) = HRR_{max} \frac{t_3 - t}{t_3 - t_2} \tag{3.4.3}$$

In the Fire Dynamic Simulator, hence in PyroSim, it is extremely simple to designate a design fire by assigning a predefined $HRR(t)$ value. The most efficient way to do that is the definition of a time-varying heat release rate by specifying the $HRRPUA$ parameter and the time value, in seconds, of the growth phase, so that FDS sets a quadratic growth curve of the type αt^2. The $HRRPUA$ (Heat Release Rate Per Unit Area) must be associated to a flat surface, or like in the present case, a solid object. The latter, i.e. the car modelled with a solid obstruction, burns with a predefined gas phase chemical reaction, which will be discussed in the next subchapter, emitting a thermal power equal to the product of the $HRRPUA$ parameter and the surface area to which it is applied, to be denoted in the simulation setup as a burner type surface.

The $HRRPUA$, thus the maximum thermal power released per unit of gross area, can be defined taking advantage of the following relation:

$$HRRPUA = \frac{HRR_{max}}{A_f} \tag{3.4.4}$$

with A_f gross area of the compartment in case of uniform distribution of the fire load, or area actually occupied by the fuel (m^2). In the present work the reference area aforementioned is assumed to be the top surface of the Mirai, which is $9.378\ m^2$. For what concerns the HRR_{max} the argument is not that easy. In fact, as anticipated above, the maximum heat release rate of a burning car be accurately determined only by real fire experiments, testing an actual prototype of the car in the conditions where the fire scenario is assumed to develop. For the purposes of this activity, it was conducted an in-depth analysis on various related literature studies which, on the basis of fire data for real fire tests, report common values of maximum heat release rates for typical vehicles in commerce. It is found that the heat release rates of frequently used hydrogen-powered car and traditional fossil fuels powered car fires are, respectively, $24.5\ MW$ and $7\ MW$ [29], [30], [31]. It is worth noting that these values are representative as the average of a range of values, as the real HRR of a burning car depends on a large number of factors, such as mass flow rate, storage capacity and environmental conditions. Thanks to the HRR_{max} values just analysed, it is finally possible to specify the $HRRPUA$ values adopted in the simulations carried out, according to the (3.4.4).

$$HRRPUA_{H_2\ car\ sim.} = 2612.5\ \frac{kW}{m^2}$$

$$HRRPUA_{Gasoline\ car\ sim.} = 746.4\ \frac{kW}{m^2}$$

The last element to discuss at this point is the ramp-up time, also to be specified in input in FDS. Its characterization, as already mentioned, can be achieved by inverting the equation (3.4.1). However, this procedure requires to know the fire growth coefficient, which depends on geometrical factors of the combustible materials, the type of combustible materials, as well as on the effect of ventilation. For this reason, rather than using the α coefficient to model the time squared fire growth, of which it is difficult to find in literature a unique and accurate value for the specific case of hydrogen car fire in a road tunnel, in the simulation setup building it is considered directly the value of the time squared itself.

Taking advantage of the work made by Shibani, Fatemeh Salehi, Til Baalisampang, Rouzbeh Abbassi regarding the numerical modeling towards the safety assessment of multiple hydrogen fires in confined areas [30] the value of the ramp-up time for the hydrogen powered car based simulation is set as follows:

$$t^2{}_{H_2\ car\ sim.} = 5\ s$$

On the other hand, in case of traditional fossil fuels powered car the ramp up time is estimated taking as reference the study performed by M. K. Cheong, M. J. Spearpoint, and C. M. Fleischmann, named Design Fires for Vehicles in Road Tunnels [32]. It considers factors such as fuel load, ventilation condition, tunnel geometry and ignition location in real case fire experiments to estimate the heat release rate of a credible vehicle fire in a road tunnel using a performance-based approach. Basing on average conditions, the time of the growth stage for the gasoline powered car based simulation is assumed to be:

$$t^2{}_{Gasoline\ car\ sim.} = 164\ s$$

Once the ramp-up time and the maximum heat release rate for the two cases of interest have been characterized, it is worth viewing the t-squared heart release rate curve, used by the Fire Dynamic Simulator to estimate the transient fire growth.

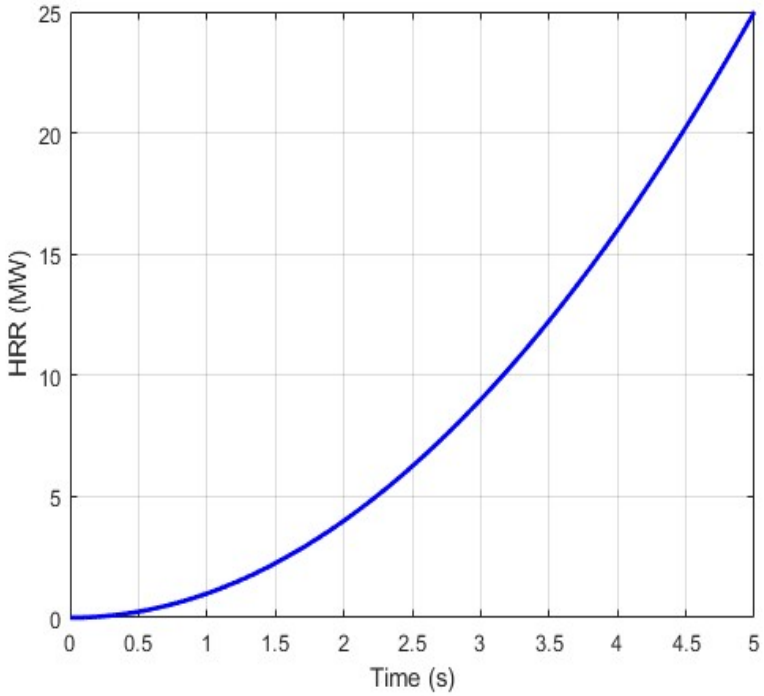

Fig. 3.4.2. t-squared heat release rate curve for hydrogen powered car based simulation.

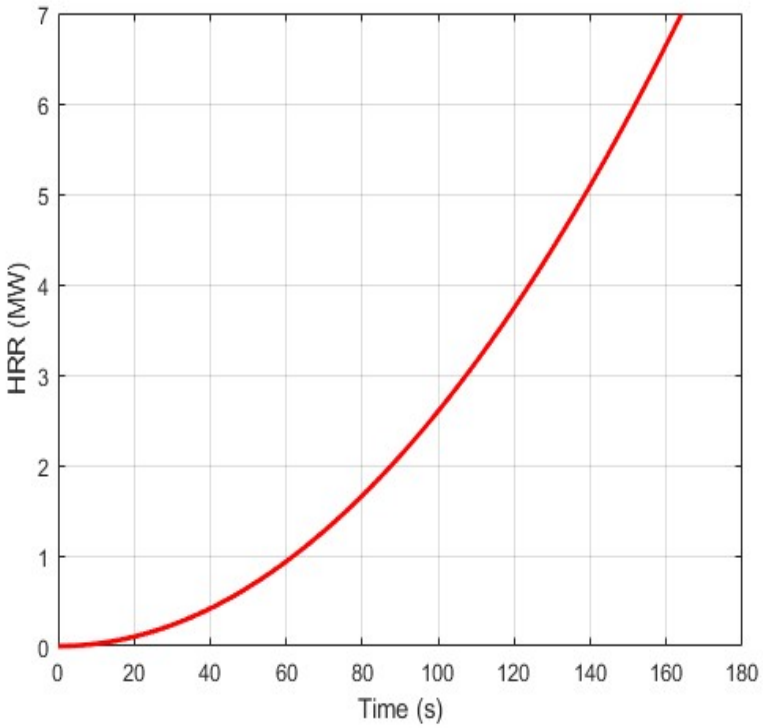

Fig. 3.4.3. t-squared heat release rate curve for gasoline powered car based simulation.

As denoted by fig. 3.4.2 and fig. 3.4.3 the heat release rate of the burning car is set to grow up to the value of $24.5\ MW$ and $7\ MW$, respectively for the hydrogen and gasoline powered car, which occurs at a time (the ramp-up one) equal to $5\ s$ and $164\ s$, depending on the case. It is important to underline that the fire modelling used to build the simulation setup takes into account the growth and the maximum steady stages, while the decay one is not considered. This because it is assumed that in the reference time domain, not wide enough, the quantity of fuel, the materials involved, and the environmental conditions are such as not to allow the extinction of the thermal power produced by the burning car.

3.5 Combustion reactions modelling

The fire modelling previously discussed is strictly related to another important topic for the fire characterization inside the tunnel: the combustion reactions involved in the burning development. Combustion, meant as the reaction of fuel vapour and oxygen, is modelled by the Fire Dynamic Simulator making use of the mixture fraction combustion model, which accounts for the evolution of the fuel gas from its surface of origin through the combustion process. Moreover, in a FDS fire simulation there is only one gaseous fuel that acts as a surrogate for all the potential fuel sources [33]. In the mixture fraction combustion model the reaction is assumed to be of the form:

$$C_x H_y O_z N_v + \nu_{O_2} O_2 \rightarrow \nu_{CO_2} CO_2 + \nu_{H_2O} H_2O + \nu_{CO} CO + \nu_S Soot + \nu_{N_2} N_2 \qquad (3.5.1)$$

with $C_x H_y O_z N_v$ chemical formula of the fuel, assumed to contain only carbon, x, hydrogen, y, oxygen, z, and nitrogen atoms, v, and ν_{O_2}, ν_{CO_2}, ν_{H_2O}, ν_{CO}, ν_S, and ν_{N_2} stoichiometric coefficients of, respectively, oxygen (reactant), carbon dioxide (product), water vapor (product), carbon monoxide (product), soot (product), and nitrogen (product) included in the combustion process. The combustion reaction, used to calculate the combustion products, is characterized in PyroSim by the implementation of a simple chemistry approach, assuming that the fuel and oxygen react fast and is only controlled by mixing. The chemical formula of the fuel must be specified by the user, together with the heat of combustion that characterizes its specific combustion reaction. The yields of CO, soot, H_2, and amount of hydrogen in the soot are also required in input by the mixture fraction combustion model as energy released by-products, but they are automatically provided by the simple chemistry approach tool on the basis of the fuel specified. The ambient oxygen mass fraction, the comburent of the combustion reaction, is assumed to be 0.21 in the simulations carried out. In the hydrogen powered car based simulation the chemical formula of the fuel is trivially $H_2(gaseous)$, with a specified heat of combustion of $1.418 \cdot 10^5 \frac{kJ}{kg}$. On the other hand, for the traditional fossil fuels powered car based simulation the argument is not that easy. In fact, gasoline does not have a unique brute formula, being from a chemical point of view a mixture of about 150 hydrocarbons between C_6H_{14} (hexane) and $C_{12}H_{26}$ (dodecane) in varying proportion, to which alcohols and additives are also added with an essentially detergent function [34]. Its composition varies widely, depending on the crude oils used, the refinery processes available, the overall balance of product demand, and the product specifications. The typical composition of gasoline hydrocarbons (% volume) is as follows: 4-8% alkanes, 2-5% alkenes, 25-40% isoalkanes, 3-7% cycloalkanes, 1-4% cycloalkenes, and 20-50% total aromatics (0.5-2.5% benzene) [35]. Given the impossibility of modelling gasoline with a precise formula with a univocal amount of carbon, hydrogen, oxygen, and nitrogen atoms, as stated above, it is included in the mixture fraction combustion model as a fuel with chemical formula C_8H_{18}. The latter, the alkane commonly known as octane, is in fact one of the components present in greater quantities in gasoline, as well as the one with the chemical-physical characteristics most similar to those of the overall mixture. For what concerns this work, in which the traditional fossil fuels powered car based simulation is used only as a term of comparison in the fire scenario with respect to the hydrogen one, this assumption is

more than legitimate. On the other hand, the heat of combustion of the reaction included in the simple chemistry approach tool is the one of gasoline, thus $4.37 \cdot 10^4 \frac{kJ}{kg}$, and not that of octane.

3.6 Setting the bounds of space and time

This subchapter aims to describe the global input parameters that affect the general scope of the simulation, such as the simulation time and the size of the computational domain, which establish the spatial and temporal coordinate systems that are used by all the other components of the simulation setup. The bounds setting of space is here covered first.
The 3D CAD model used to simulate the road tunnel geometry is contained in a volume whose dimensions are 12.596 m x 250 m x 10.087 m (respectively on x, y, z axis). This is because the Fire Dynamic Simulator is able to numerically solve the set of differential equations described in subchapter 3.1 provided that a spatial grid is built to discretize the computational domain. The latter, in the present work the 250 m long stretch of Virgolo, is divided into number of small cubic cells whose size needs to be appropriately chosen. It is important to underline that in FDS the details at places smaller than the grid size are not studied, as well as geometry of sizes less than the spatial grid are not accepted even if modelled [36]. The base size of the mesh is a direct indication of the computational time required by the simulation to solve the numerical problem under investigation, as well as an index of the calculation resolution with which results are produced. A coarse mesh is desirable from a required simulation time point of view, but unfortunately it cannot guarantee accuracy and reliability of the achieved results. On the other hand, a very fine mesh may result in unpractical or not affordable simulation times but gives accurate results from a physical point of view. Therefore, the grid size is a matter of trade-off between accuracy and computational cost and hence must be chosen reasonably. In this sense a support can be provided by the evaluation of the characteristic fire diameter $D^*(m)$, computed using the following equation:

$$D^* = \left(\frac{Q}{\rho\, c_p T_\infty \sqrt{g}}\right)^{\frac{2}{5}} \tag{3.6.1}$$

with Q heat release rate of fire (W), c_p air specific heat capacity at constant pressure $\left(1005 \frac{J}{kg\, K}\right)$, ρ air density $\left(1.225 \frac{kg}{m^3}\right)$, and T_∞ ambient temperature in Kelvin $(293.15\ K)$. The base size of the spatial grid Δx can be related to D^*: the smaller the characteristic fire diameter the smaller the cell size to reasonably solve the fluid flow and fire dynamics. Depending on the specific case under investigation, the ratio between characteristic fire diameter and cell size $\frac{\Delta x}{D^*}$ must be in the range $\frac{1}{20}$ - $\frac{1}{5}$ to ensure that the plume is modeled with at least a moderate level of accuracy [37]. The characteristic fire diameters obtained for the hydrogen and traditional gasoline-powered car based simulations are, respectively, 3.42 m and 2.07 m. It means that in the hydrogen car based simulation the cell size must be selected in the range 0.171 m - 0.685 m, while in the fossil fuel-powered car based simulation in the range 0.104 m - 0.415 m. The lower characteristic fire diameter in the case

of gasoline car based simulation, and hence the lower base size range on which basing the mesh building, is due to the lower heat release rate, which requires a higher number of computational cells spanning D^*. As anticipated before, the characteristic fire diameter is only a brief starting tool to establish the size of the spatial grid to be adopted, in fact the results achieved choosing an arbitrary cell dimension within the prescribed range $\frac{1}{20} < \frac{\Delta x}{D^*} < \frac{1}{5}$ cannot be considered as definitive, thus a grid sensitivity analysis is carried out to ensure stable and accurate results. Moreover, in fire applications it is not suitable to adopt a uniform grid distribution, since close to the fire sources there are large gradient temperature changes to be captured thanks to enough refined meshes, quite the opposite not necessarily needed far from the fire source. For this reason, a non-uniform mesh is considered for the purpose of the present work, with a lower cell base size near the burning zone, represented by the central part of the computational domain, and a higher base size close to the road tunnel entrance and exit. In this way it is possible to obtain an accurate fire simulation in the area where the burning car is located, which is the most interesting in data obtaining, as well as a not unadvisable number of total computational cells to discretize the domain. In particular, the refined mesh is adopted for a 100 m long central tunnel section, while the coarse grid for the 75 m upstream and downstream. To perform the grid sensitivity analysis, whose results are presented in figures 3.6.1 and 3.6.2, seven base sizes evenly spaced in the range prescribed by the characteristic fire diameter technique are considered to solve the problem under investigation, for both hydrogen and gasoline car based simulations. The sensitivity of the simulation setup to the spatial discretization parameter is investigated taking as reference the maximum gas phase temperature reached in the road tunnel in the target time domain, hence named the grid independence parameter.

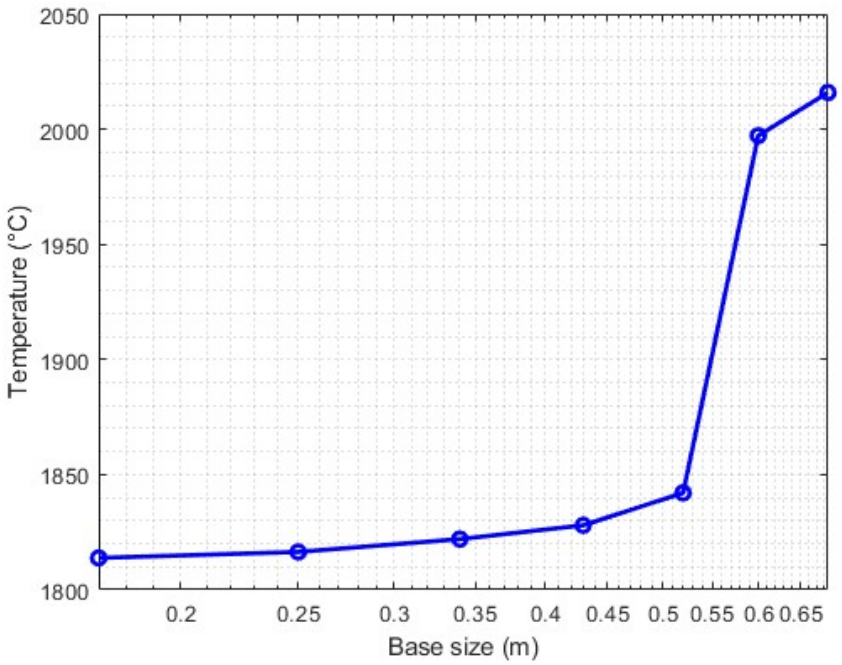

Fig. 3.6.1. Grid independence for hydrogen powered car based simulation.

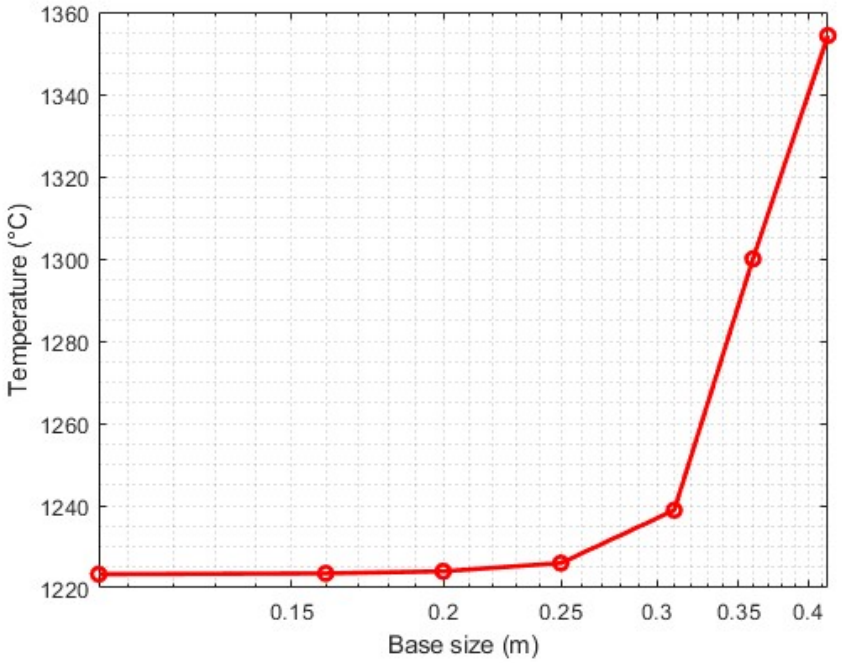

Fig. 3.6.2. Grid independence for gasoline powered car based simulation.

It is important to underline that the base sizes included in the two figures above refer to the dimension of the cells used in the refined section of the mesh, as it is the one in which the burning car is located and thus the one in which the maximum of temperature takes place. As shown by figures 3.6.1 and 3.6.2 the grid independence parameter, plotted in logarithmic scale on x axis, decreases as the base size decreases, reaching a plateau for base sizes equal or lower 0.25 m for both hydrogen and gasoline-powered car based simulations. The quite flat shape of the maximum gas phase temperature for the smaller cell dimensions implies that a base size of 0.25 m in the dense part of the computational domain (denoted as mesh 2) guarantees accurate results for both the simulations of interest, being therefore the one chosen in the present work. On the other hand, the cell size in the two parts of the domain closest to the tunnel entrance and exit (denoted, respectively, as mesh 1 and mesh 3) is set twice 0.25.
A summary of the spatial discretization scheme adopted, resulting in a 950000 total number of computational cells, is available in tab. 3.6.1.

	Tunnel stretch length (m)	Base size (m)	Number of cells
Mesh 1	0 – 75	0.5	75000
Mesh 2	75 – 175	0.25	800000
Mesh 3	175 – 250	0.5	75000

Tab. 3.6.1. Spatial discretization scheme adopted.

The non-uniform spatial grid used to discretize the computational domain is sketched in the following figures in top view, including a zoomed section near the mesh alignment.

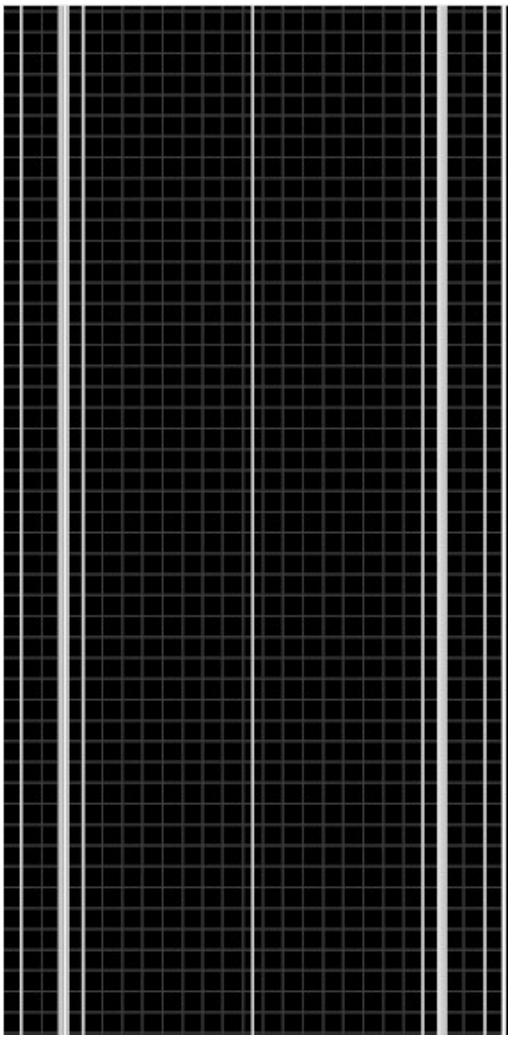

Fig. 3.6.3. Coarser mesh sketch.

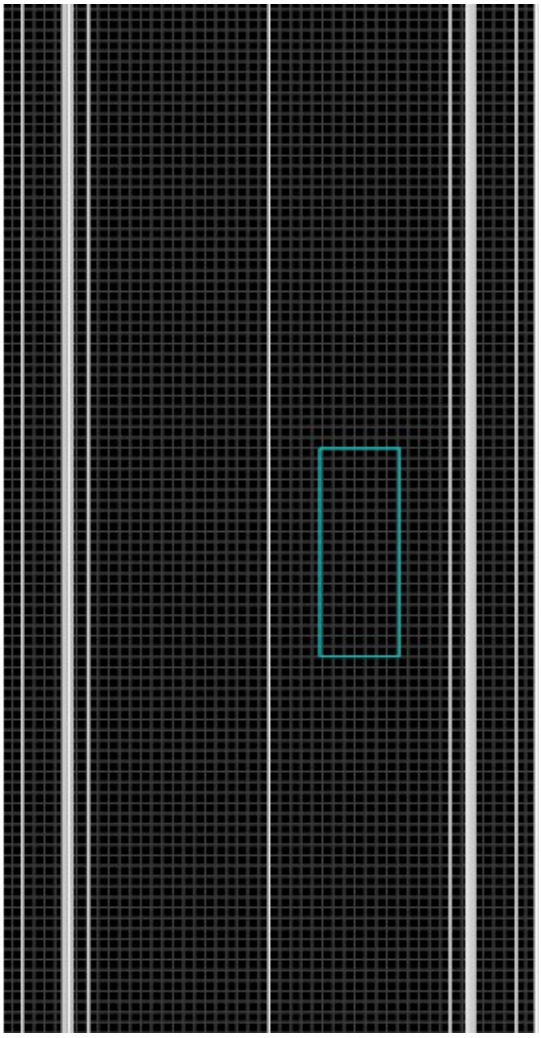

Fig. 3.6.4. Refined mesh sketch.

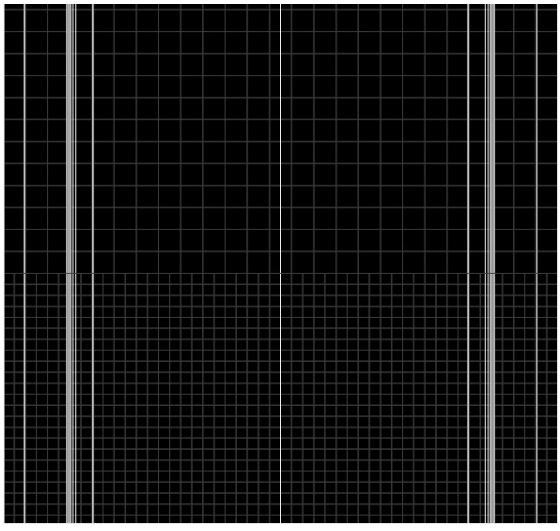

Fig. 3.6.5. Mesh alignment zoomed sketch.

It is important to specify that in FDS the mesh alignment must respect a fundamental rule: the abutting cells ought to have the same cross sectional area, or integral ratios. The kind of alignment reported in fig. 3.6.5, the one used in the simulation setup, is allowed so long as there are an integral number of fine cells abutting each coarse cell. In the present case, of course, this constraint is satisfied.

To conclude this section the setting of the time bounds is analysed. The time duration of the simulation is set to 600 s, as it is the maximum estimated time from the start of the fire after which there is no possibility of survival for the occupants not rescued. The time step used to advance the solution of the discretized equations, up to the end of the temporal domain, is not a fixed parameter in the Fire Dynamic Simulator, rather is adjusted during the calculation so that the CFL condition is satisfied. In fact, FDS uses an explicit time advancement scheme, hence, the time step plays an important role in maintaining numerical stability and accuracy [19]. The CFL (Courant-Friedrichs-Lewy) constraint aforementioned is given by the relation (3.6.2):

$$CFL = \delta t \frac{\|u\|}{\delta x} < 1 \tag{3.6.2}$$

with δt and δx, respectively, time step and cell base size in the spatial discretization, and u advection velocity. The CFL condition places a restriction on the time step due to the advection velocity and its minimum and maximum limits are set by default to, respectively, 0.8 and 1. From a physical point of view, this constraint establishes that a fluid element cannot traverse more than one cell within a prescribed time step. The default value of the initial time step size in FDS is set as follows:

$$\delta t_{initial} = \frac{5(\delta x \delta y \delta z)^{\frac{1}{3}}}{\sqrt{gH}} \tag{3.6.3}$$

in which δx, δy, and δz are the dimensions of the smallest mesh cell, and H the height of the computational domain. By default, the time step is never allowed to increase above its initial value, that according to the (3.6.3) is 0.125 s for the adopted simulation setup. This value is sufficient small to capture the accurate flame temperature distribution in the transient.

Results and discussions

The purpose of this section is to present the achieved results for the various simulations carried out on the reference case study. The results of the fire scenario caused by the HFCV are presented first, followed by those of the scenario produced by the traditional fossil fuels powered car. Finally, the variation of the output quantities of interest is analyzed for the HFCV case with modification of the boundary conditions of the problem, i.e. with the adoption of longitudinal ventilation inside the road tunnel using jet fans.

4.1 HFCV based simulation

The heat release rate for the fire produced by the HFCV, according to the modelling described in the subchapter 3.4, is characterized by a quadratic growth in the first 5 seconds of the simulation transient, after which it assumes an almost steady state behavior for the entire time domain considered. The average value which the HRR settles is 24.5 MW, with oscillations in the range 23-26 MW. Its trend, reported in fig. 4.1.1, is of considerable importance as it also influences other physical quantities, including above all the temperature of the gas phase inside the road tunnel. A zoomed view of the HRR evolution immediately following the fire ignition is also included, to fully understand its shape in the most interesting part of the transient.

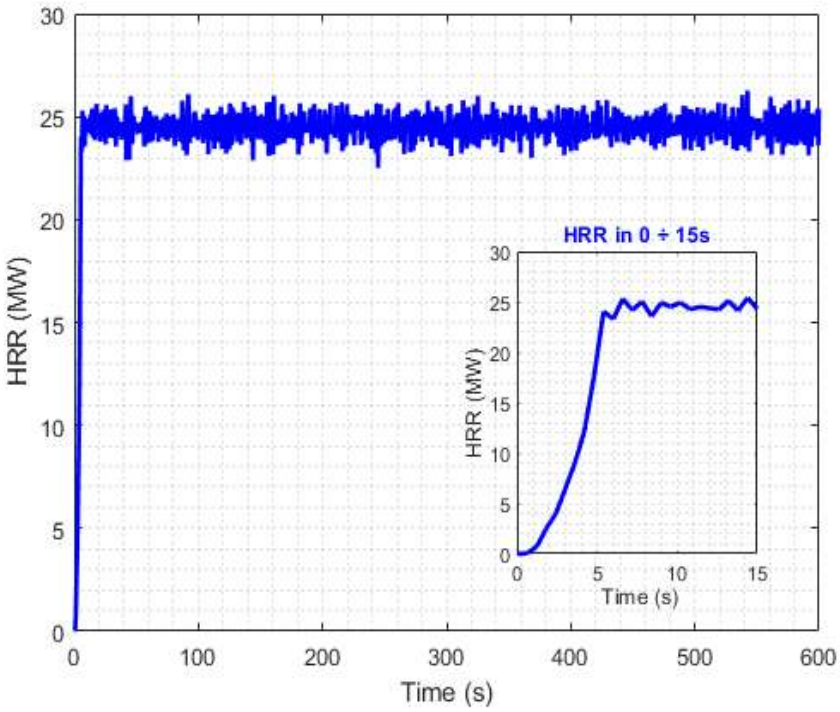

Fig. 4.1.1. HRR evolution for HFCV.

To compute the temperature evolution and distribution inside the road tunnel, 37 thermocouples distributed along the entire center line in correspondence with the ceiling are used, distributed more in the fire area and less away from it. The evolution of ceiling temperature in the reference time domain of the simulation at fire source (125 m from the tunnel entrance), and at 5 m, 10 m, 50 m, and 125 m from it, for the hydrogen fuel cell vehicle fire scenario, is shown in fig. 4.1.2.

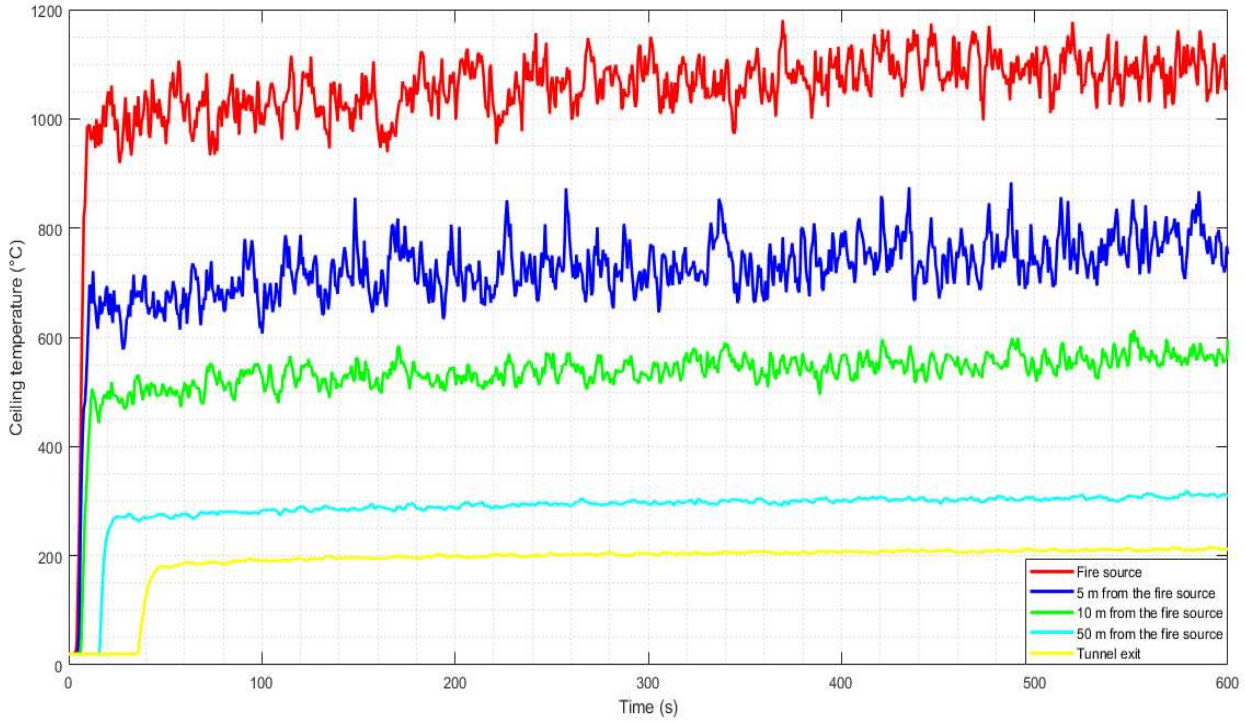

Fig. 4.1.2. Ceiling temperature evolution of the gas phase for HFCV.

Following the hydrogen ignition at time zero, the fire, thus the temperature behavior, increases very rapidly until the maximum heat release rate is accomplished. The temperature profiles achieve a quasi steady-state at roughly 10 s (red, blue, and green curve), 20 s (pale blue curve), and 40 s (yellow curve), depending on the distance from the burning car, setting up in this state for all the rest of the reference time domain. The greater the distance from the fire source, the greater the time in which the quasi-steady state condition is reached, due to the higher time required to attain the peak HRR for that specific area in case of greater distances from the fire itself. The mean ceiling temperature, in the quasi steady-state period of the transient, stands at about 1050 °C, 725 °C, 540 °C, 290 °C, and 190 °C, respectively at the fire source, at 5 m from it, at 10 m from it, at 50 m from it, and at the tunnel exit. It is worth mentioning that, due to the geometrical symmetry conditions of the tunnel as well as of the car inside it, and due to the boundary conditions set for the problem under investigation (i.e. no ventilation sources), the temperature evolutions are perfectly specular, at the same distance, both upstream and downstream of the fire source.
In figures from 4.1.3 to 4.1.13 are shown the temperature distributions on the longitudinal plane section at X = 8.42 m (4.1.3, 4.1.4, 4.1.5, 4.1.6), cross plane section Y = 125 m (4.1.7, 4.1.8, 4.1.9, 4.1.10), and horizontal plane section Z = 7 m (4.1.11, 4.1.12, 4.1.13) of the Virgolo road tunnel for different instants of time in the case of HFCV fire scenario.

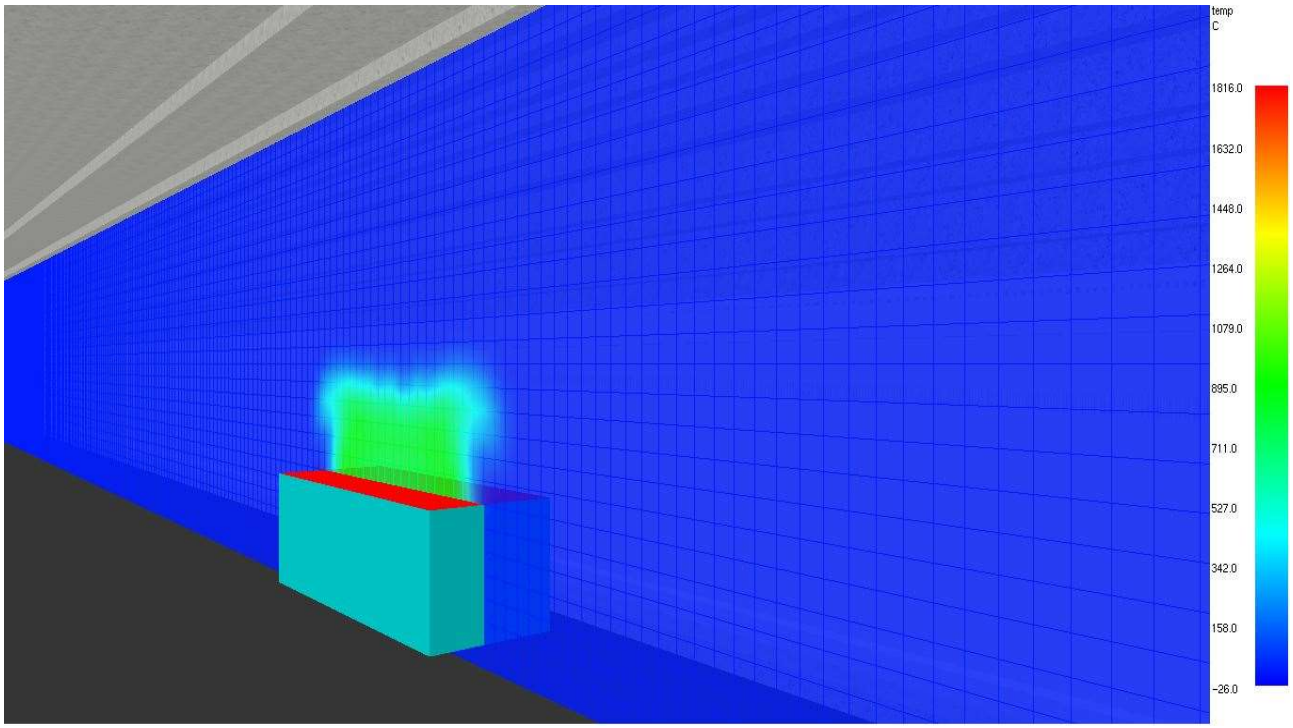

Fig. 4.1.3. 2D temperature map on plane X = 8.42 m at t = 2.5 s for HFCV.

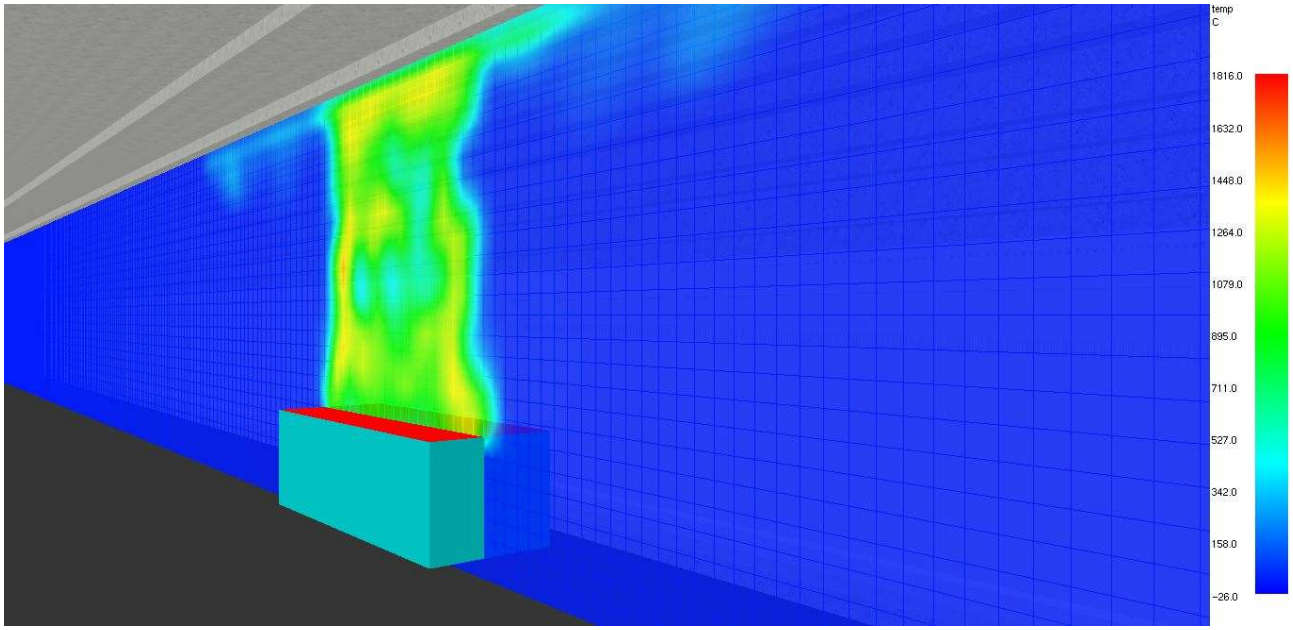

Fig. 4.1.4. 2D temperature map on plane X = 8.42 m at t = 5 s for HFCV.

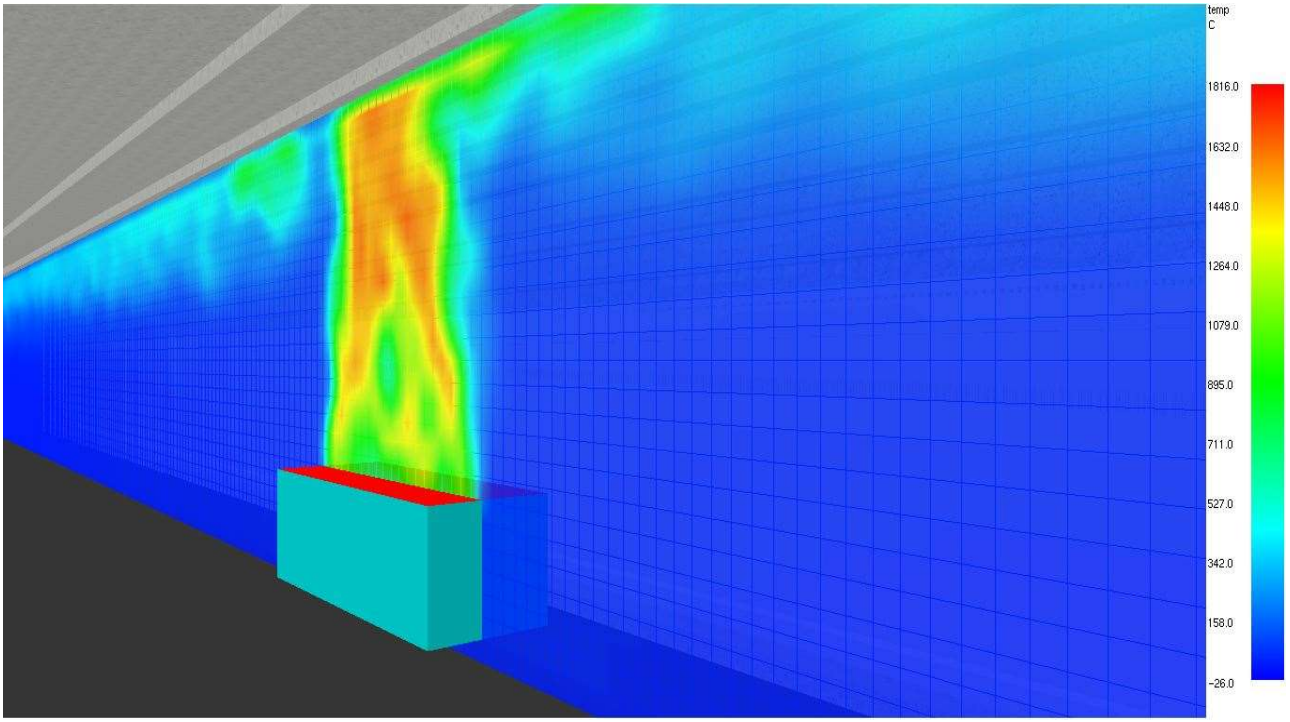

Fig. 4.1.5. 2D temperature map on plane X = 8.42 m at t = 60 s for HFCV.

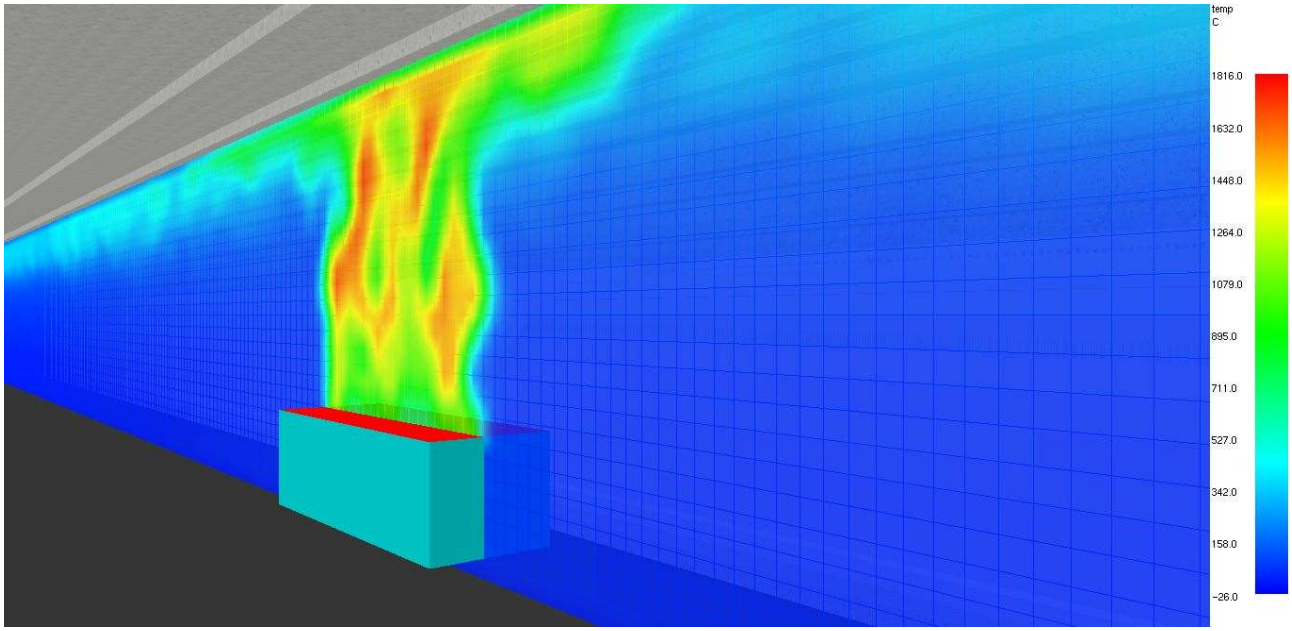

Fig. 4.1.6. 2D temperature map on plane X = 8.42 m at t = 600 s for HFCV.

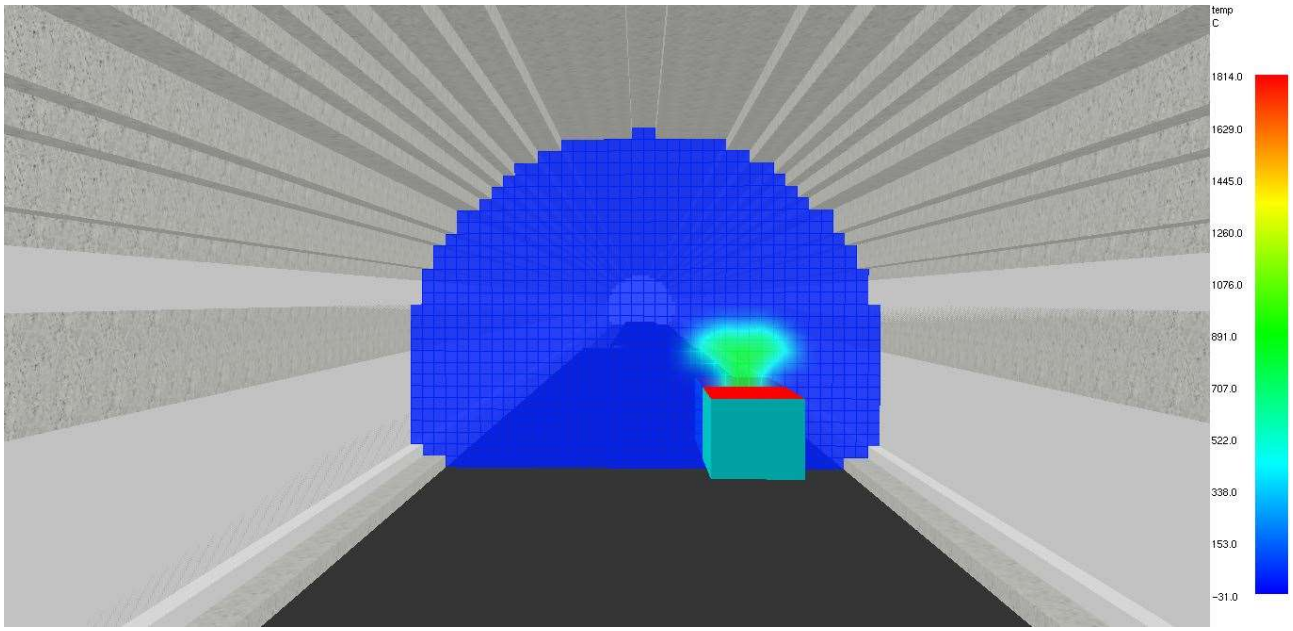

Fig. 4.1.7. 2D temperature map on plane Y = 125 m at t = 2.5 s for HFCV.

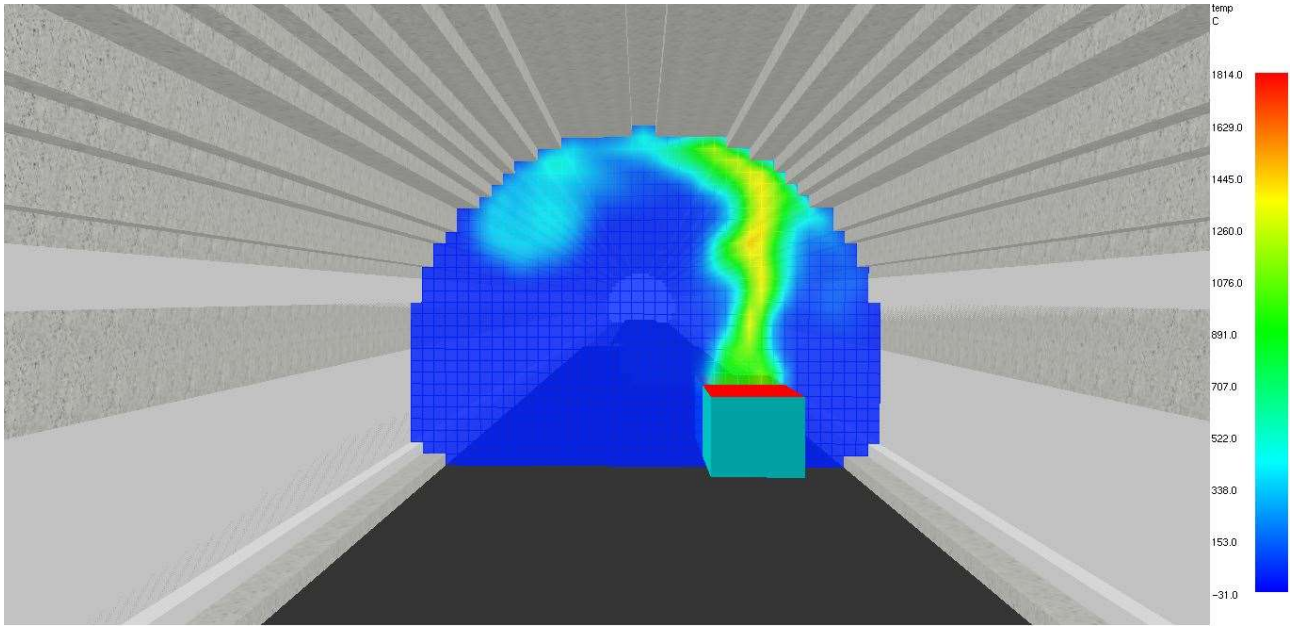

Fig. 4.1.8. 2D temperature map on plane Y = 125 m at t = 5 s for HFCV.

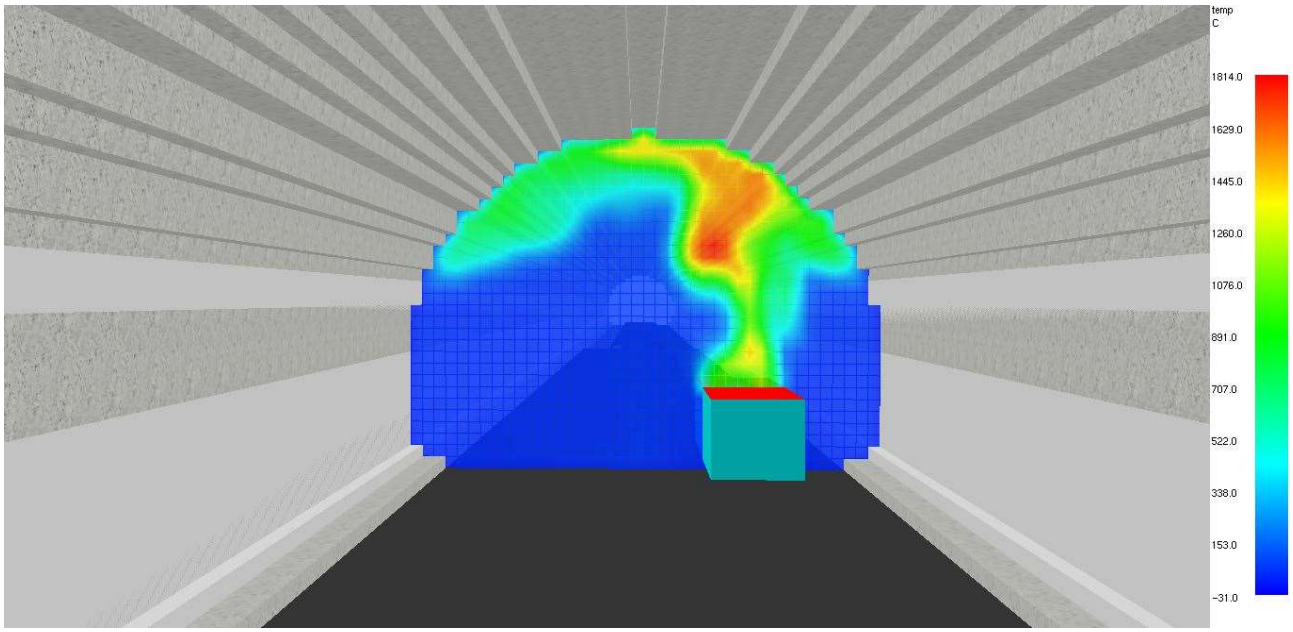

Fig. 4.1.9. 2D temperature map on plane Y = 125 m at t = 60 s for HFCV.

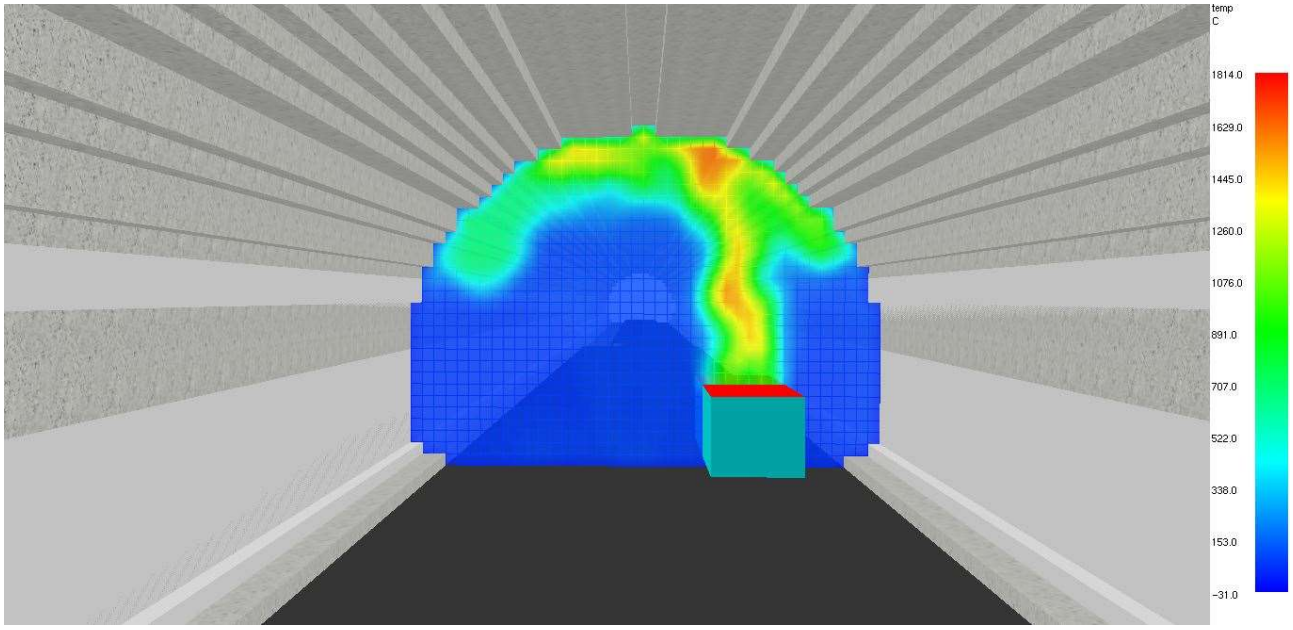

Fig. 4.1.10. 2D temperature map on plane Y = 125 m at t = 600 s for HFCV.

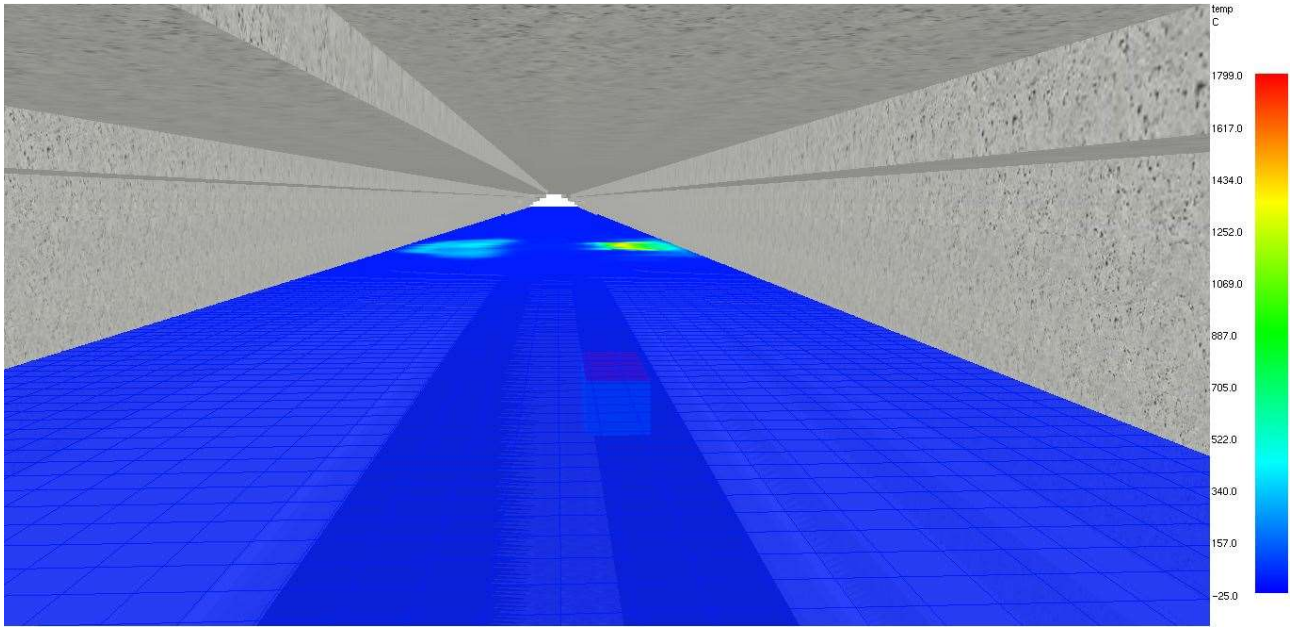

Fig. 4.1.11. 2D temperature map on plane Z = 7 m at t = 5 s for HFCV.

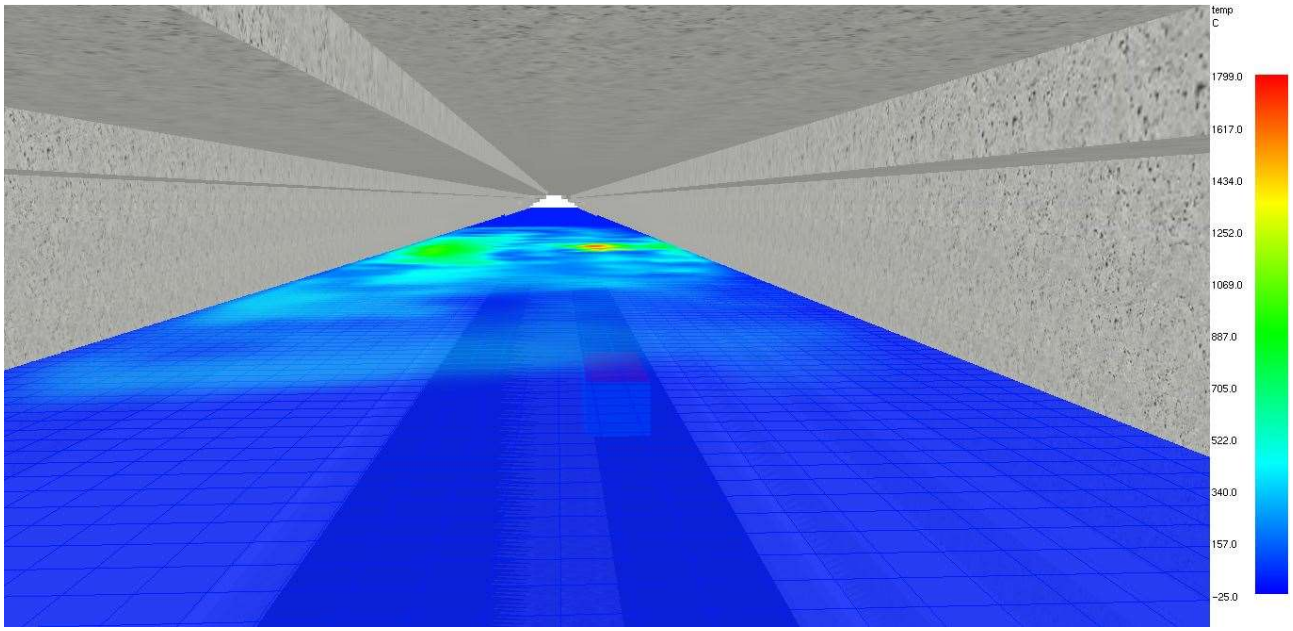

Fig. 4.1.12. 2D temperature map on plane Z = 7 m at t = 10 s for HFCV.

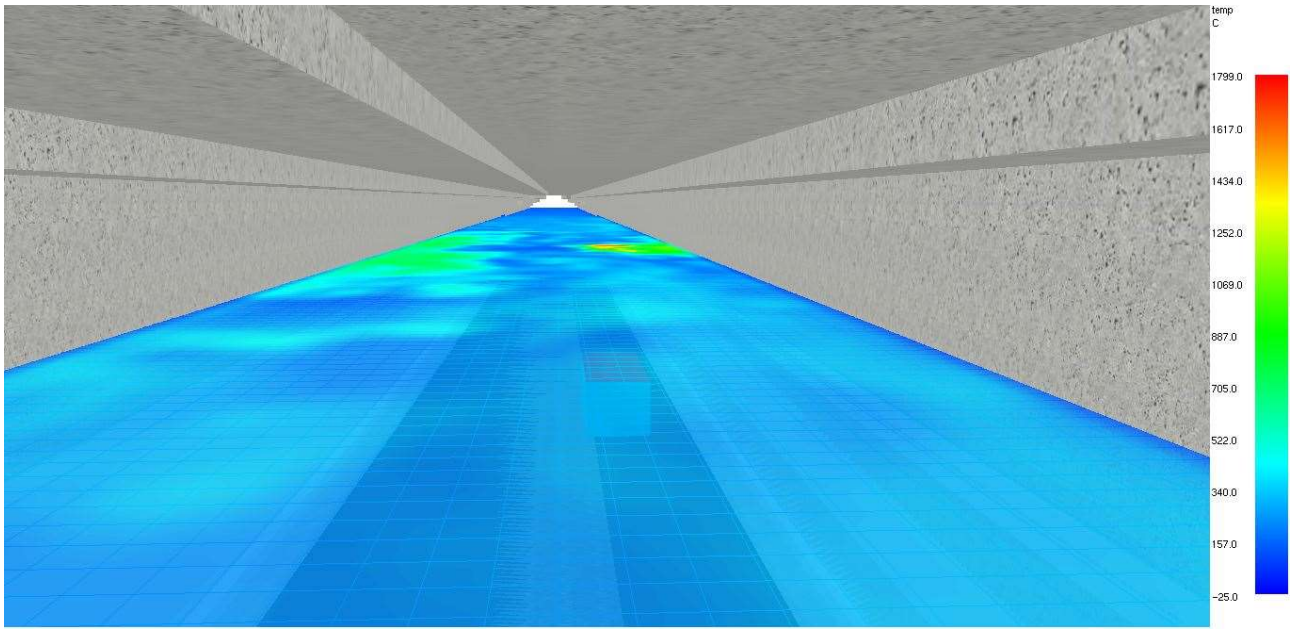

Fig. 4.1.13. 2D temperature map on plane Z = 7 m at t = 600 s for HFCV.

The 2D temperature slices reported in the previous figures show that the temperature maps increase as the transient goes by and, after a critical and very small time, roughly 5 s or 10 s depending on the considered section of the tunnel, do not change in an appreciable way. This quasi steady-state temperature behaviour, shown in particular by figures 4.1.5, 4.1.9, and 4.1.13 after that this critical time has been exceeded, is perfectly in agreement with which reported in fig. 4.1.2 concerning the ceiling temperatures evolution. The maximum temperature reached during the burning process is computed in 1816 °C, 1814 °C, and 1799 °C, respectively for the longitudinal, cross section, and horizontal plane of the road tunnel. For what concerns the planes X = 8.42 m and Y = 125 m, the highest slice temperature is not reached in correspondence of the vehicle surface, as one could expect, ad this is due to the non-premixed jet flame characteristics. In the aforementioned case, in fact, the air and the fuel (hydrogen) are initially separated and then, thanks to bulk convection and molecular diffusion, they unite to start reactions in the so-called reaction zone [31]. The entire region close to the burning object can be divided into 3 macro zones: a fuel rich (exactly on the car surface), an air rich (away from the car at the ceiling), and a reaction zone (in the middle) [38]. The maximum flame temperature of the gas phase is reached inside the reaction zone, and this is the reason for which the temperature at the outlet of the HFCV nozzle is not the higher in the reference fire space domain. This behaviour is considerably different with respect to the case of traditional fossil fuels powered car, as it will be discussed in the next subchapter. However, even if not the maximum ones, very high temperatures are recorded in correspondence with the ceiling and at the greater height zones of the road tunnel compared to the average of the longitudinal and transversal sections. This is due to the fact that, during the burning process, the light hot gaseous combustion products, as a consequence of the hydrogen high buoyancy in the air, move upstream towards the ceiling. Always close to the latter, as it is possible to appreciate starting from fig. 4.1.3 and up to 4.1.10, flames merge and, in addition, are also characterized by the wider extension with respect to the slices surface. It is quite obvious that this hydrogen flame collision, accompanied by high thermal stresses, may produce the crumble of the ceiling constituting materials, giving rise to a very dangerous situation for the structural integrity of the road tunnel. For this reason, in

subchapter 4.3, it will be investigated the adoption of ventilation strategies to attempt mitigating this phenomena. Regarding the 2D slices on the horizontal plane Z = 7 m, in agreement with figures 4.1.11, 4.1.12, and 4.1.13, it can be noted that the temperature map takes longer to reach the steady state condition than the other sections previously described. The hotspots in this plane place above the head of the vehicle, evolving first and more towards the left lane, with instead lower values upstream and downstream of the fire location.
The monodimensional temperature distribution in the entire tunnel length, computed taking advantage of the 37 thermocouples placed on the ceiling, is reported in fig. 4.1.14.

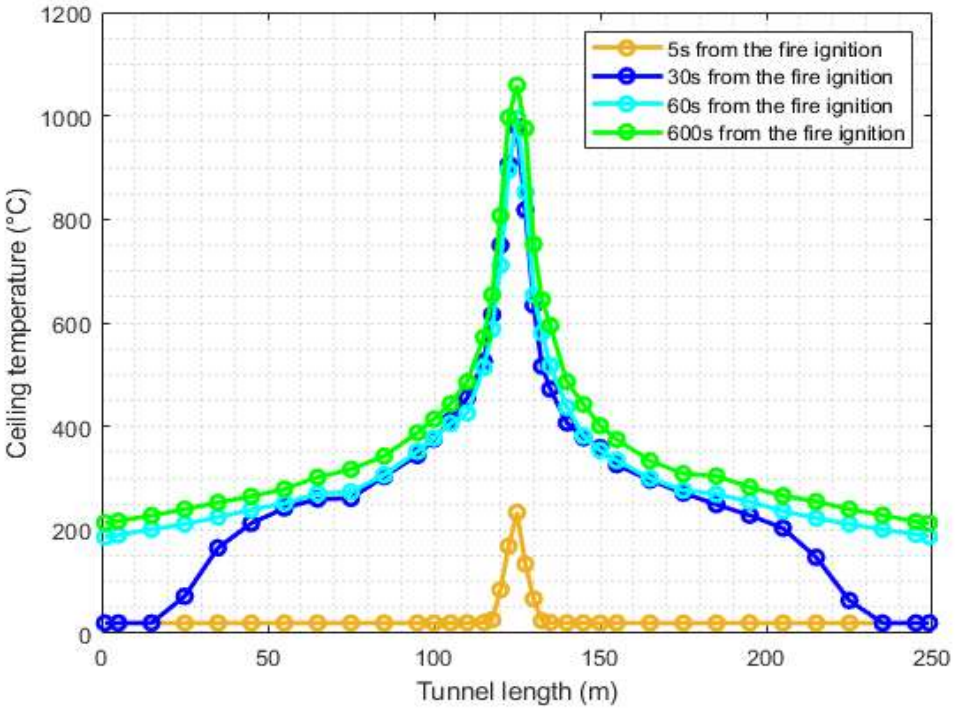

Fig. 4.1.14. Ceiling temperature distribution of the gas phase in the tunnel length for HFCV.

The peak ceiling temperature, as it was expected, is located at the car location, hence at 125 m from the tunnel entrance, being the place in which the heat release rate is the maximum one. This peak proved to be about 250 °C at 5 s from the fire ignition, 1000 °C at 30 s and 60 s from the fire ignition, and 1050 °C at the end of the transient. The temperature distribution, due to the previously made considerations on geometrical symmetry and boundary conditions set, is perfectly symmetrical to the left and right of the fire source, which is consistent with the physic of the problem. The ceiling temperature decreases with an exponential shape moving from the burning car to the tunnel exit, and, specularly, increases exponentially from the tunnel entrance towards its center. This exponential trend is valid once the steady state condition has been reached, while for instants of time below the critical one (i.e. the golden curve in the figure above) the temperature profiles increase and decrease with a shape more similar to a linear one. As depicted by fig. 4.1.14, starting from 30 s and for all the rest of the simulation duration, the temperature profiles are almost superimposable, especially in the tunnel stretch 50 m – 200 m. This confirms the low dynamics of the problem after the critical time, and is in agreement with the results achieved in terms of 2D temperature slice distributions.

Beyond the temperature evolution of the gas phase over the transient and its distribution in the tunnel length at various instants of time, it is interesting to show even the temperature evolutions at the wall surface of the ceiling, attached in fig. 4.1.15.

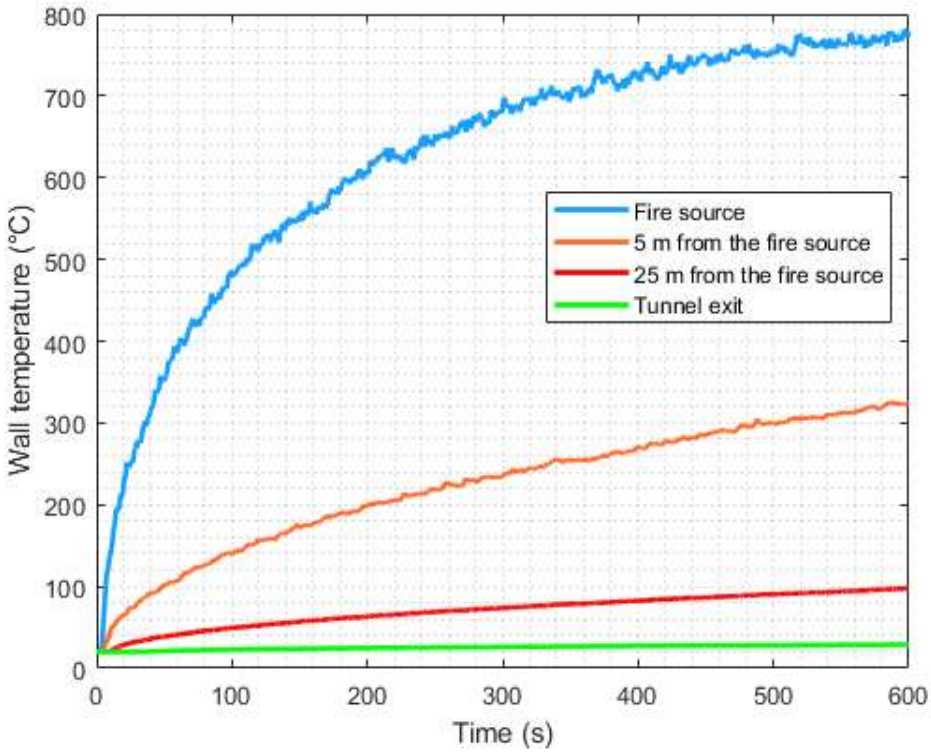

Fig. 4.1.15. Wall ceiling temperature evolution for HFCV.

To compute the wall temperature of the upper part of the road tunnel, solid phase devices are exploited. In particular, 3 sensors for each cross-section plane at ceiling (one in the middle of the left lane, one in the middle of the right lane, and one at the centerline) at regular distances from the fire source are used, averaging their output results to produce a single temperature value evolution representative of the ceiling solid phase wall temperature at different locations inside the tunnel. At the end of the transient the wall temperature reaches a value of nearly 780 °C, 320 °C, 100 °C, and 30 °C, respectively at the fire source, at 5 m from it, at 25 m from it, and at the tunnel exit. With respect to the gas phase temperature evolution, depicted in fig. 4.1.2, the wall temperature is characterized by a constant growing in the transient time, without reaching a steady state condition after a critical time and without, or almost, the temperature fluctuations that mark gaseous hydrogen combustion products. The lower the distance from the fire source the higher the temperature growth rate of the solid phase, as it is reasonably to be, due to the influence of the heat release rate in the space domain. Even though with a considerably greater growth speed, the wall temperature evolution has a sort of logarithmic trend, except for the green curve in fig. 4.1.15 (in correspondence of the tunnel exit) which does not have time to grow in the reference simulation interval, having thus an almost constant shape.

Another key quantity in the kind of problem under investigation is the propagation of hot smokes, which becomes stable in a small amount of time during the transient. The 3D smoke soot density is reported in figures 4.1.16, 4.1.17, and 4.1.18, at different instants of time.

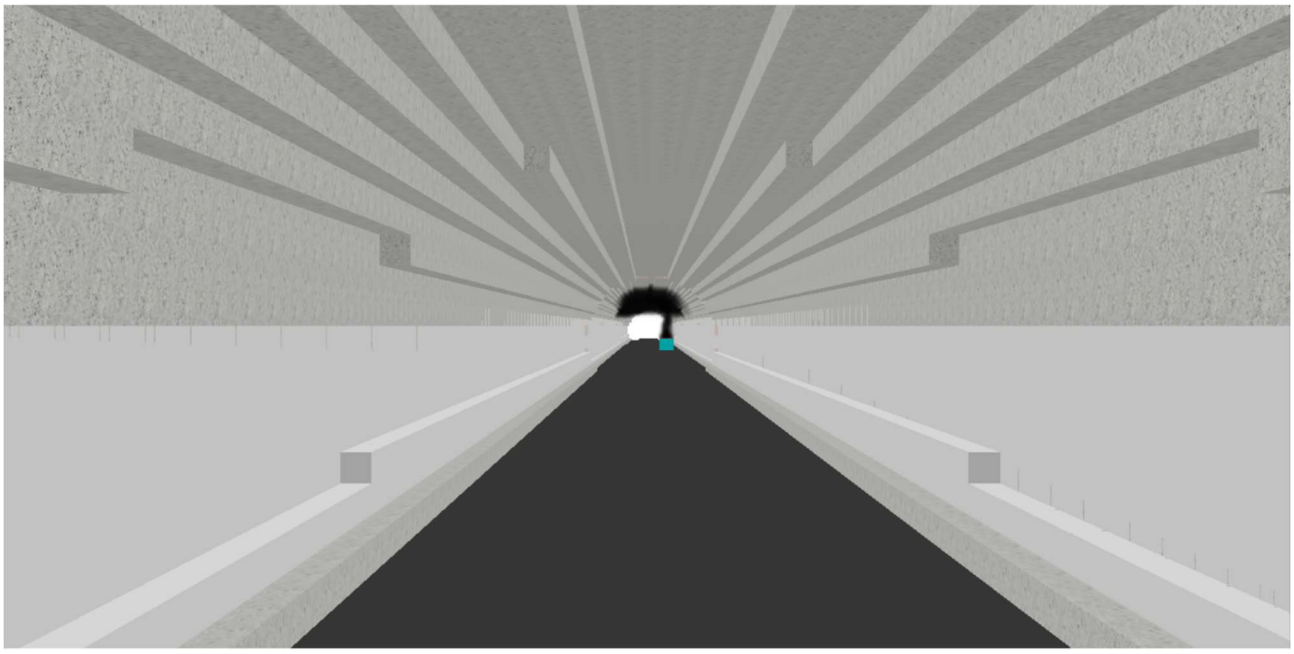

Fig. 4.1.16. Hot smokes distribution at t = 60 s for HFCV.

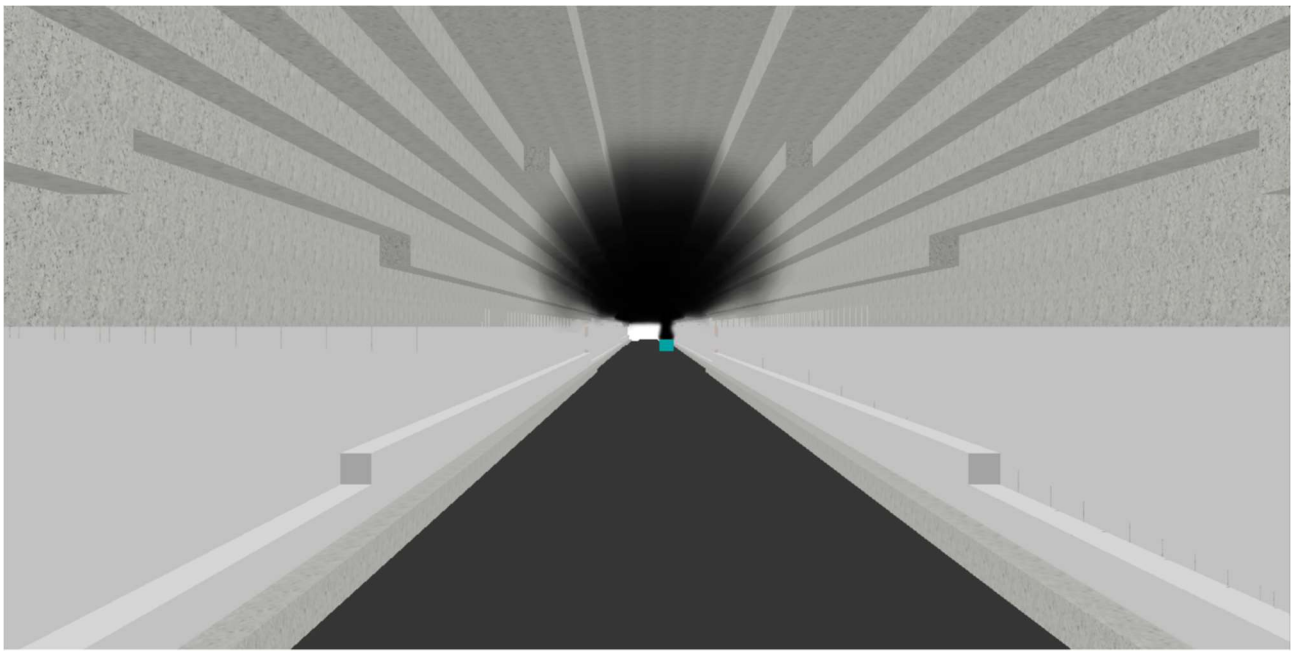

Fig. 4.1.17. Hot smokes distribution at t = 120 s for HFCV.

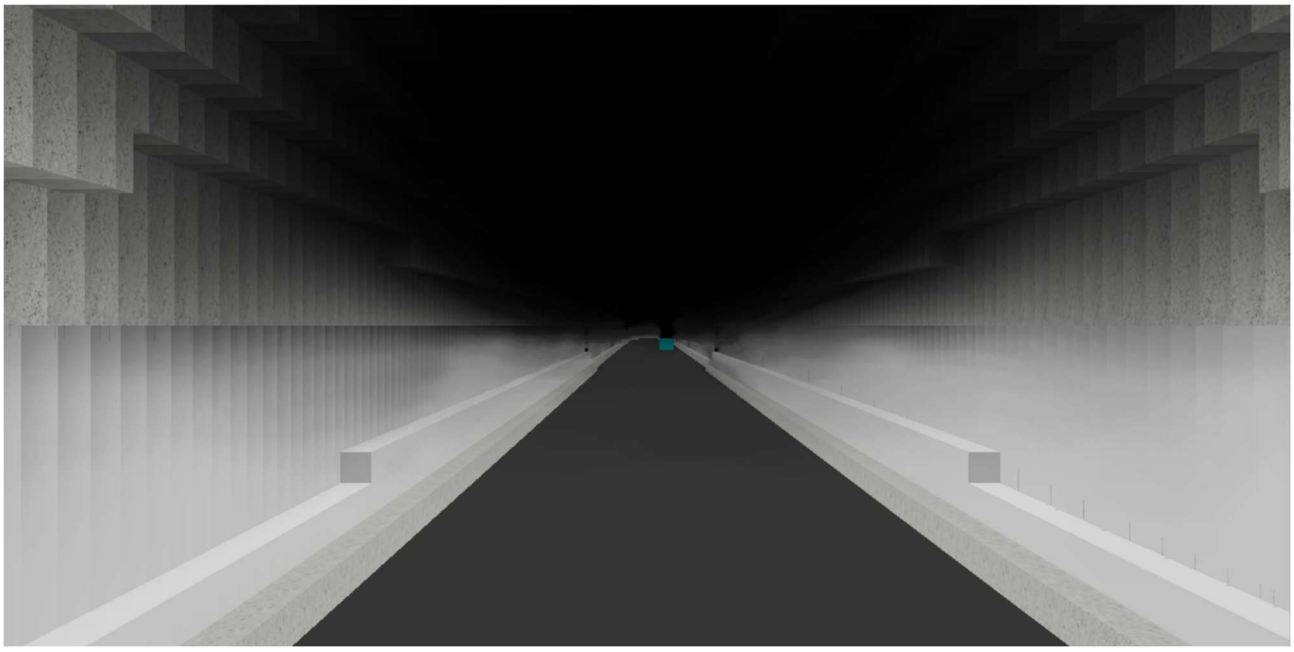

Fig. 4.1.18. Hot smokes distribution at t = 600 s for HFCV.

The relevance of hot smokes propagation lies in the fact that it influences the variation of the ceiling temperature, which is sensible to the smoke movement towards the under part of the road tunnel vault. The ceiling temperature, as discussed above, decreases in the sections away from the burning car and, after a given location inside the tunnel, decreases less than in areas closer to the fire source. The hot smokes, which are a post-combustion product of the burning object, move towards the ceiling, colliding with it and then returning to the tunnel ground, thanks to the inertial force coming from the released hydrogen jet. This inertial force, both back down and longitudinal, coupled with the thermal buoyancy ascent motion towards the ceiling, is responsible of the fluctuating shape with which the thermal plume moves towards the tunnel vault, which is well highlighted by fig. 4.1.2. Moreover, once the feeble back down inertial force is consumed, a monodimensional almost quite smoke flow comes to create in the longitudinal section of the tunnel.

Moving forward, the velocity distributions on longitudinal and cross plane sections of the road tunnel are included from fig. 4.1.19 to 4.1.26, reported as 2D vector slices to properly understand non only the modulus but also the direction of the velocity vectors.

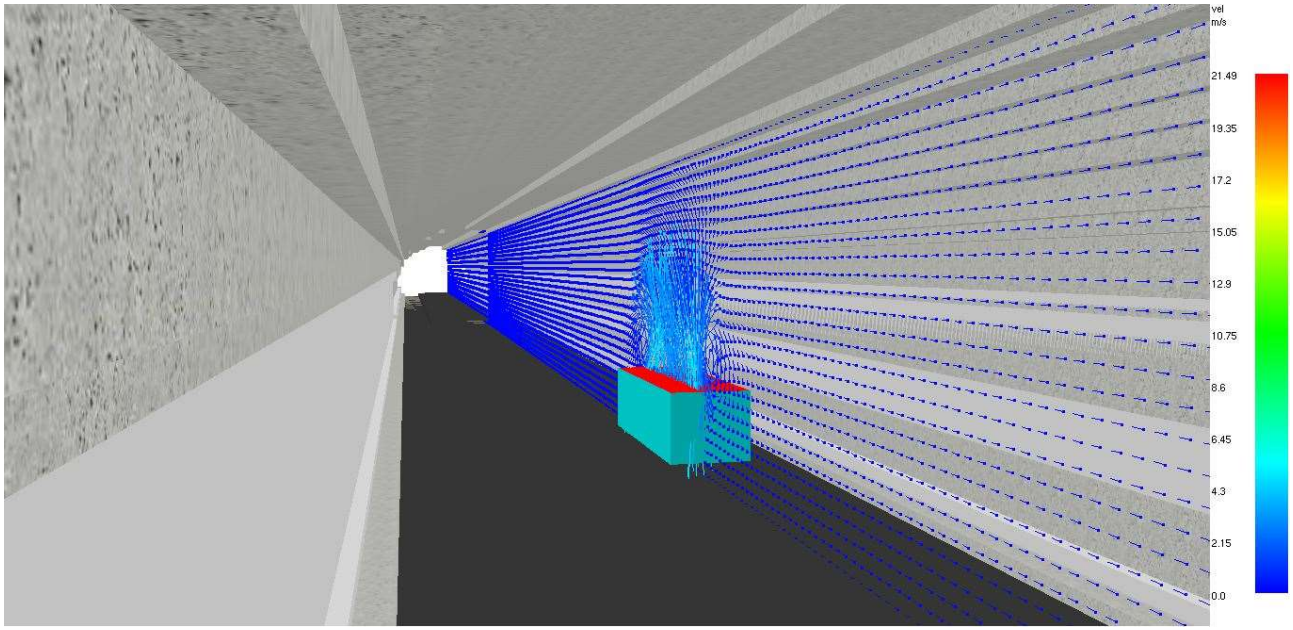

Fig. 4.1.19. 2D vector velocity map on plane X = 8.42 m at t = 2.5 s for HFCV.

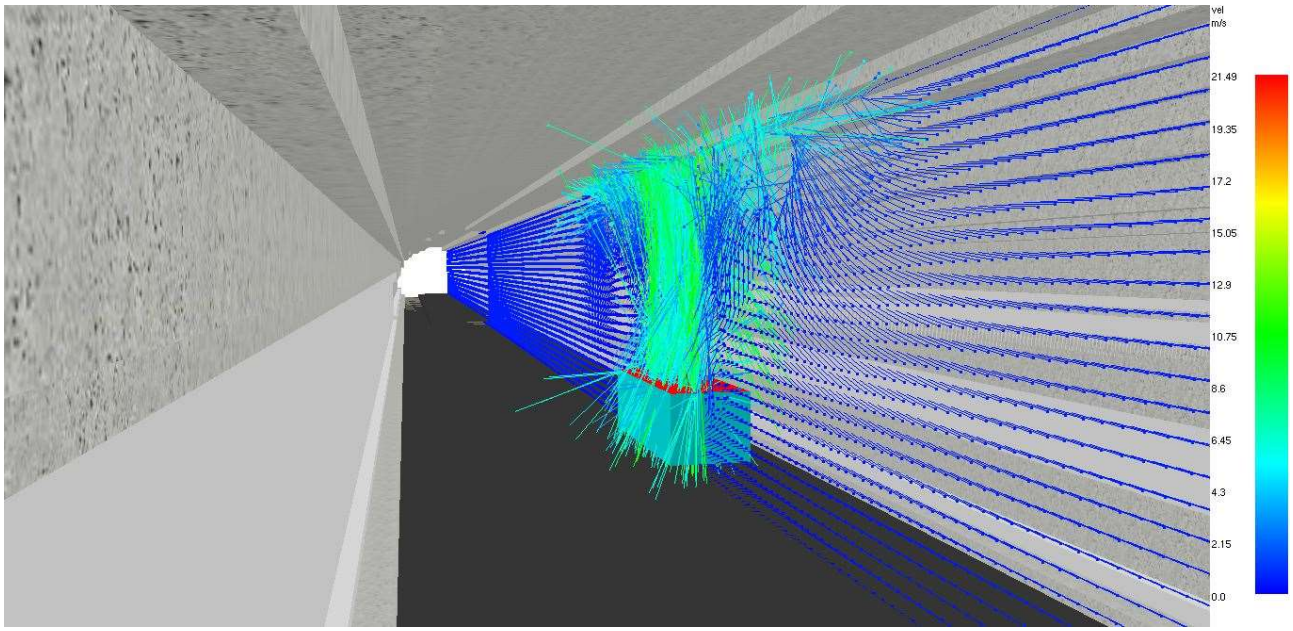

Fig. 4.1.20. 2D vector velocity map on plane X = 8.42 m at t = 5 s for HFCV.

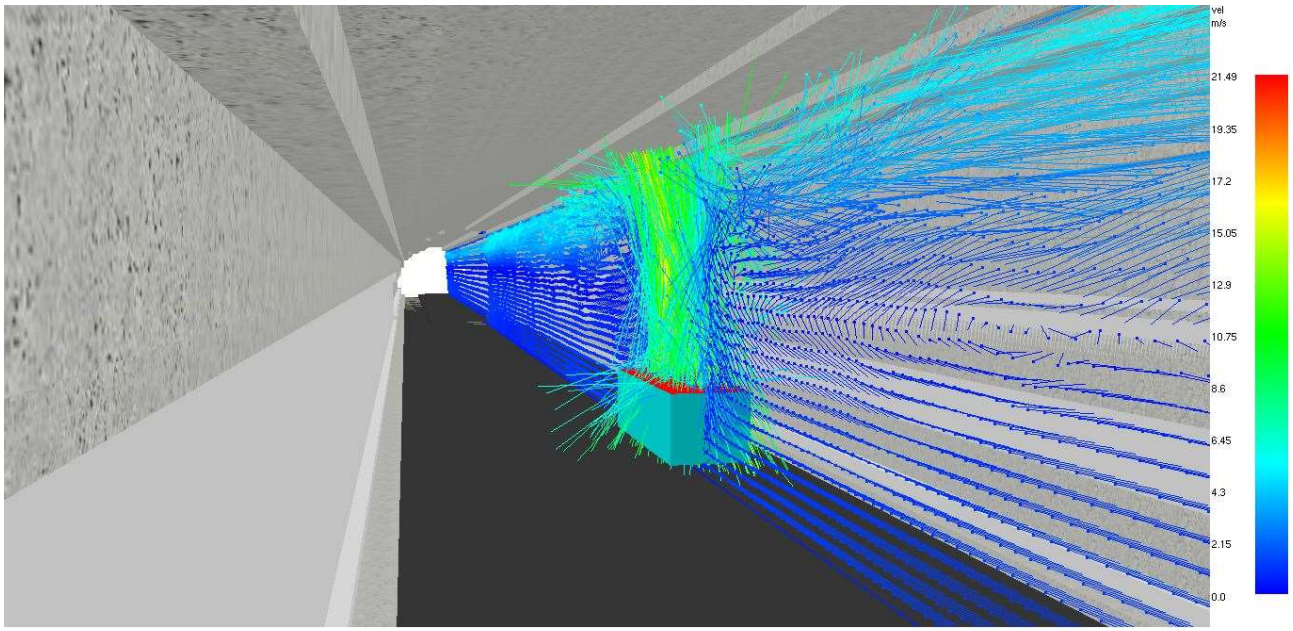

Fig. 4.1.21. 2D vector velocity map on plane X = 8.42 m at t = 60 s for HFCV.

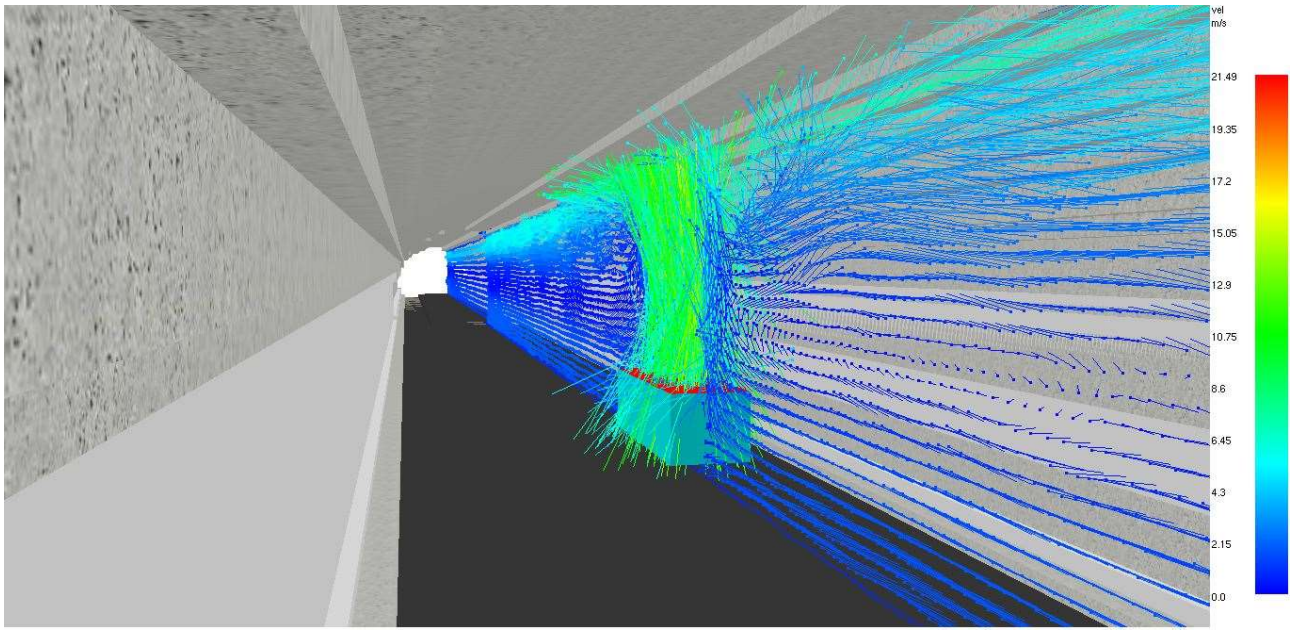

Fig. 4.1.22. 2D vector velocity map on plane X = 8.42 m at t = 600 s for HFCV.

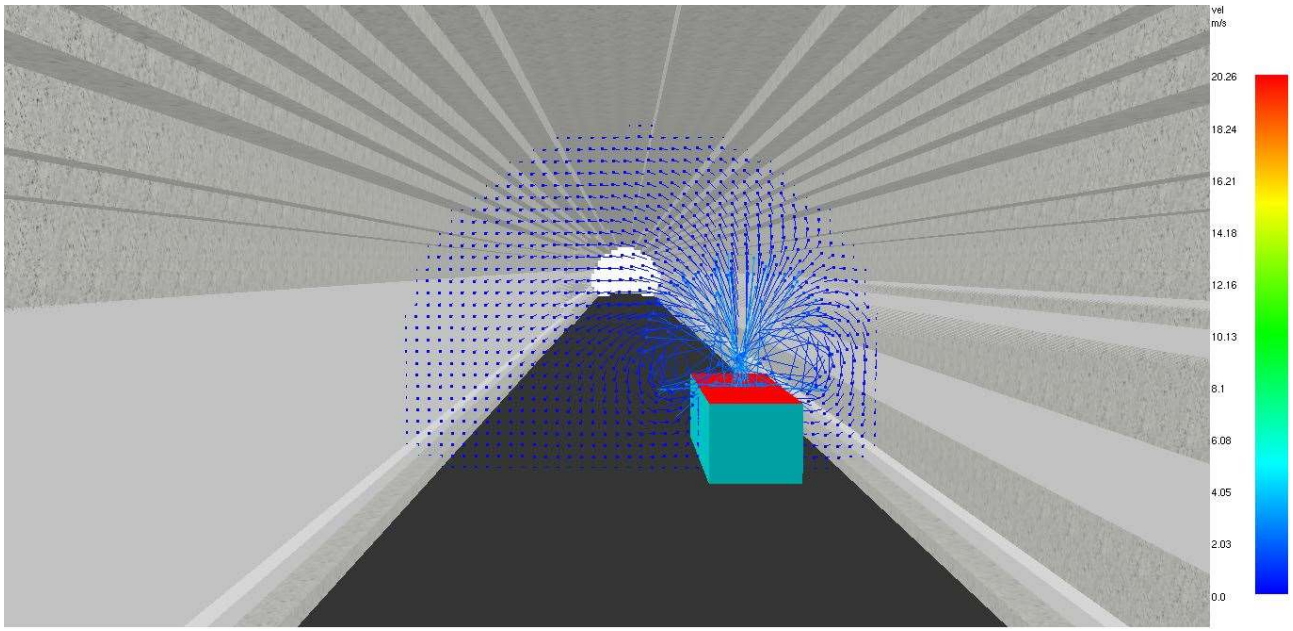

Fig. 4.1.23. 2D vector velocity map on plane Y = 125 m at t = 2.5 s for HFCV.

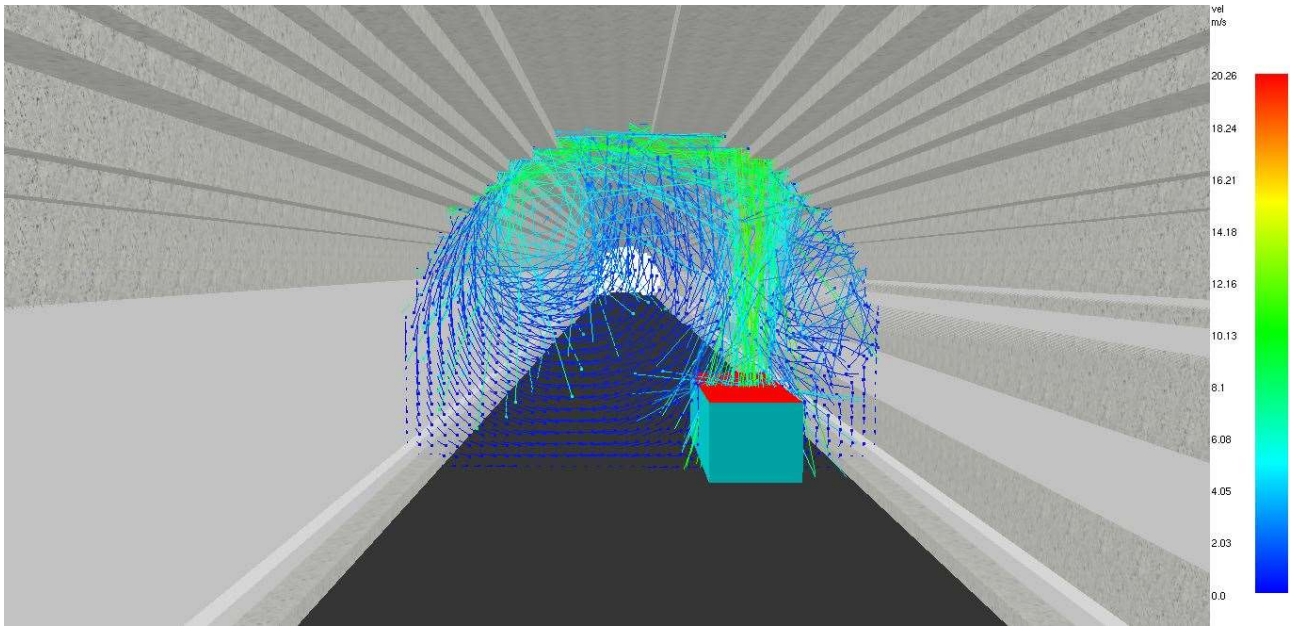

Fig. 4.1.24. 2D vector velocity map on plane Y = 125 m at t = 5 s for HFCV.

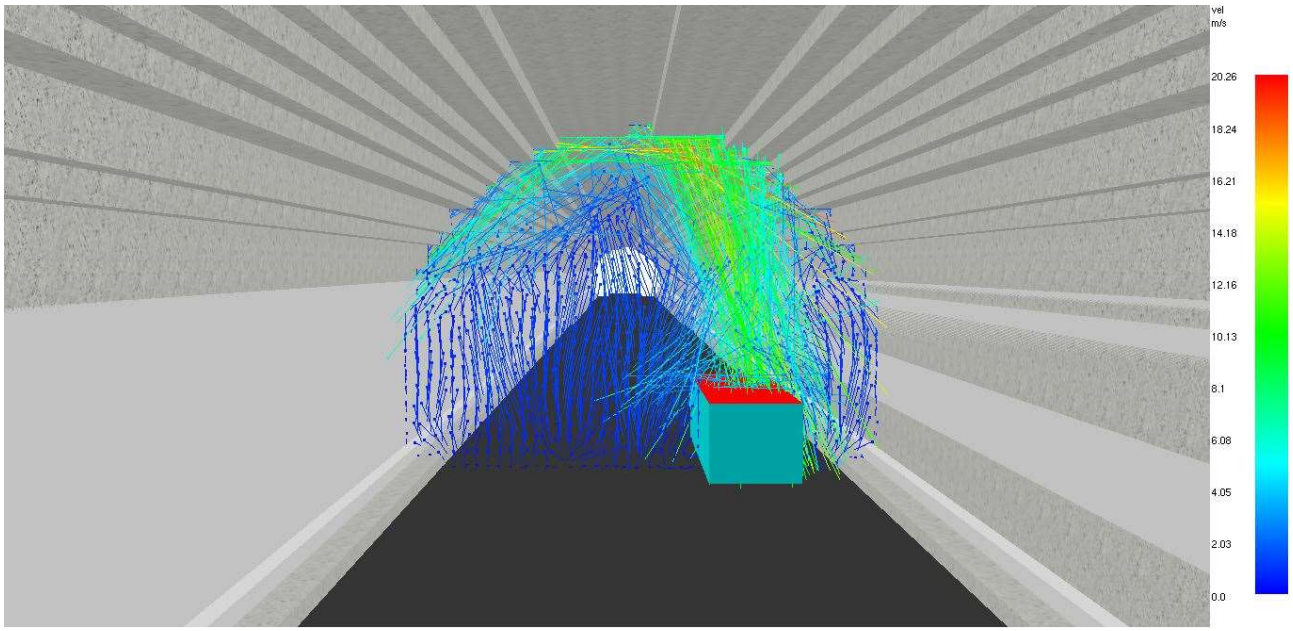

Fig. 4.1.25. 2D vector velocity map on plane Y = 125 m at t = 60 s for HFCV.

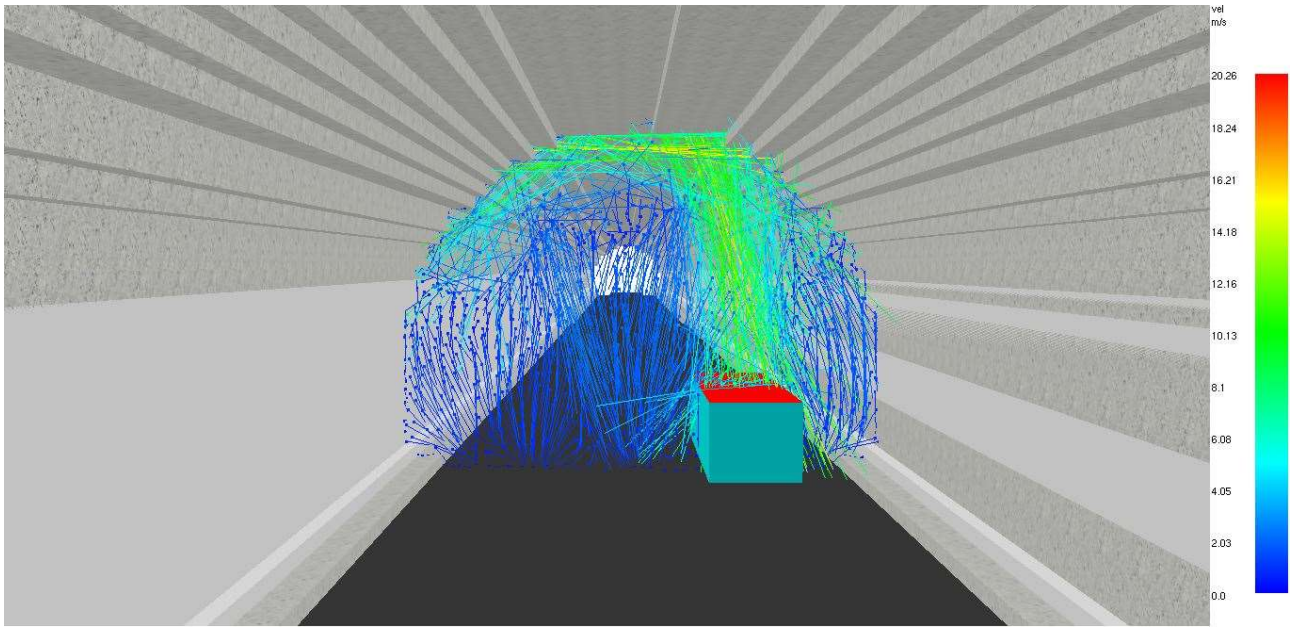

Fig. 4.1.26. 2D vector velocity map on plane Y = 125 m at t = 600 s for HFCV.

The velocity of the smokes flow, according to what depicted by the previous attached figures, stands at a mean value of roughly $9\ \frac{m}{s}$ in the region closer to the burning car and to the ceiling, and $2\ \frac{m}{s}$ elsewhere, for what concerns the tunnel cross plane section, while at a mean value of about $11\ \frac{m}{s}$ and $3\ \frac{m}{s}$ in the case of the longitudinal plane section. The maximum velocity values reached by the flow are, respectively for the plane Y = 125 m and X = 8.42 m, $20.3\ \frac{m}{s}$ and $21.5\ \frac{m}{s}$. The velocity of the smokes flow close to the fire summit increases very quickly in the transient time due to the

symmetrical ascending heat source force on both the left and right side of the road tunnel. The thermal buoyancy, coupled with the inertial force carried out by the hydrogen jet, the latter characterized by a high outer speed from the nozzle, is responsible of the smokes fast motion, increasing their velocity values next to the burning HFCV and to the ceiling. Moreover, the aforementioned forces at play are even responsible for breaking the symmetry of the vortex on both sides of the burning vehicle. This occurrence ensures a non-symmetrical distribution of the hot smokes to the left and to the right, with respect to the vertical section plane, of the fire location. Similarly to the 2D temperature profiles evolution, the velocity of the smokes flow is characterized by an almost steady state behaviour during the transient after that a critical time is reached, the latter being equal to 5 s.

To properly understand, and clearly visualize, the evolution of the combustion process inside the road tunnel, the heat transfer coefficient on all the walls of the tunnel itself is also considered. Its distribution, in the form of 3D plots at the instants of time 2.5 s, 5 s, 60 s, and 600 s, is attached below.

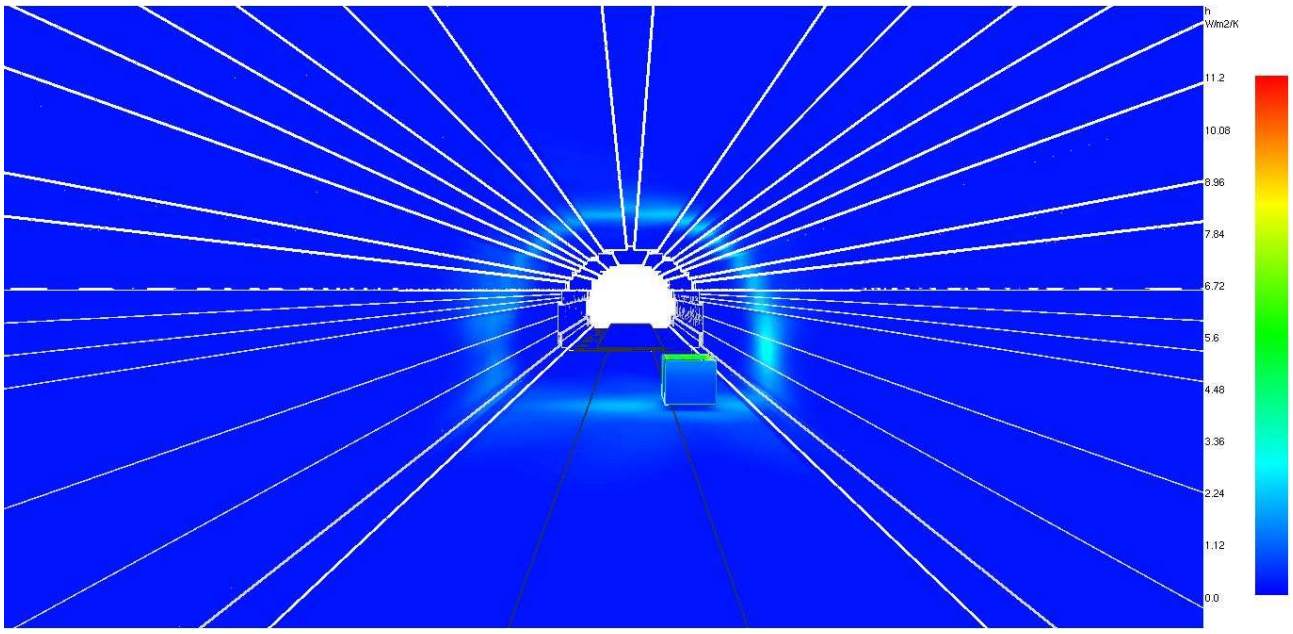

Fig. 4.1.27. Heat transfer coefficient distribution at t = 2.5 s for HFCV.

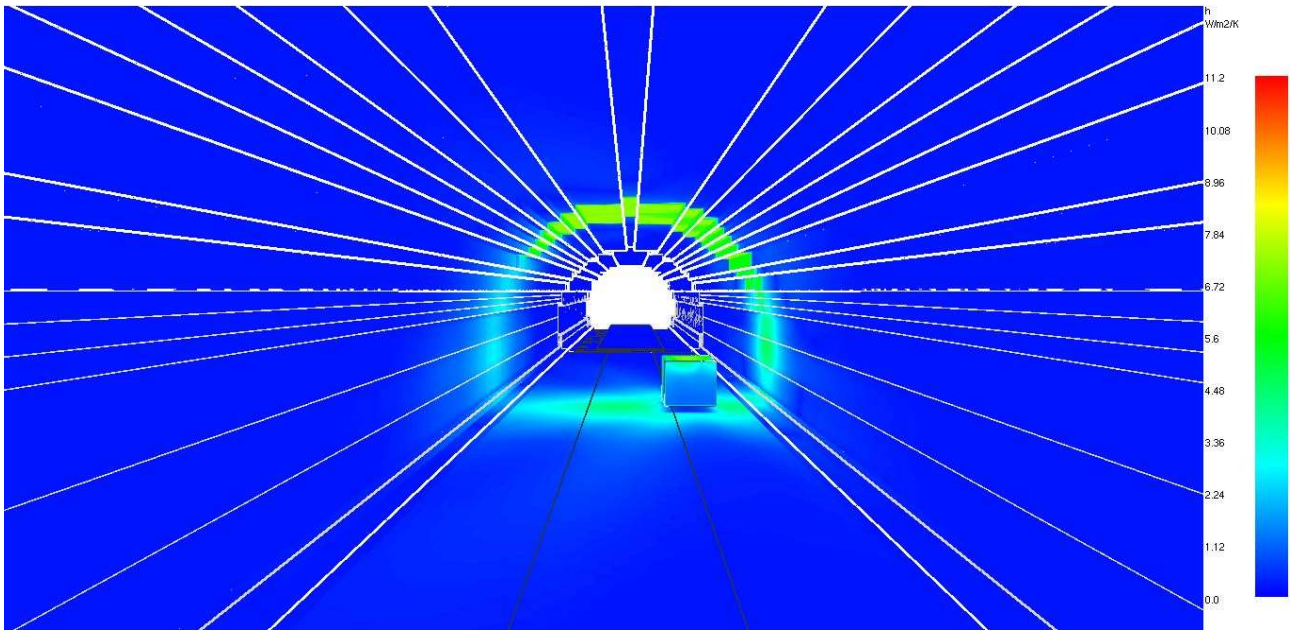

Fig. 4.1.28. Heat transfer coefficient distribution at t = 5 s for HFCV.

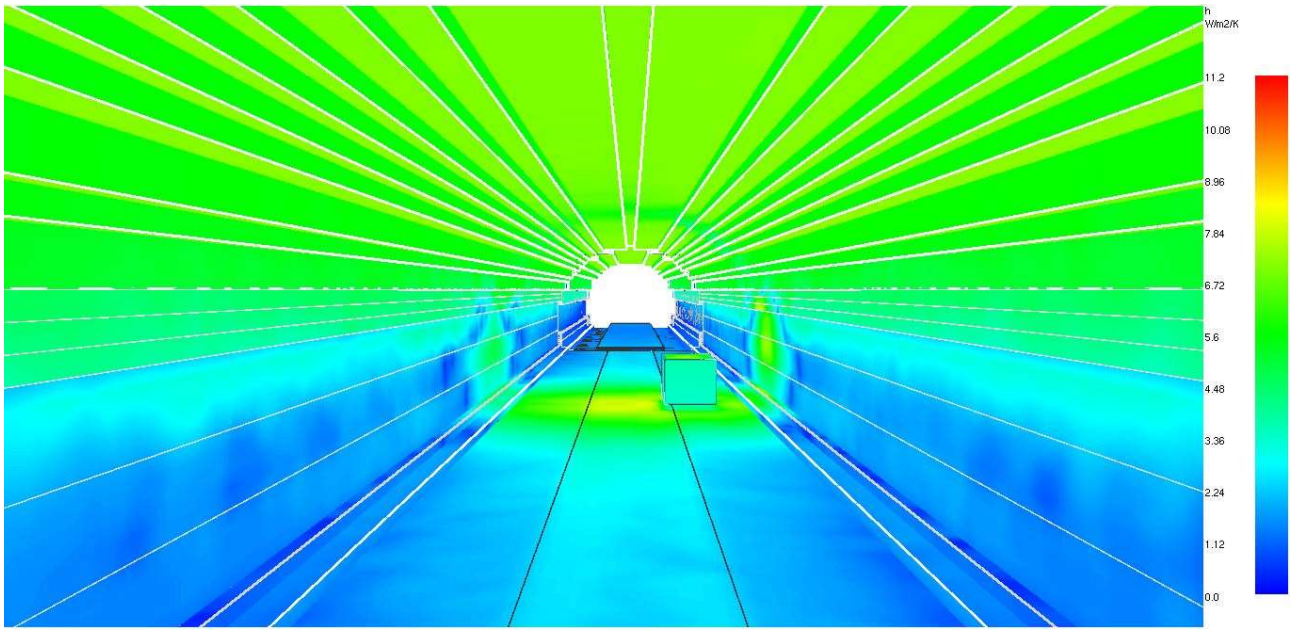

Fig. 4.1.29. Heat transfer coefficient distribution at t = 60 s for HFCV.

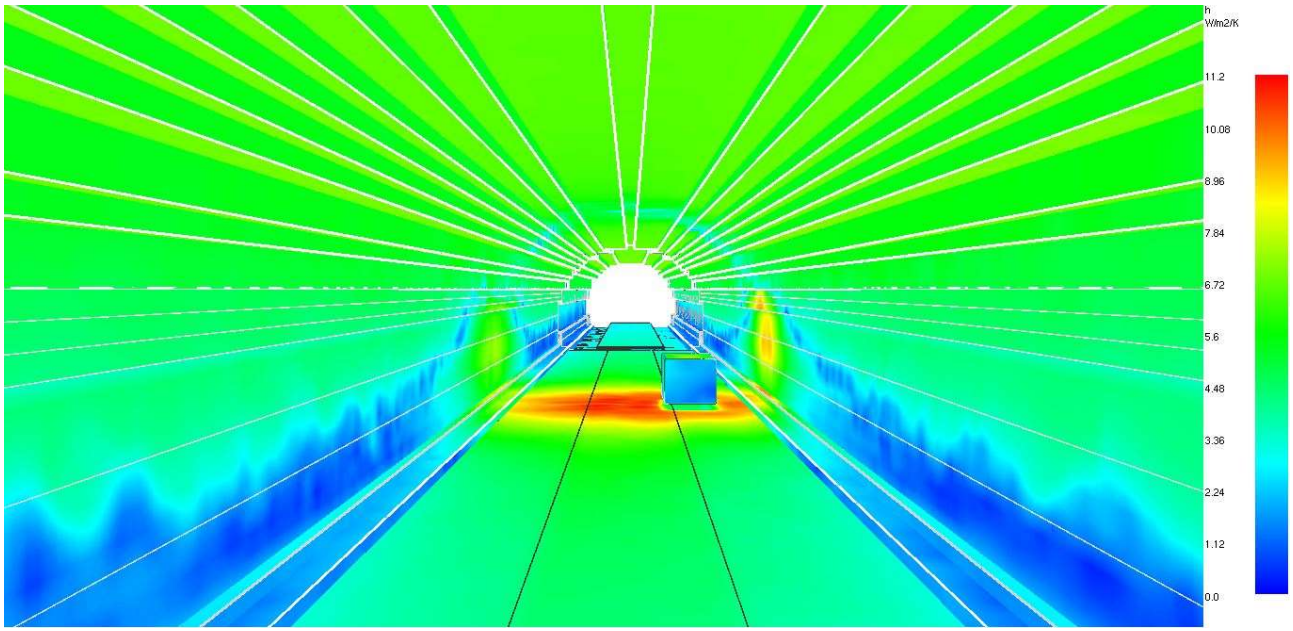

Fig. 4.1.30. Heat transfer coefficient distribution at t = 600 s for HFCV.

As it is possible to appreciate from the previous plots, the heat transfer coefficient, as a consequence of the combustion process, increases starting from the cross sectional thin slice surrounding the fire source. After the first initial instants, once the t-squared time has been exceeded, the heat transfer develops upstream and downstream of the fire location, more on the ceiling and less elsewhere. As the transient goes by, like shown by fig. 4.1.29, the heat exchange becomes greater in correspondence of the entire tunnel vault, of the floor adjacent to the vehicle, and of the portions of the side walls near the fire source, where the heat transfer coefficient sets to nearly $7\ \frac{W}{m^2K}$. Contrariwise, in the remaining walls of the tunnel, where the heat transfer is less developed, the heat transfer coefficient stands at a value slightly lower than $3\ \frac{W}{m^2K}$. Following this kind of evolution, moving towards the last part of the transient, the heat transfer increases also downward along the side walls, but especially at the ground level nearby the hydrogen fuel cell vehicle, where the heat transfer coefficient reaches the value of $11.2\ \frac{W}{m^2K}$, the highest one in the reference time domain of the simulation. According to figures 4.1.29 and 4.1.30, even with fully developed combustion, the road tunnel section in which the heat exchange is the lowest is the one of the side walls, in the verge area as well as in the area corresponding to the lower heights of porcelain steel panels. Having the latter incombustible properties, the results achieved are perfectly consistent.

In figures from 4.1.31 to 4.1.34 the oxygen concentration evolution in the longitudinal section plane of the road tunnel is demonstrated.

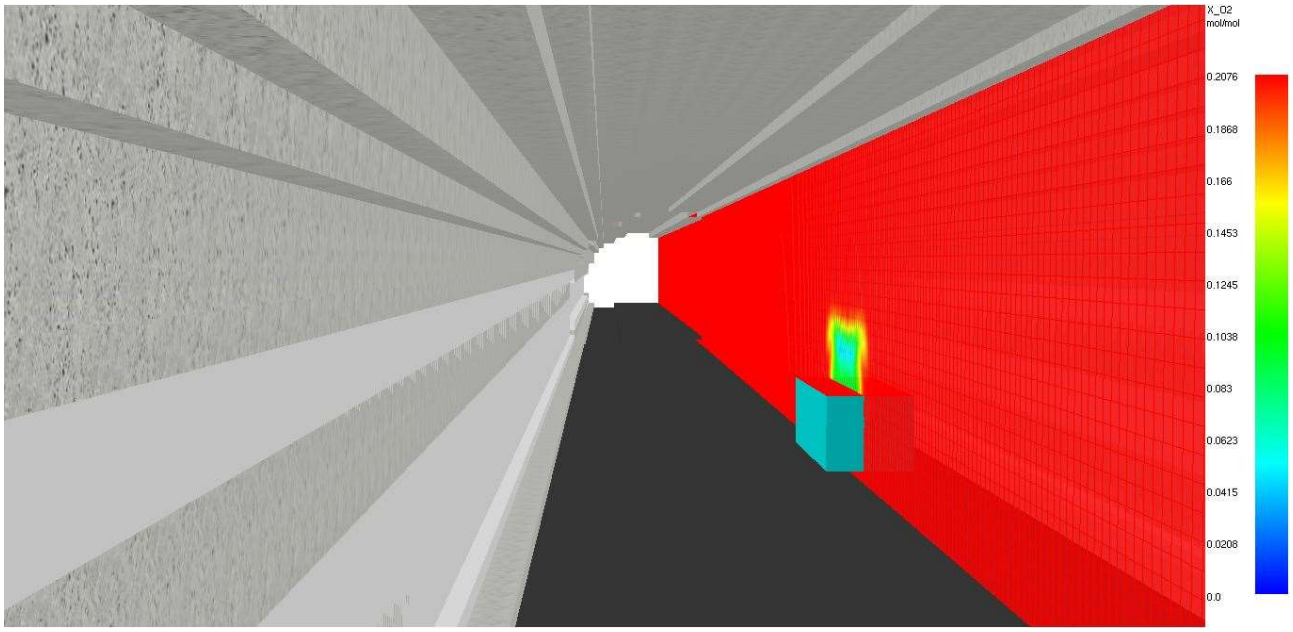

Fig. 4.1.31. 2D oxygen concentration map on plane X = 8.42 m at t = 2.5 s for HFCV.

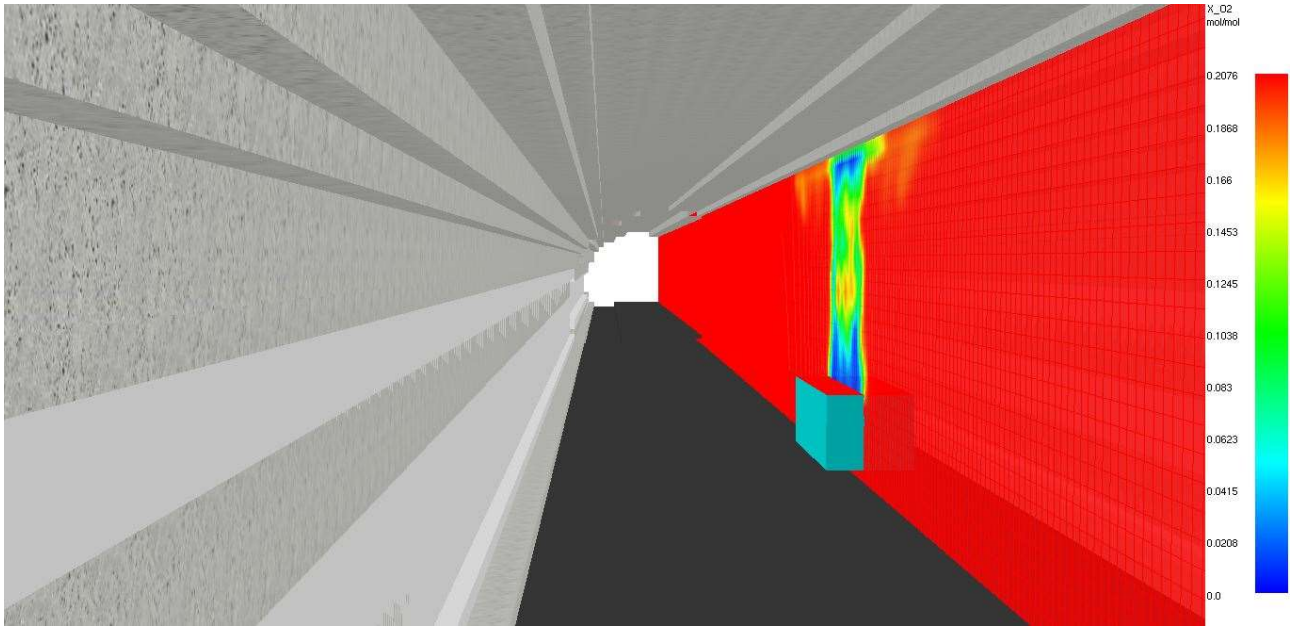

Fig. 4.1.32. 2D oxygen concentration map on plane X = 8.42 m at t = 5 s for HFCV.

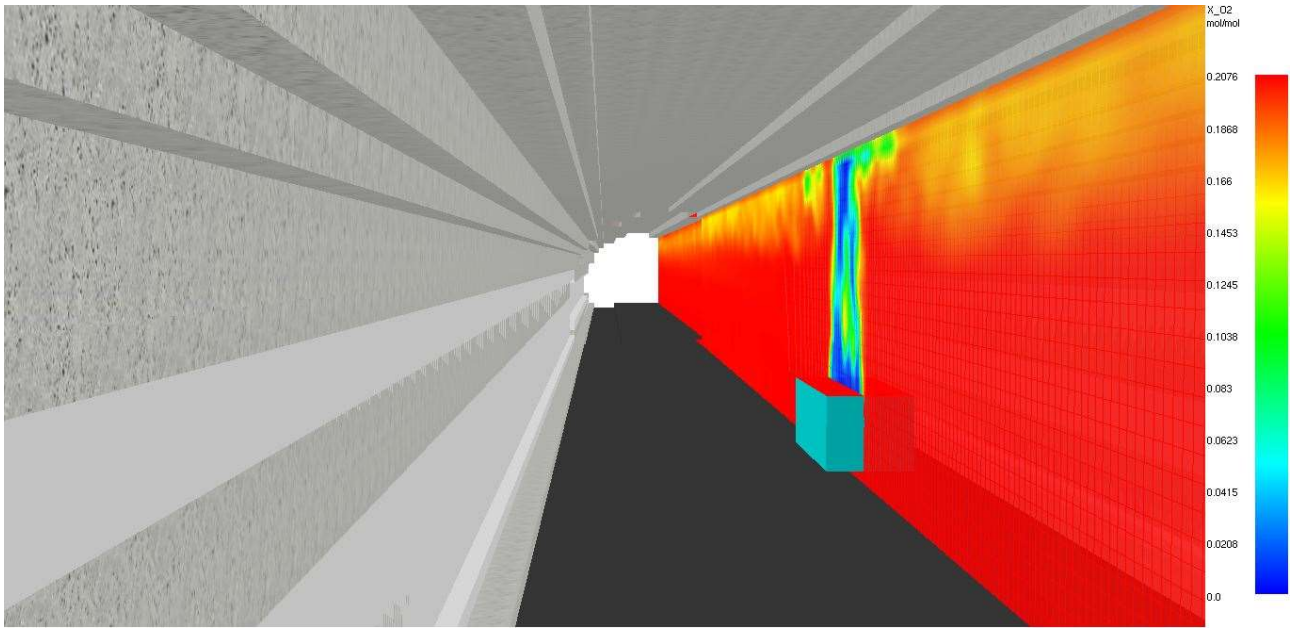

Fig. 4.1.33. 2D oxygen concentration map on plane X = 8.42 m at t = 60 s for HFCV.

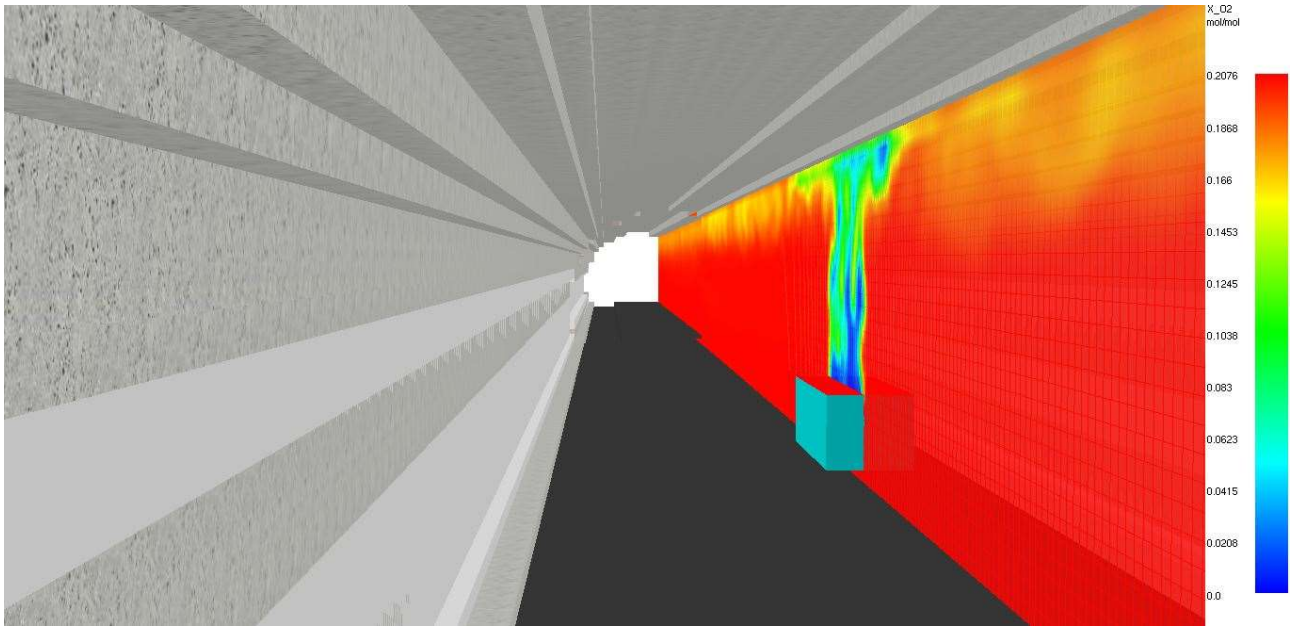

Fig. 4.1.34. 2D oxygen concentration map on plane X = 8.42 m at t = 600 s for HFCV.

Oxygen concentration distributions in the tunnel have a shape very similar to the one of temperatures in the plane X = 8.42 m, with a very fast evolution in the first instants of the transient, beyond which they reach instead an almost steady state condition, barring some fluctuations, for the remaining part of the simulation. Symmetrical conditions in the oxygen distributions, upstream and downstream the HFCV, are also noticed. The lowest concentrations of oxygen, at fully developed flow motion, are observed in correspondence of the tunnel ceiling $\left(0.12\ \frac{mol}{mol}\right)$ at both

left and right sides of the fire location, as well as in the area adjacent to the top surface of the vehicle $\left(0.02\ \frac{mol}{mol}\right)$, in the so called fuel-rich zone. Compared to the oxygen fraction in the ambient air, i.e. with respect to the initial atmospheric conditions set for the problem, the oxygen concentrations close to the tunnel ceiling and to the burning car are, respectively, the 40 % and 90 % less. The oxygen-deficient zones are determined by the combustion reaction of gaseous hydrogen coming out from the nozzle, which, in order to burn, requires the oxygen contained in the air surrounding the fire zone, producing water vapor and heat as by-products. In fact, the hot gases produced by the combustion, which takes place nearby the fire location, symbolize a layer of combustion products in which the oxygen is lacking, and this is also consistent with that shown by the 2D temperature slices, from fig. 4.1.3 to 4.1.6. Except the vertical section from the ground to the ceiling at the longitudinal extent of the car, no oxygen-deficient zones are observed in the road tunnel as the transient goes by, which is positive for the safety of the occupants, to whom, even during the escape, must be guaranteed a sufficient amount of oxygen to avoid permanent health problems.
The last relevant quantity to discuss in this section is the soot visibility, which is strictly related to the hot smokes production in the combustion process.

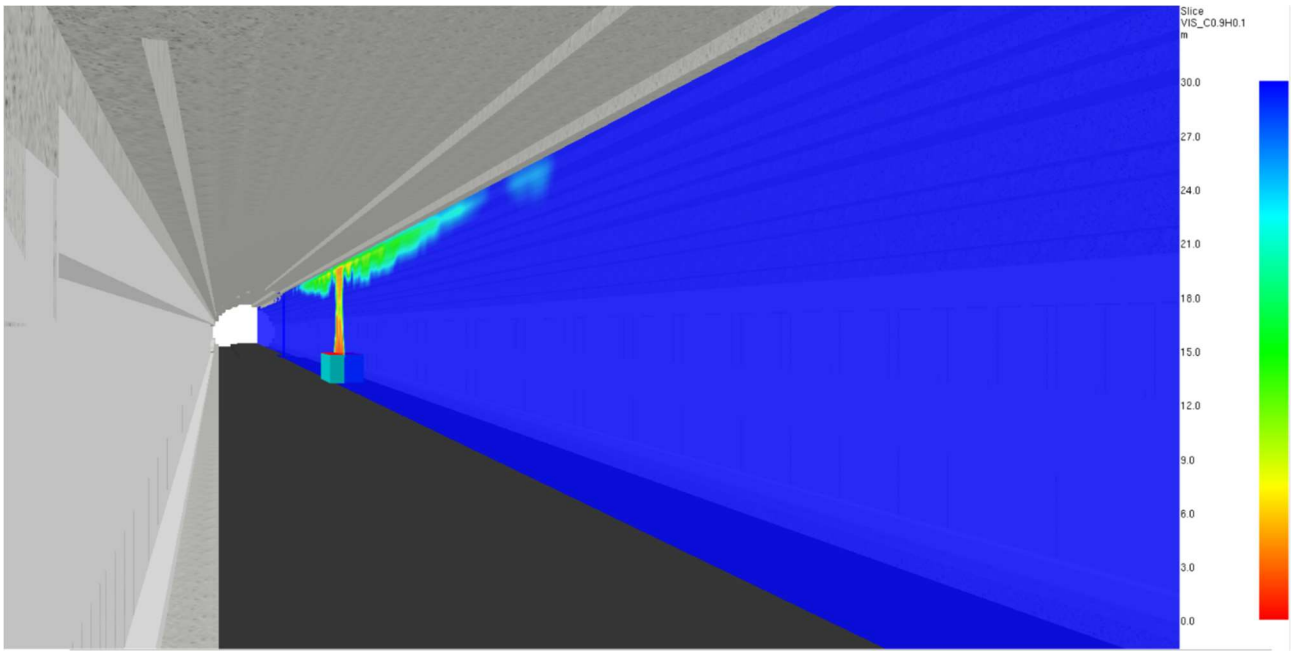

Fig. 4.1.35. 2D visibility map on plane X = 8.42 m at t = 60 s for HFCV.

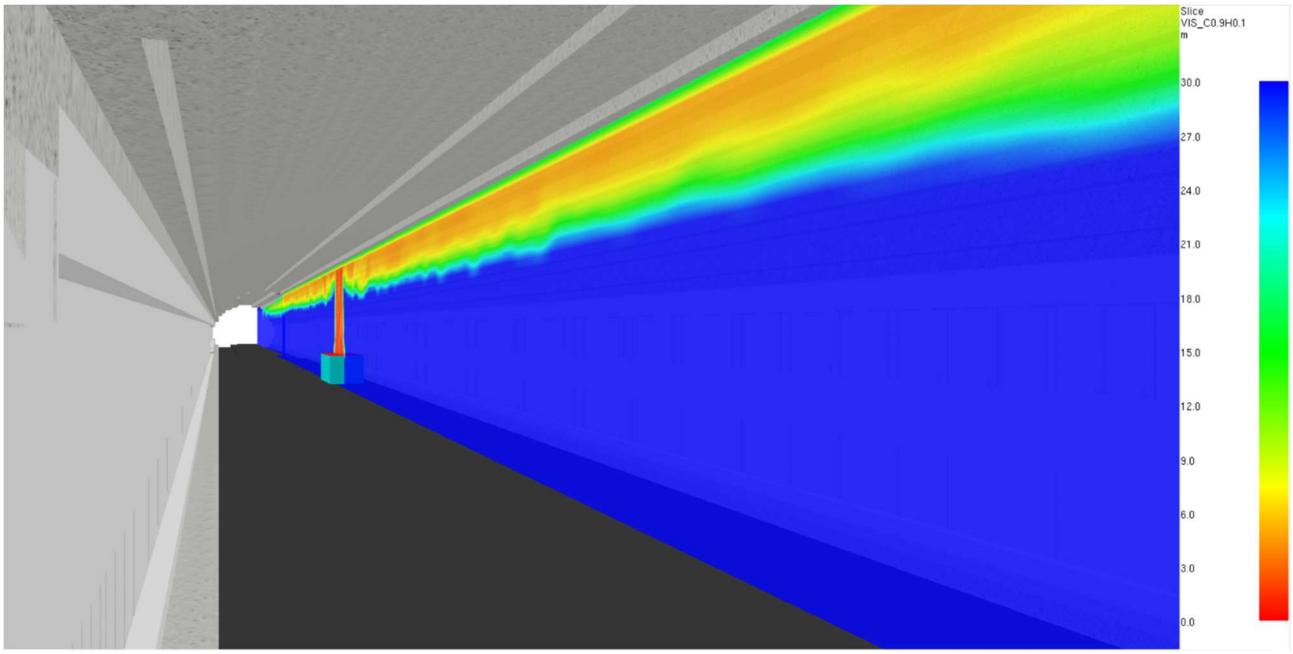

Fig. 4.1.36. 2D visibility map on plane X = 8.42 m at t = 120 s for HFCV.

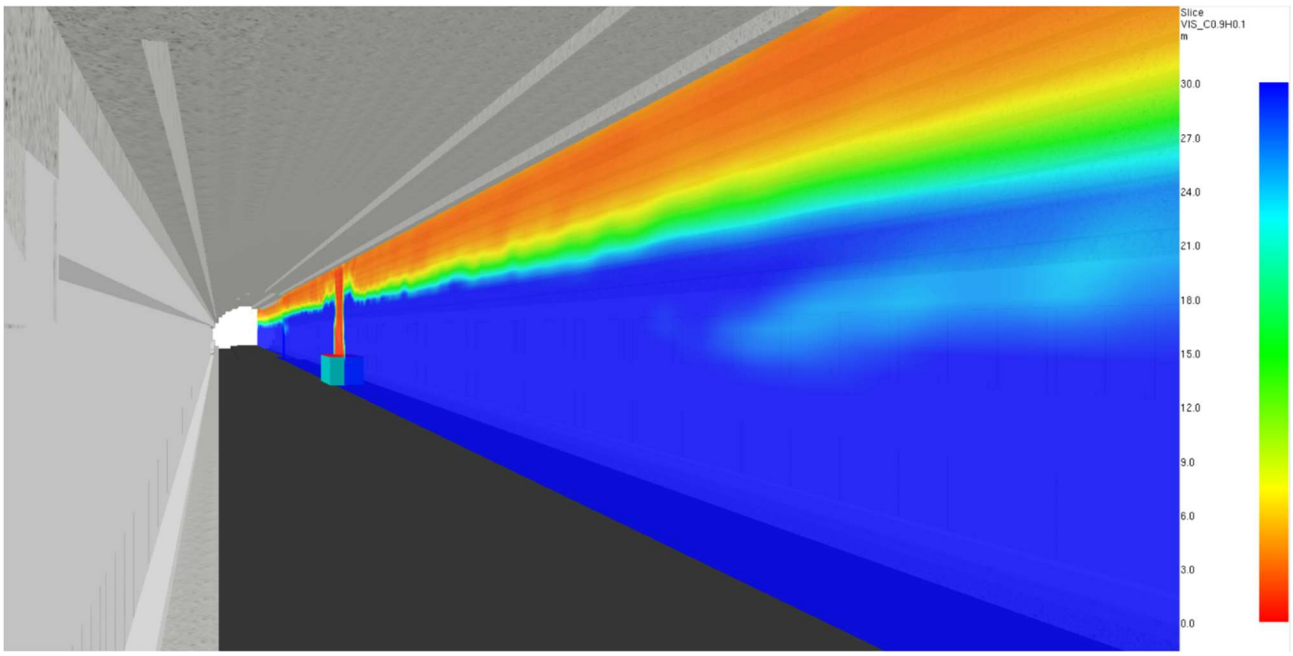

Fig. 4.1.37. 2D visibility map on plane X = 8.42 m at t = 600 s for HFCV.

The soot visibility is computed in the previously reported graphs in terms of visibility distance S, which is calculated by the Fire Dynamic Simulator according to the relation:

$$S = \frac{C}{K_m \cdot \rho \cdot Y_{soot}} \tag{4.1.1}$$

with $C = 3$, and $K_m = 8700\ \frac{m^2}{kg}$ by default, ρ density of the soot, and Y_{soot} (soot yield) the local value of the mass fraction of soot, obtained from the mixture fraction calculation and thus dependent on the manner in which the combustion reaction matters are defined in the simulation setup. Looking at the (4.1.1) it is clear that, in the absence of soot, the parameter S, nothing more than the visibility distance within a homogeneous medium having soot concentration Y_{soot}, should tend to infinity. However, the maximum value it can conventionally assume in FDS is 30 m, for reasons of practicality in the calculations. As the transient goes by, the visibility distance evolves inside the road tunnel by first reducing its value vertically at the car location, and subsequently to the ceiling on both the left and right sides. The downward motion of the hot smokes once reached the tunnel vault after the critical time, together with the high velocity of the smokes flow in that region, affects the soot visibility bringing the visibility distance to a mean value of 9 m at the ceiling, two minutes after the fire ignition. At the end of the considered simulation time, as it is reasonable to be due to the continuation of the combustion process, with a consequent increase in the production of soot, the visibility distance further decreases setting to a mean value of 5 m at the ceiling, stratifying, and decreasing from the bottom to the top. Apart from the area in proximity of the car (zero visibility distance) and of the ceiling, the visibility distance has its maximum possible value, hence 30 m, in all the other sections of the road tunnel.

4.2 Comparison between HFCV and gasoline powered car based simulations

The characterization of the physical quantities of interest for the fire scenario produced by a hydrogen fuel cell vehicle is now proposed again by comparing these same quantities, or rather the main ones, to the scenario produced by the traditional fossil fuels powered car. This is done to make reference in the analysis of fire related safety hazards, both in qualitative and quantitative terms on the basis of the differences in the physical magnitudes involved, between the proven and established technology (gasoline car) and the innovative one (HFCV), whose risks in the event of an accident are not yet fully understood.
The first thing to discuss is the heat release rate, highlighted in fig. 4.2.1.

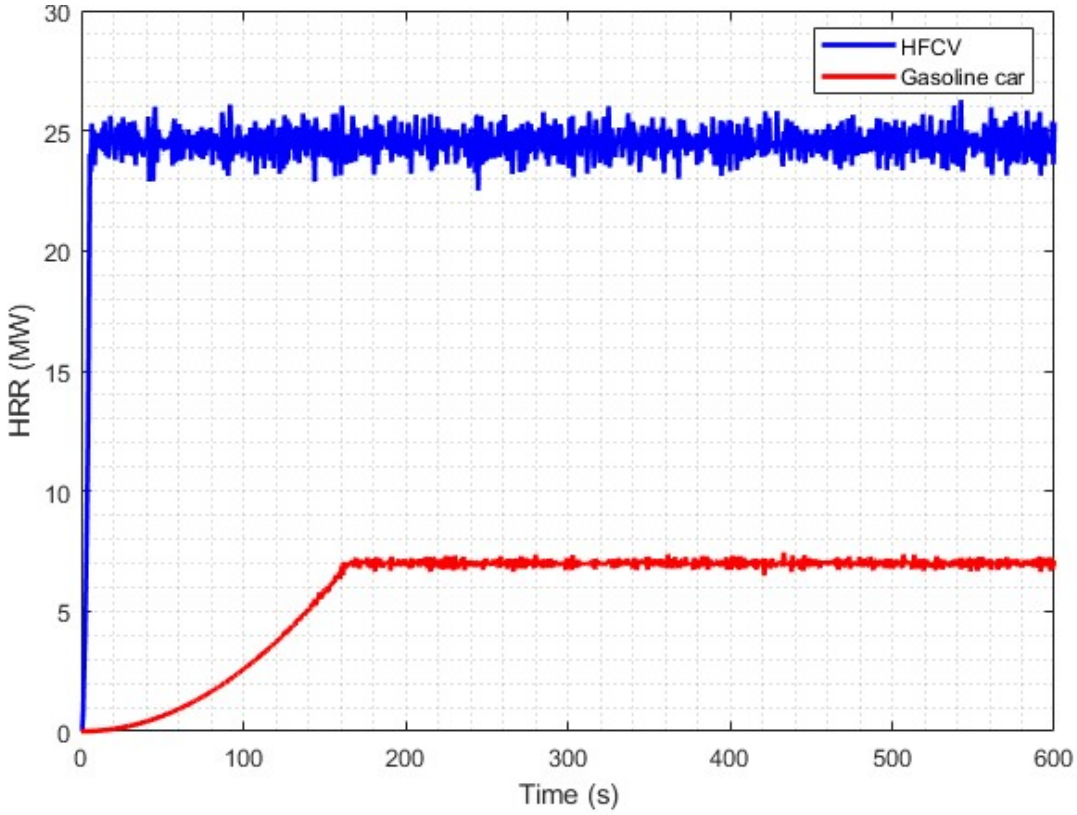

Fig. 4.2.1. HRR evolution compared between HFCV and gasoline car.

The heat release rate of gasoline care fire is 7 MW, thus 3.5 times lower than that of the hydrogen fuel cell vehicle one. Apart from the lower peak value reached by the HRR in the case of traditional fossil fuels powered car, what is also quite interesting is the growth time necessary to reach this peak. The t-squared time t^2, in fact, is more than 30 times greater in the case of the gasoline powered car based simulation (red curve in fig. 4.2.1) with respect to the HFCV based one (blue curve in fig. 4.2.1). This translates into a temporal delay as regards the achievement of the almost steady state power condition in the case of gasoline car, whose stationary behaviour however, regardless of the growth time, is common to both scenarios. The higher heat release rate in the case of HFCV, as already discussed, is due not only to the higher heat of combustion that characterize

the hydrogen burning reaction with respect to that of octane, but also to the physical characteristics of the hydrogen itself. Rather than the pool fire typical of traditional fossil fuels powered cars fire scenarios, in fact, hydrogen burning results in a high speed jet fire which produces a concentrated heat release from the nozzle.
The magnitude difference between the two HRRs, obviously, also greatly influences the ceiling temperatures in the road tunnel, reported in fig. 4.2.2.

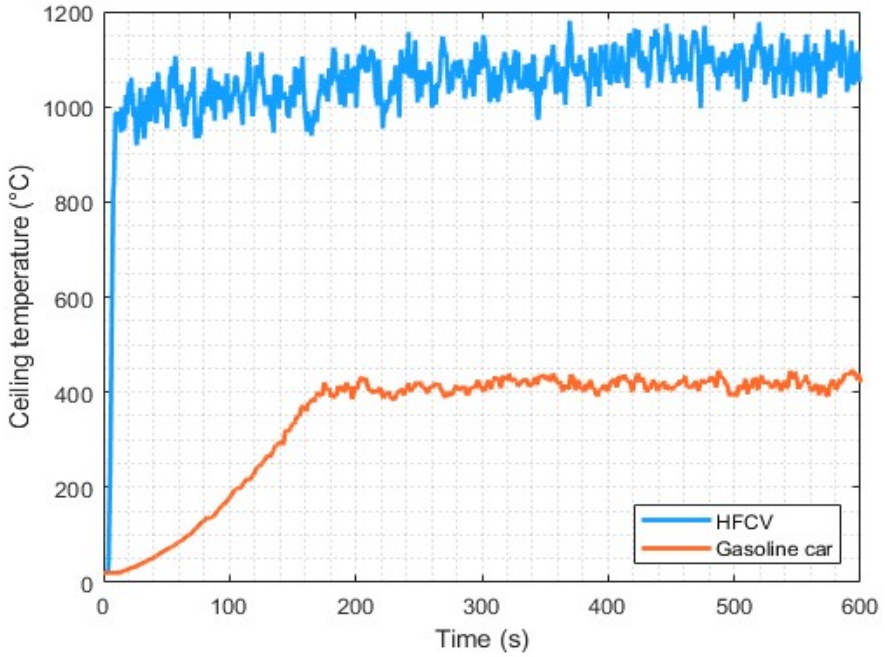

Fig. 4.2.2. Ceiling temperature evolution of the gas phase at fire source compared between HFCV and gasoline car.

The ceiling temperature evolution for both the simulations carried out at fire location, thus at 125 m from the tunnel entrance, is characterized by the same trend of the HRR depicted in fig. 4.2.1. As a consequence of the lower heat release rate, the maximum ceiling temperature reached during the transient in the case of gasoline powered car is slightly lower than 450 °C, hence less than half with respect to the HFCV case. The ceiling temperature for the traditional fossil fuels powered car based simulation rises more slowly before reaching the quasi steady state condition, during which it settles to an average value of about 400 °C, compared to the other simulation. Another difference between the two ceiling temperature evolutions is noticeable, looking at the pale blue and orange curves in fig. 4.2.2, in terms of fluctuations during the transient after the critical time: in greater number and more pronounced for the hydrogen fuel cell vehicle case, while minor and less marked in the other one.

Moving to the 2D temperature slices in the road tunnel, in figures from 4.2.3 to 4.2.6 it is reported their distribution one minute after the fire ignition and at the end of the transient, both in the longitudinal (figures 4.2.3, and 4.2.4) and cross plane sections (figures 4.2.5, and 4.2.6). Due to the slower nature of the transient in the case of gasoline car, due to the longer ramp-up time, the instants of time lower than the critical time are not examined in the 2D slices, as they lack useful information for the problem under investigation.

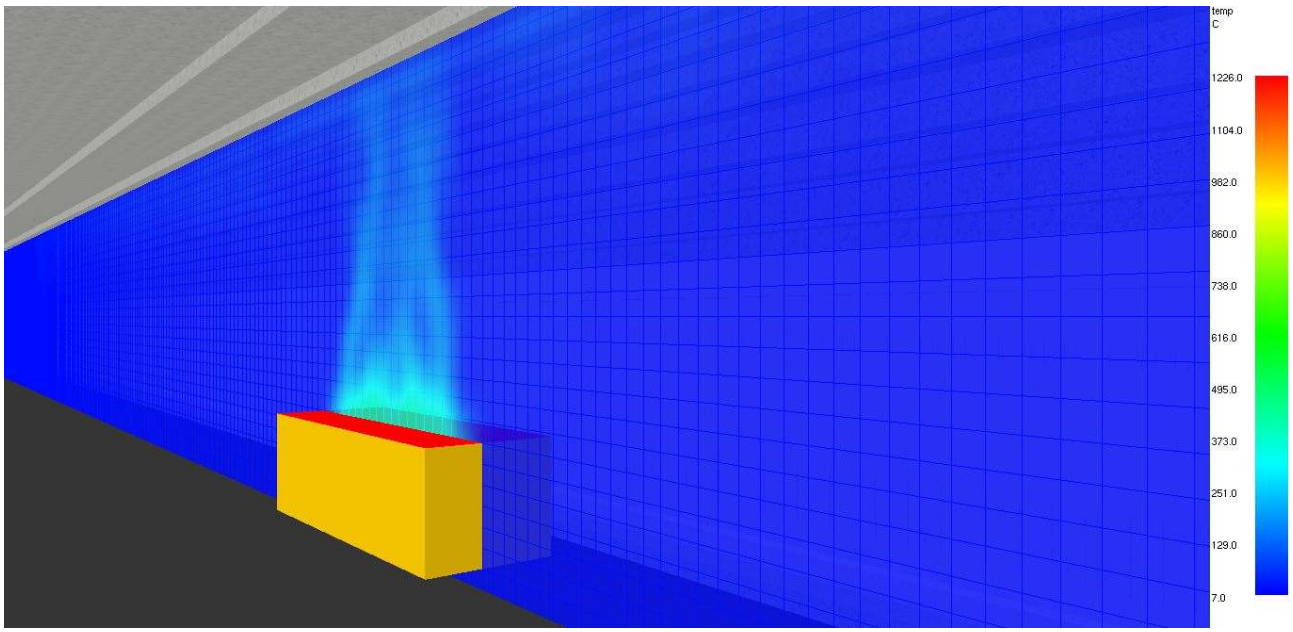

Fig. 4.2.3. 2D temperature map on plane X = 8.42 m at t = 60 s for gasoline car.

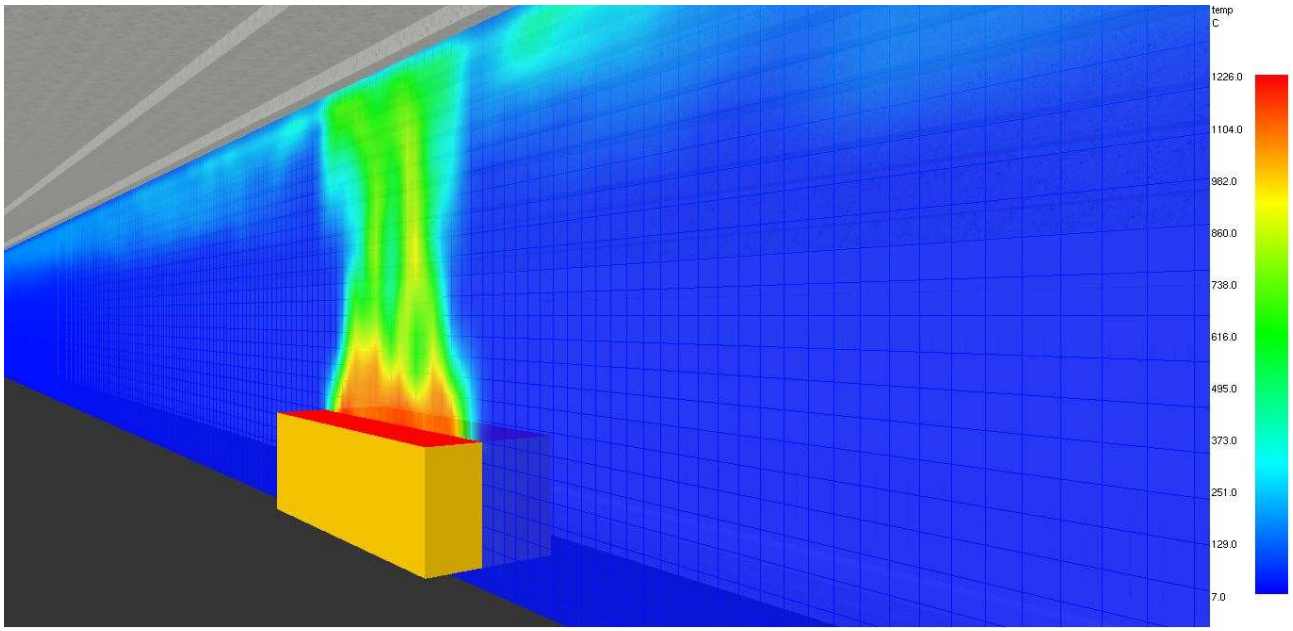

Fig. 4.2.4. 2D temperature map on plane X = 8.42 m at t = 600 s for gasoline car.

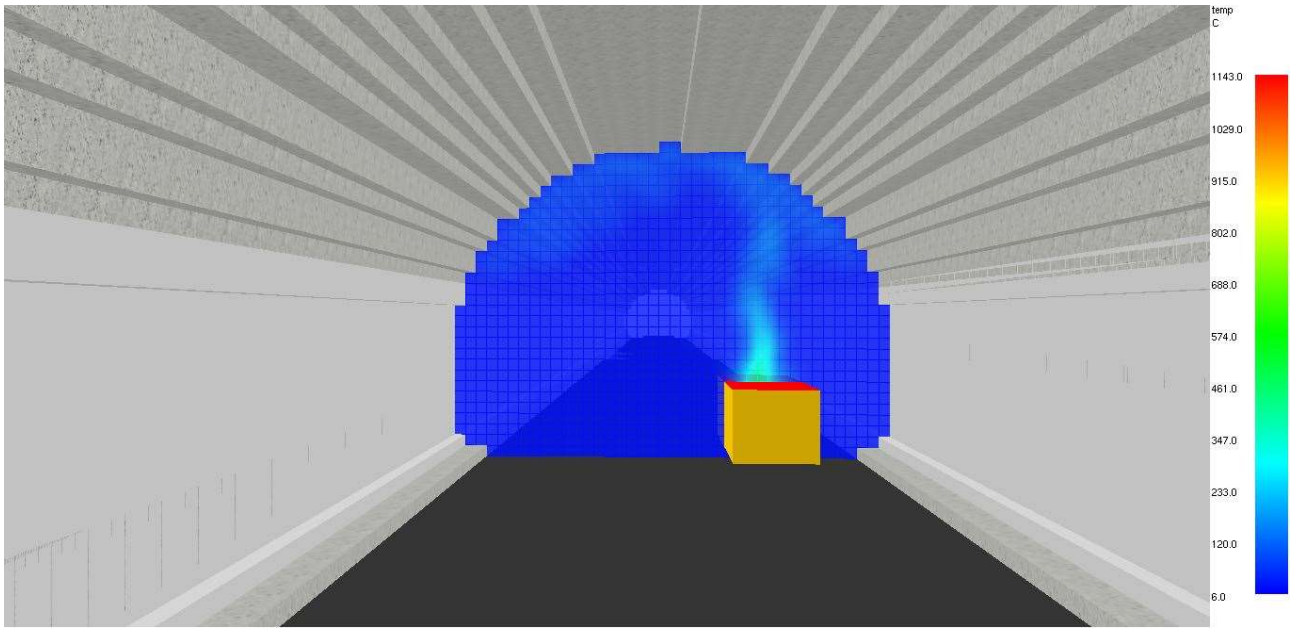

Fig. 4.2.5. 2D temperature map on plane Y = 125 m at t = 60 s for gasoline car.

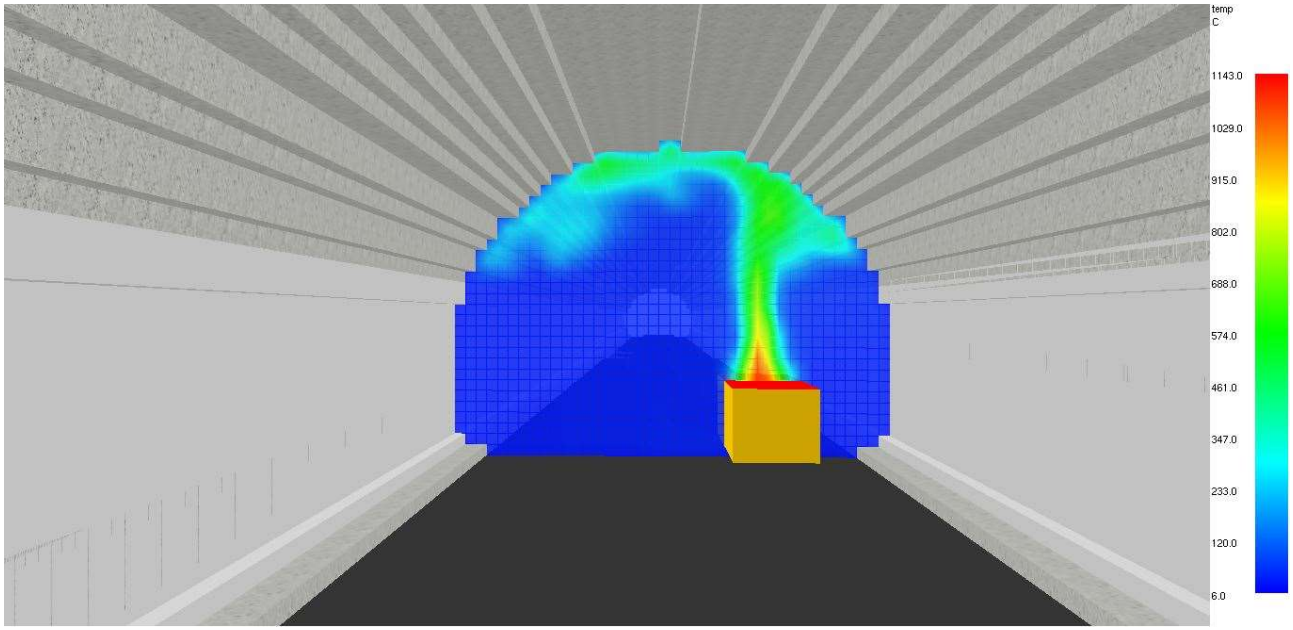

Fig. 4.2.6. 2D temperature map on plane Y = 125 m at t = 600 s for gasoline car.

As denoted by the previous figures, the characteristics of the gasoline car fire are the ones of the classic pool fire. As a consequence of the combustion of the solid materials that make up the vehicle and of the fuel, hot smokes are generated during the burning process. These last move in the direction of the road tunnel ceiling, as a result of the buoyancy induced by density difference. During the combustion, the presence of air all around the fire source, coupled with thermal convection and radiative phenomena, is responsible of the reduction of the fire plume temperature, whose maximum value is therefore located exactly on the top surface of the burning car. This behaviour is

considerably different with respect to the one assumed by the fire plume temperature peak in the case of hydrogen fuel cell vehicle, in which instead it settles down in the reaction zone and not close to the object, as seen in the previous subchapter. Once reached the tunnel vault, the vertical development of hot smokes is impeded, hence their flow reverses and they spread horizontally to the left and to the right of the road tunnel, doing that the temperature contour at extinguished transient on the plane Y = 125 m at fire location (fig. 4.2.6) assumes a sort of M-shape. The maximum temperature reached during the burning process in the case of traditional fossil fuels powered car is computed in 1226 °C and 1143 °C, respectively for the longitudinal and cross section plane of the tunnel. These temperature peak values are not only lower with respect to the HFCV ones (32 % and 37%, respectively), but also spatially narrower.

As previously done for the hydrogen fuel cell vehicle fire scenario, the monodimensional temperature distribution in the tunnel length at different instants of time as well as the temperature evolution at the wall surface of the ceiling are now discussed even for the gasoline car based case.

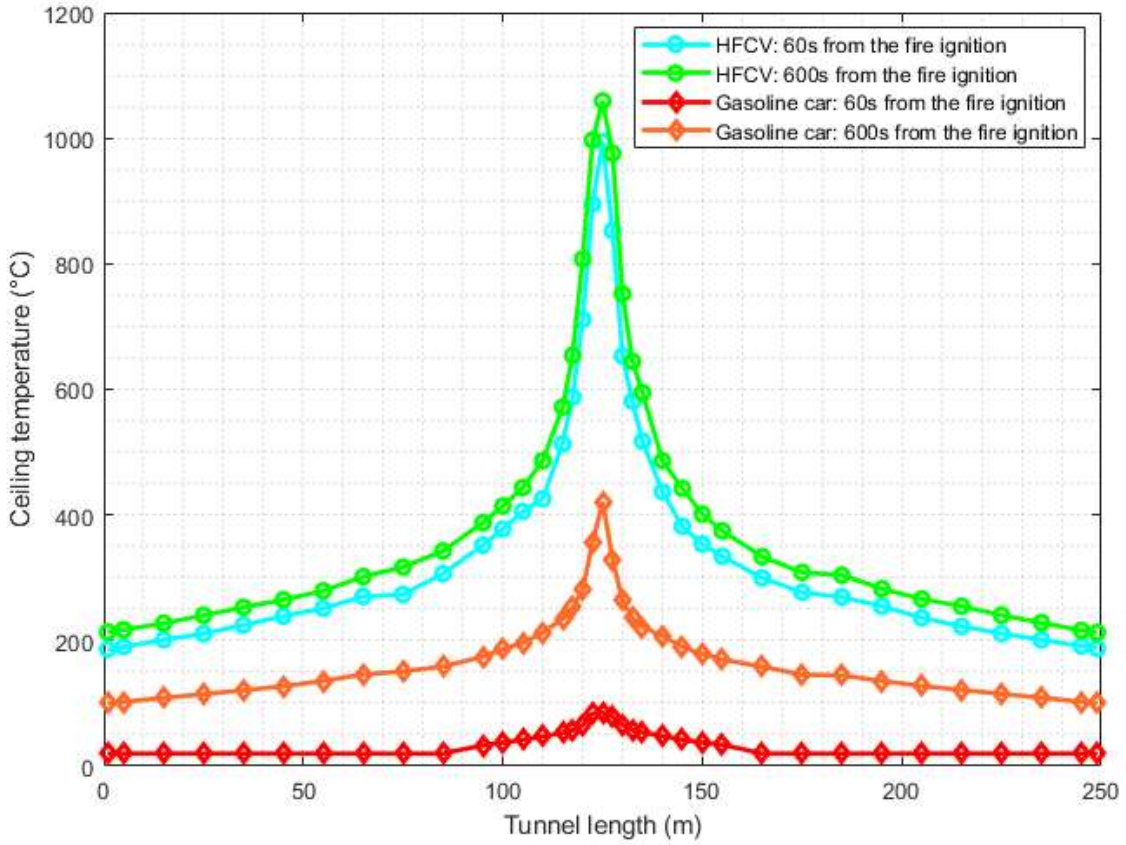

Fig. 4.2.7. Ceiling temperature distribution of the gas phase in the tunnel length compared between HFCV and gasoline car.

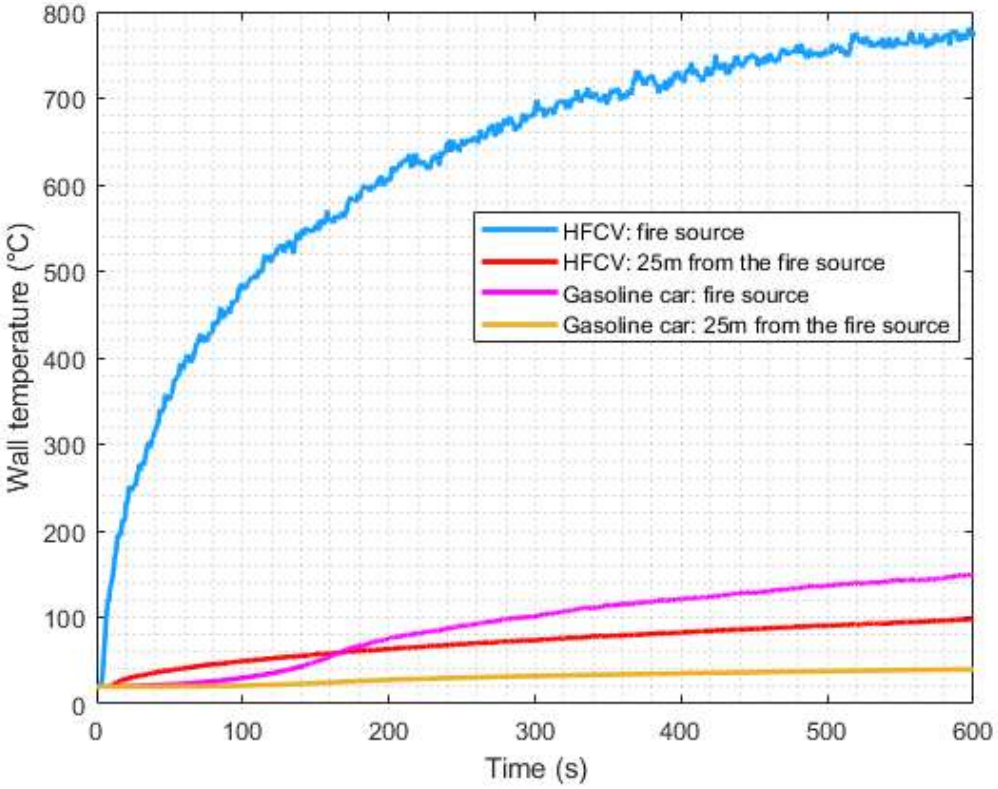

Fig.4.2.8. Wall ceiling temperature evolution compared between HFCV and gasoline car.

The ceiling temperature distribution in the road tunnel length for the gasoline car fire scenario is characterized by a symmetrical shape upstream and downstream of the fire source, as in the case of HFCV, due to the fact that geometry and boundary conditions of the problem are kept unchanged. Apart from the lower ceiling temperature peak values reached at fire location during the transient, 425 °C and 100 °C respectively at 60 s and 600 s from the fire ignition, the traditional fossil fuels powered car fire stands for lower steepness both in the growth and decrease phases. This translates into a lower temperature difference, especially in the road tunnel stretch close to the burning car (100 m – 150 m), between two neighbouring thermocouples with respect to HFCV accident scenario. The higher ramp-up time required to reach the almost steady state power deposition is also responsible for the more gradual evolution of the ceiling temperature in the transient, as highlighted by the distance among the orange and red curve in fig. 4.2.7, compared to the instead rapid achievement of the peak temperature in the case of HFCV fire scenario. In the latter case, in fact, the monodimensional ceiling temperature distribution immediately after the critical time is almost superimposable with which at the end of the transient, like shown by green and pale blue curves in fig. 4.2.7. Also the wall temperature at the ceiling for the gasoline car fire, as expected due to the lower heat release rate, is considerably lower with respect to the hydrogen fire. In particular, the lower the distance from the fire source the greater the temperature difference between the two cases carried out, with a wall temperature at the end of the transient computed in 150 °C and 40 °C, respectively at fire location and 25 m from it, in the case of traditional fossil fuels powered car fire. Due to the fact that high ceiling temperatures cause possible damages to the road tunnel lining, this aspect must be carefully taken into account when comparing fire related safety hazards between the established technology and the new one represented by hydrogen fuel cell vehicles.

Moving forward in the analysis of the differences between the HFCV fire and gasoline car fire, the hot smokes evolution is highlighted in the figures below.

Fig. 4.2.9. Hot smokes distribution at t = 60 s for gasoline car.

Fig. 4.2.10. Hot smokes distribution at t = 120 s for gasoline car.

Fig. 4.2.11. Hot smokes distribution at t = 600 s for gasoline car.

The hot smokes produced during the burning process, for the same amount of time from the fire ignition, are noticeably greater in the case of traditional fossil fuels powered car scenario. At the same point of the transient, in fact, with respect to the HFCV fire scenario, they go deeper into the tunnel length both upstream and downstream from the car location into the tunnel length, moving downwards more substantially once reached the tunnel ceiling. The larger amount of hot smokes is a consequence of the fuel characteristics used to power the car. Black smokes, in fact, are produced from carbon particles or organic compounds that have not been completely burned during combustion. When the hot flue components condense on cooler objects, such as the walls of the road tunnel, the result, if they are primarily carbon made, is the production of soot. In the case of hydrogen fuel cell vehicle fire scenario the only burning materials that contain carbon are the ones of which the vehicle is made, while for gasoline powered car simulation a large amount of carbon is contained not only in the materials of the car itself, but mainly in the fuel, just gasoline. For this reason a larger amount of hot smokes is produced in the traditional fossil fuels powered car fire scenario, rather than in the hydrogen powered one.

The velocity of the smokes flow for the gasoline powered car fire scenario, in the form of 2D vector slices in the longitudinal plane section, is analysed in the figures 4.2.12 and 4.2.13.

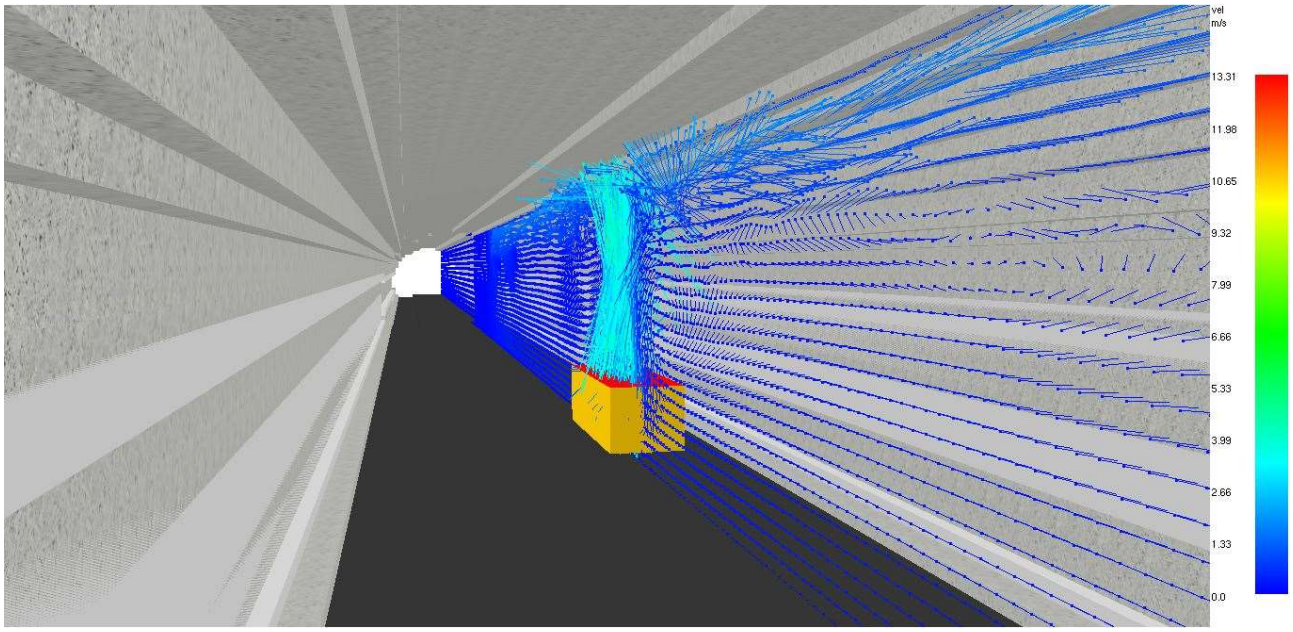

Fig. 4.2.12. 2D vector velocity map on plane X = 8.42 m at t = 60 s for gasoline car.

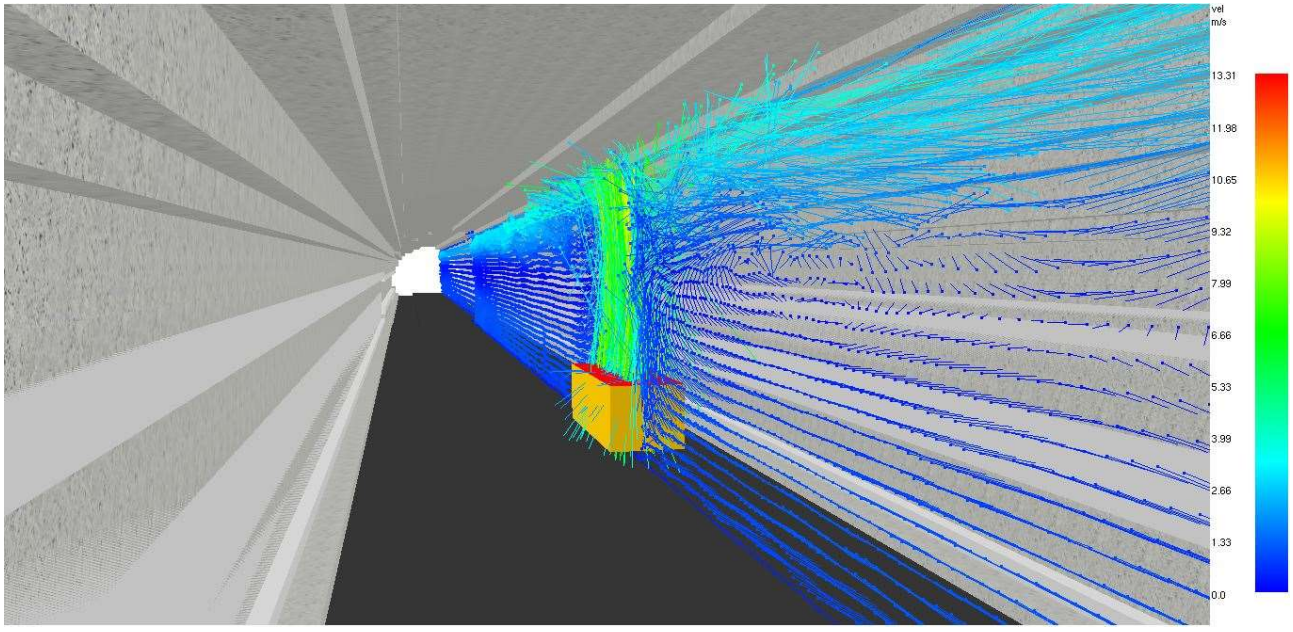

Fig. 4.2.13. 2D vector velocity map on plane X = 8.42 m at t = 600 s for gasoline car.

As in the case of HFCV fire scenario, the smokes flow velocity close to the fire summit increases in the transient time due to the symmetrical ascending heat source force on both the left and right side of the road tunnel, reaching the peak value in correspondence of the ceiling, obviously at car location. The lack of the high speed hydrogen jet, however, reduces considerably the flow velocity values inside the road tunnel section, which settle, at fully developed motion, to a mean value of $7\ \frac{m}{s}$ close to the top surface of the vehicle and to the ceiling, with a peak of $13.3\ \frac{m}{s}$. The aforementioned values, respectively 36 % and 38% lower all thing being equal compared to the scenario produced by the hydrogen powered car, prove the lower dynamics of the gasoline car fire, with lower inertial forces as well as lower thermal buoyancy. This also translates into less turbulence and, therefore, less vortex formation inside the road tunnel length.
The last thing to discuss at this point is the soot visibility, inevitably related to hot smokes production discussed above.

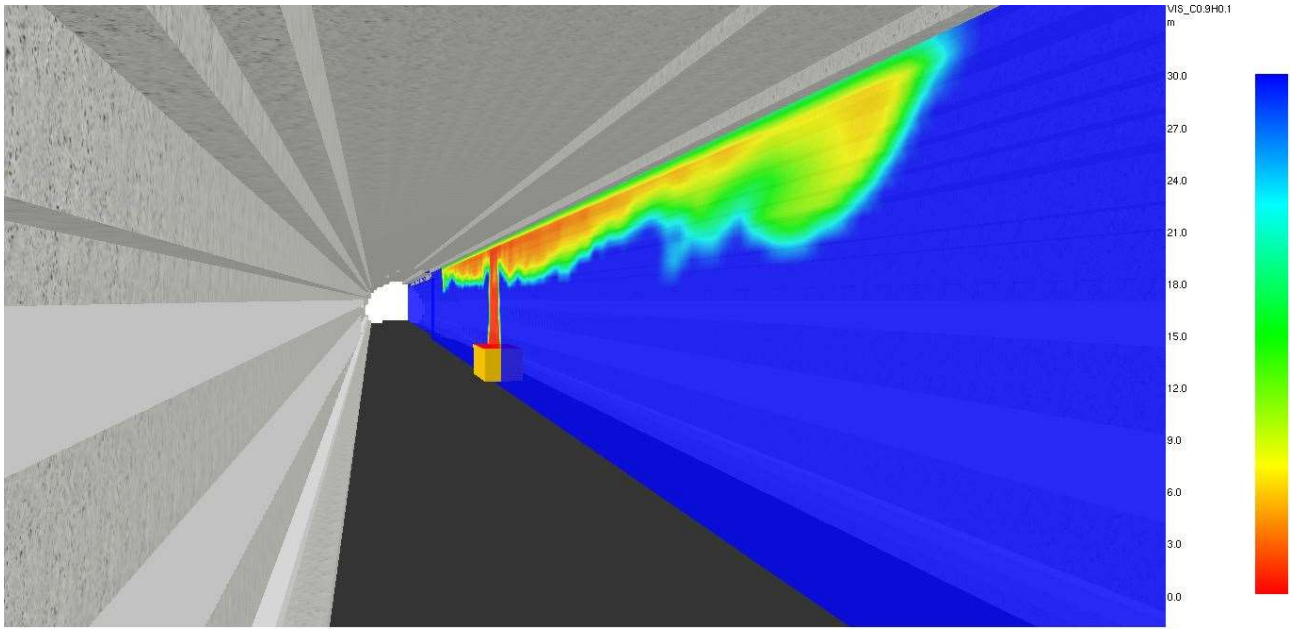

Fig. 4.2.14. 2D visibility map on plane X = 8.42 m at t = 60 s for gasoline car.

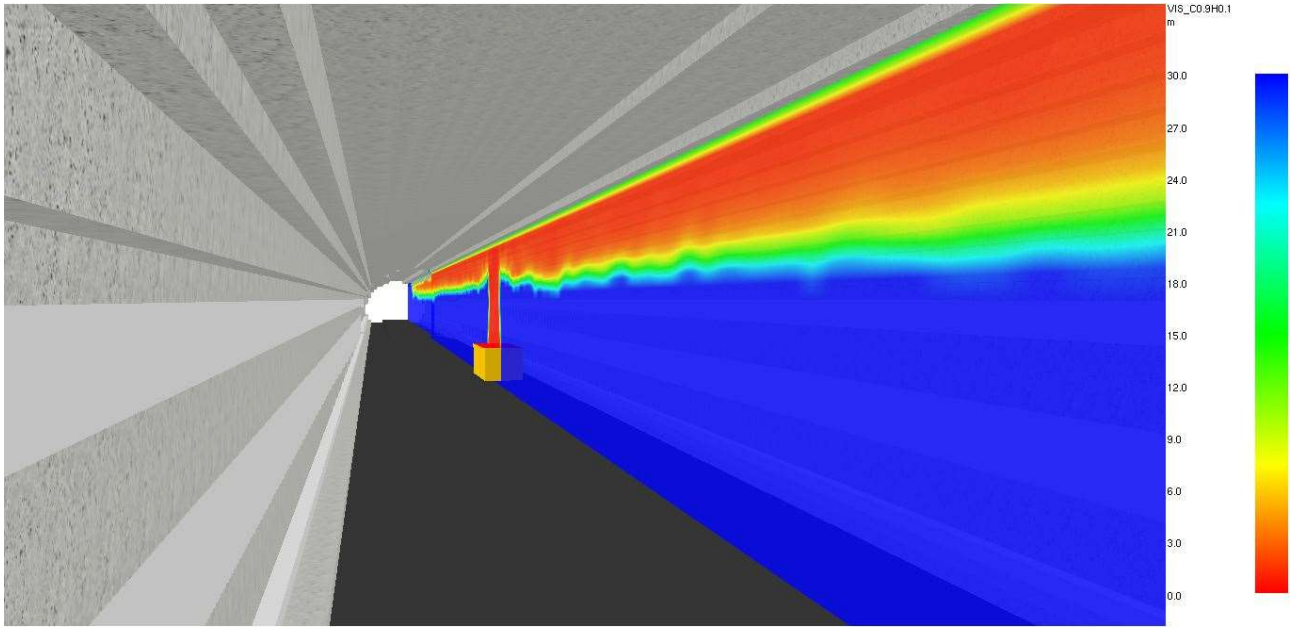

Fig. 4.2.15. 2D visibility map on plane X = 8.42 m at t = 120 s for gasoline car.

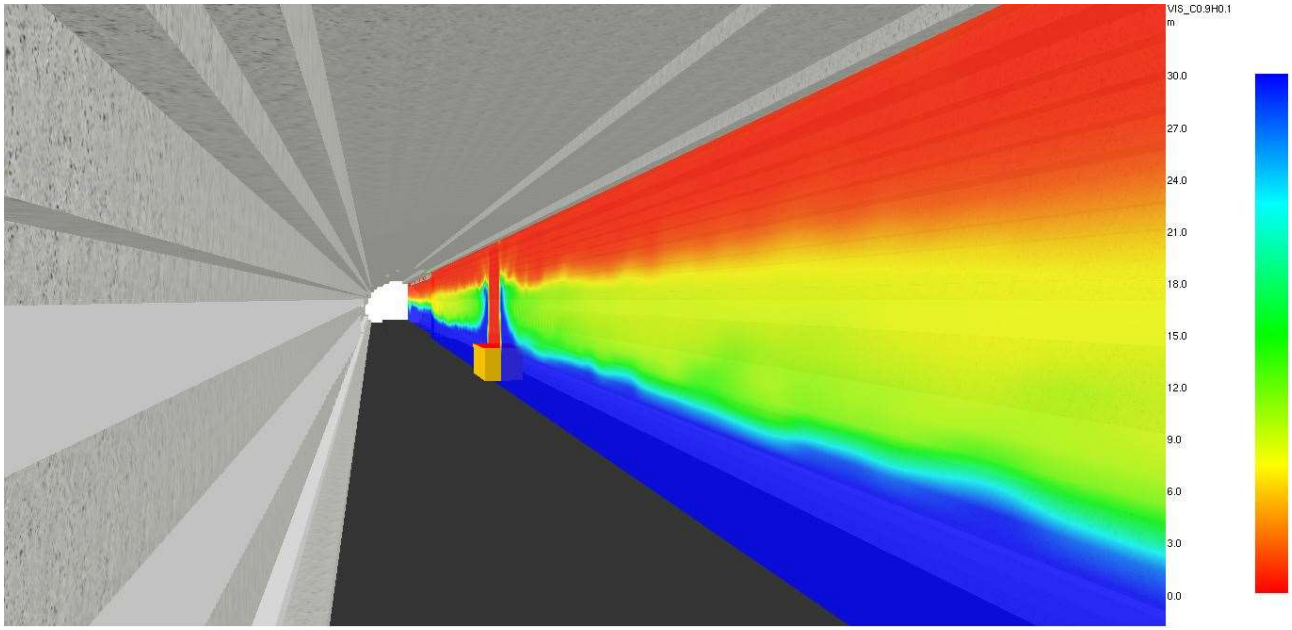

Fig. 4.2.16. 2D visibility map on plane X = 8.42 m at t = 600 s for gasoline car.

The soot visibility evolution has a trend similar to the one in the case of HFCV fire scenario, with a progressive reduction going down from the ceiling to the bottom part of the tunnel as the transient goes by. However, in the comparison, it is noticeable a considerably difference in terms of visibility distance values, which settle to about 0 m at the ceiling and between 6 m and 9 m at middle heights of the tunnel, hence substantially lower with resepect to the hydrogen fire. Due to the larger amount of hot smokes produced during combustion, the poor visibility areas do not establish only

in the upper parts of the tunnel, but also in the medium-lower ones, which instead do not happen in the HFCV based simulation, leaving acceptable visibility distance values only at the ground level and up to maximum 1.5 m from it.

4.3 Implementation of ventilation strategies for HFCV based simulation

The outcome of the previous subchapter is that due to the higher ceiling temperature, as a consequence of the greater heat release rate in the case of road tunnel accident, the fire hazard of hydrogen jet fires is more dangerous with respect to the fire scenario produced by a traditional fossil fuels powered car (pool fire). This occurrence must be thus carefully taken into account in the design of the tunnel ventilation system, an important support in the suppression of the thermal behaviour of the road tunnel. Among the different ventilation strategies available (natural, transversal, longitudinal, hybrid) the longitudinal one is largely used as it is practical, inexpensive, and suitable for two-lane tunnels with a unique direction of travel, like in the case of Virgolo. Apart from ventilation during ordinary operation, used to ensure good air quality by expelling pollutants, additional emergency one is indispensable in the case of road tunnel accidents resulting in fires ignition, in order to reduce the consequences of heat and smoke generated, to facilitate the tunnel abandonment, and to back up in general safety operations. Longitudinal ventilation, performed in the tunnel length using jet fans, carries cold and fresh air into the fire region, reducing the temperature due to species dilution by mixing, and pushing forwards hot smokes in the direction of the tunnel outer section. One of the key parameters in ventilation strategies is the critical ventilation velocity, defined as the minimum speed thanks to which the backlayering length is null and the hot smokes are spread out only downstream of the car location, making available a path for the rescue of the tunnel occupants [31]. The critical ventilation velocity is an essential physical quantity for what concerns fire interdiction and mitigation, and for this reason it has been experimentally detected by numerous researchers which, also using theoretical data, investigated to build up several models useful to foretell its value. The critical velocity model by Kennedy is the most widespread in road tunnel smoke control design, being recommended by several road tunnel ventilation guides [39]. It expresses the critical ventilation velocity v_{cr} as follows:

$$v_{cr} = k_1 k_g \left(\frac{g\, Q\, H}{\rho\, c_p\, A\, T_f} \right)^{\frac{1}{3}} \tag{4.3.1}$$

$$T_f = \left(\frac{Q}{\rho\, c_p\, A\, v_{cr}} \right) + T \tag{4.3.2}$$

with $k_1 = 0.606$, $g = 9.81\ \frac{m}{s^2}$, ρ average density of the incoming air, c_p specific heat of air, T temperature of incoming air, A tunnel cross section perpendicular to the flow, H tunnel height, T_f

average temperature of hot smokes, Q heat release rate of the produced fire, and k_g grade factor, which takes into account the effect of blowing smokes downhill, and can be obtained according to:

$$k_g = 1 + 0.374\ \theta^{0.8} \tag{4.3.3}$$

where θ is the tunnel average slope. In the specific case under investigation, with Virgolo road tunnel cross section, height, and average slope of, respectively, $62.32\ m^2, 7.16m$, and 0.2 %, also considering the hydrogen fire heat release rate assessed in $24.5\ MW$, the critical velocity value, obtained solving iteratively the system of two equations (4.3.1, 4.3.2) for two unknowns (v_{cr}, T_f), is computed in $2.49\ \frac{m}{s}$.

The longitudinal ventilation is achieved in the Virgolo road tunnel taking advantage of jet fans, with in particular 5 ventilation sections per barrel and 2 bi-directional axial Jet-Foil 71 K fans by section [20].

Fig. 4.3.1. Jet-Foil 71 K adopted in Virgolo road tunnel.

The jet fans Jet-Foil 71 K installed in the Virgolo road tunnel are automatically adjustable according to the polluting load detected, and manually in function of emergencies, with the possibility of reversing the air flow in particular cases or in emergency situations. The typical air volumetric flow rate they work at during normal operation is $15\ \frac{m^3}{s}$, with a required start-up time to reach the nominal power output, starting from system off, of 30 s. It is worth remembering that in the present work only a 250 m long stretch of Virgolo is considered for the analysis of the fire scenario thus, rescaling with respect to the total length, a unique ventilation section is adopted, the latter located in correspondence of the tunnel entrance and composed by 2 Jet-Foil 71 K, each of which positioned at the ceiling in the middle of the respective lane.

An extract of the reference jet fans characteristics, taken from their technical datasheet, is available below [40].

QUANTITY OF INTEREST	
Speed (rev/min)	2950
Thrust (N)	735
Volume flow $\left(\frac{m^3}{s}\right)$	15.2
Outlet velocity $\left(\frac{m}{s}\right)$	38.4
Absorbed power (kW)	26.4

Tab. 4.3.1. Technical datasheet extract of Jet-Foil 71 K.

The model proposed by Kennedy to compute the critical ventilation velocity, previously discussed in detail, is obtained by performing real cases experiments on traditional fossil fuels powered car fires. This therefore does not guarantee that the critical velocity value computed with this approach, 2.49 $\frac{m}{s}$, is also meaningful for hydrogen jet fires. Moreover, in the combined use of the Fire Dynamic Simulator with Pyrosim it is not possible to assign a specific incoming air velocity value the jet fans must guarantee to the fire region, but only a volumetric flow rate they must supply through the rotational speed of their blades. On the basis of this input airflow value, depending on numerous factors such as the distance between jet fans and fire location, the tunnel height, and the number of vehicles present in the tunnel, incoming air with a specific velocity is provided at fire source. This specific velocity value can be determined only by running CFD simulations, and furthermore is also the one critical ventilation methods refer to. For all these reasons, the effect of longitudinal ventilation is deeply investigated by considering different volumetric air flow rate values, in particular $15\ \frac{m^3}{s}$, $22.5\ \frac{m^3}{s}$, and $30\ \frac{m^3}{s}$, hence starting from the nominal one used in the Virgolo up to doubling it. In this way it is possible to understand the tunnel thermal behavior variation depending on the ventilation rate, as well as if the established models used to predict the critical ventilation velocity in the case of traditional pool fires are still valid for hydrogen jet fires.

The average flow velocity detected by the burning car at fully developed motion of the air coming from jet fans, thus at 60 s from the fire ignition (twice their start-up time), is obtained referring to figures 4.3.2, 4.3.3, 4.3.4, depending on the reference ventilation rate.

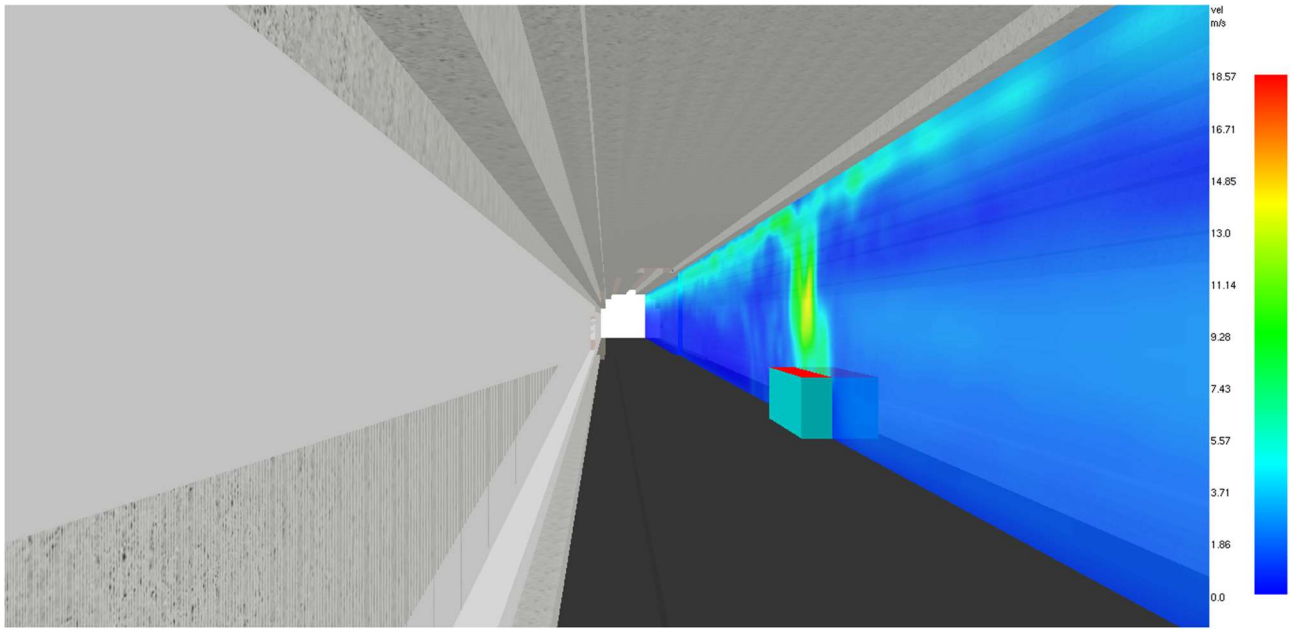

Fig. 4.3.2. 2D velocity map on plane X = 8.42 m at t = 60 s for HFCV with ventilation flow rate Q = 15 $\frac{m^3}{s}$.

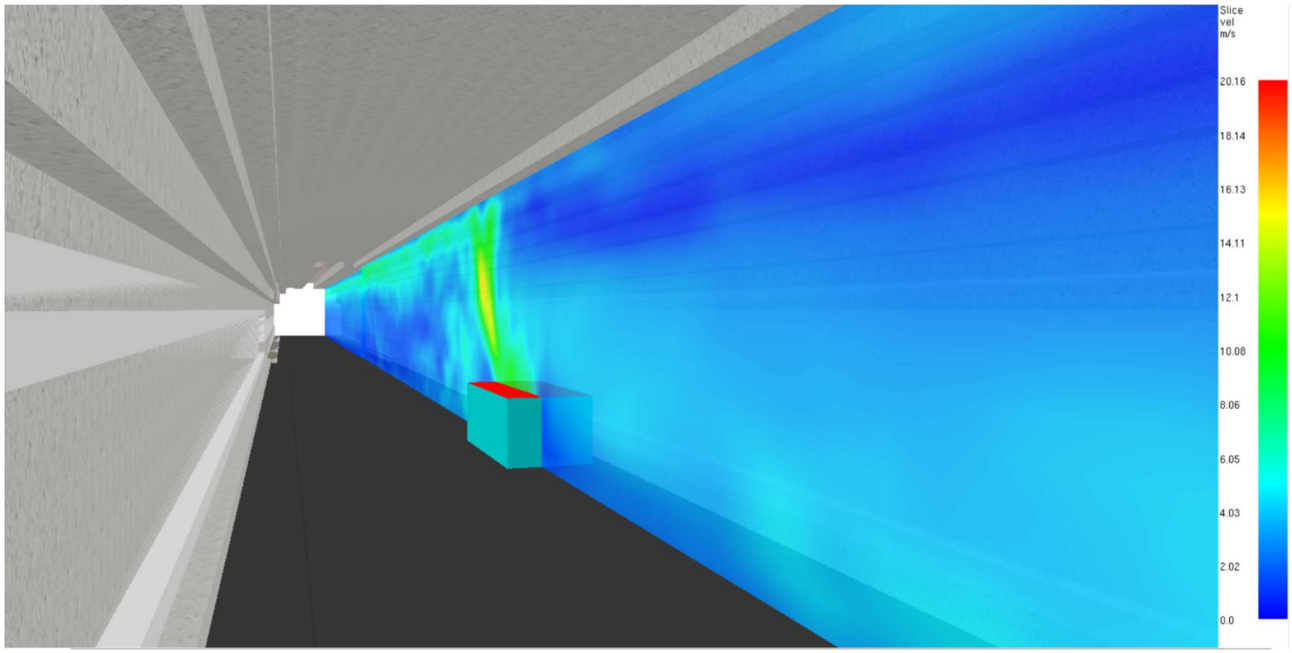

Fig. 4.3.3. 2D velocity map on plane X = 8.42 m at t = 60 s for HFCV with ventilation flow rate Q = 22.5 $\frac{m^3}{s}$.

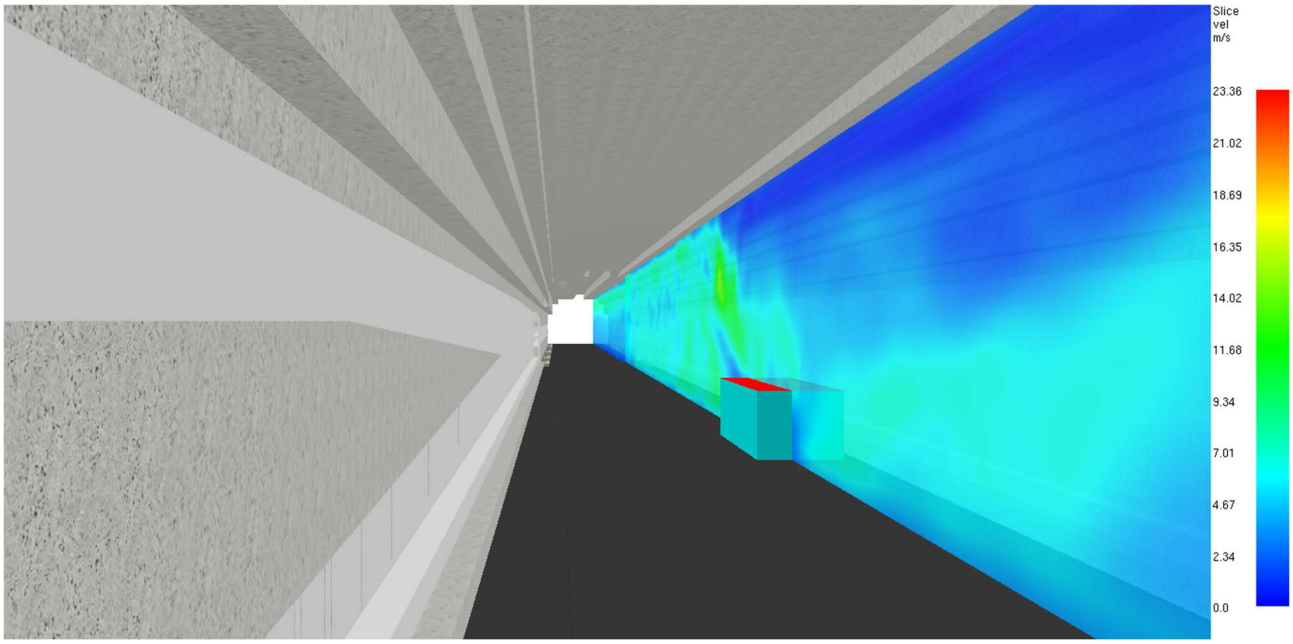

Fig. 4.3.4. 2D velocity map on plane X = 8.42 m at t = 60 s for HFCV with ventilation flow rate Q = 30 $\frac{m^3}{s}$.

The average velocity value of the incoming air to the fire location is assessed, respectively for Q = 15 $\frac{m^3}{s}$, Q = 22.5 $\frac{m^3}{s}$, and Q = 30 $\frac{m^3}{s}$, in $v = 2.2\ \frac{m}{s}$, $v = 4\ \frac{m}{s}$, and $v = 5.8\ \frac{m}{s}$. Obviously, the greater the ventilation rate the higher the flow velocity detected by the fire source, with an almost linear increase from the lowest to the highest volumetric air flow rate. The first velocity value is very close to the computed critical one, $2.49\ \frac{m}{s}$, while the other two are, respectively, about the double and triple. At this point the temperature distribution on the longitudinal plane section of the road tunnel at different instant of time during the transient, for all the three different ventilation rates under investigation, is reported.

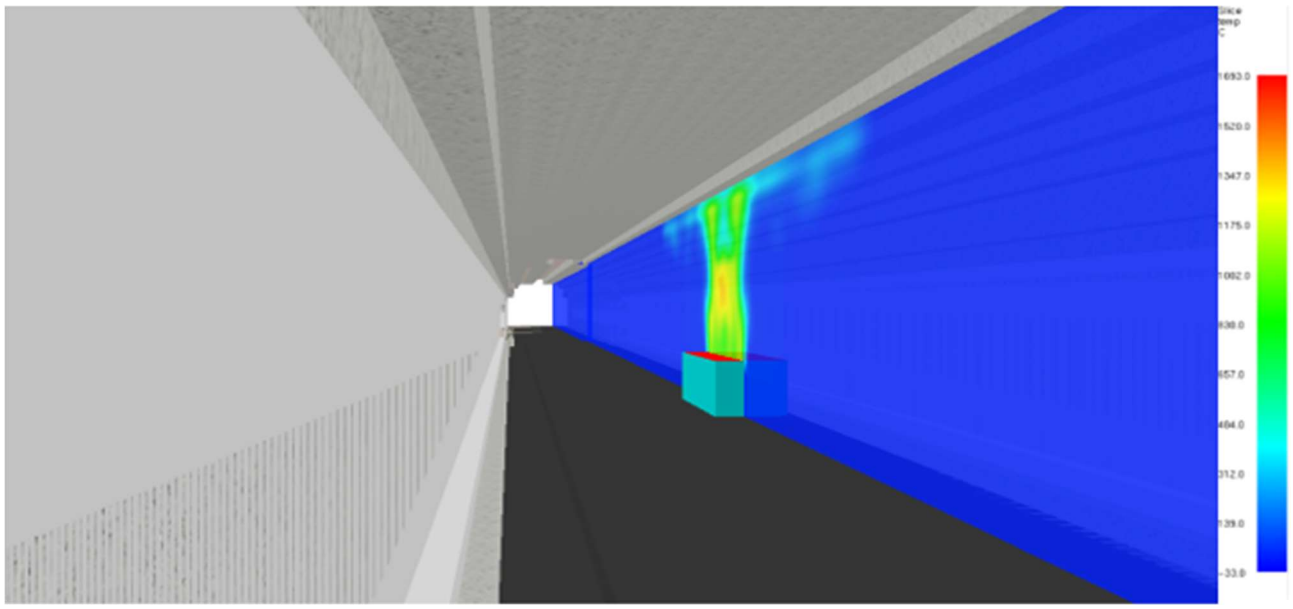

Fig. 4.3.5. 2D temperature map on plane X = 8.42 m at t = 5 s for HFCV with ventilation flow rate Q = 15 $\frac{m^3}{s}$.

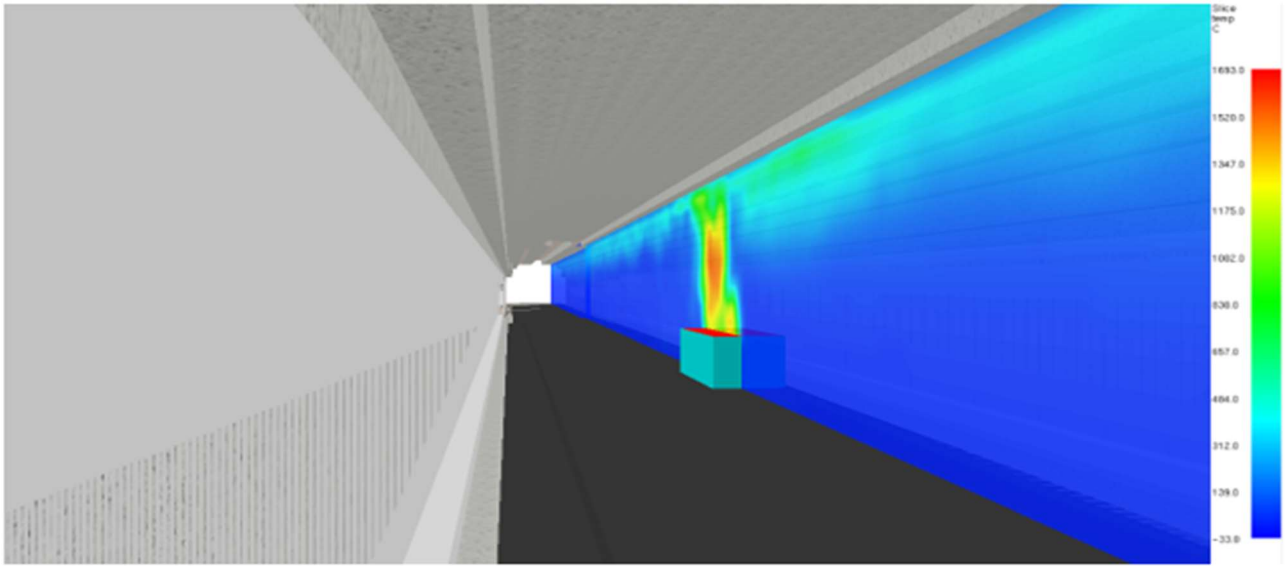

Fig. 4.3.6. 2D temperature map on plane X = 8.42 m at t = 60 s for HFCV with ventilation flow rate Q = 15 $\frac{m^3}{s}$.

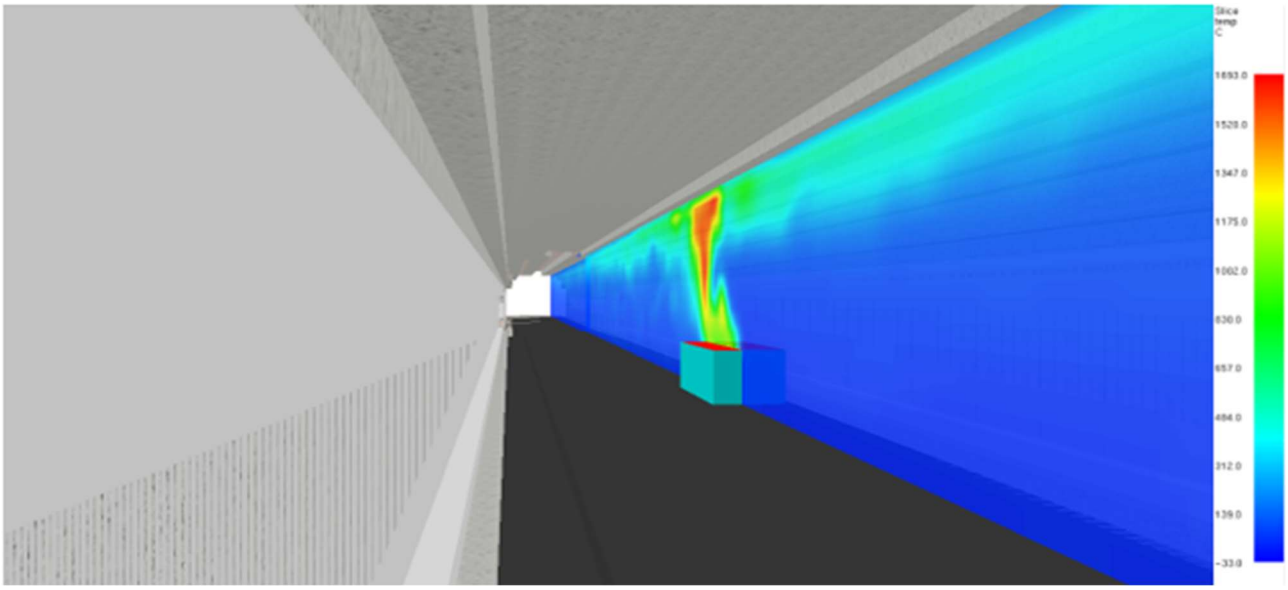

Fig. 4.3.7. 2D temperature map on plane X = 8.42 m at t = 600 s for HFCV with ventilation flow rate Q = 15 $\frac{m^3}{s}$.

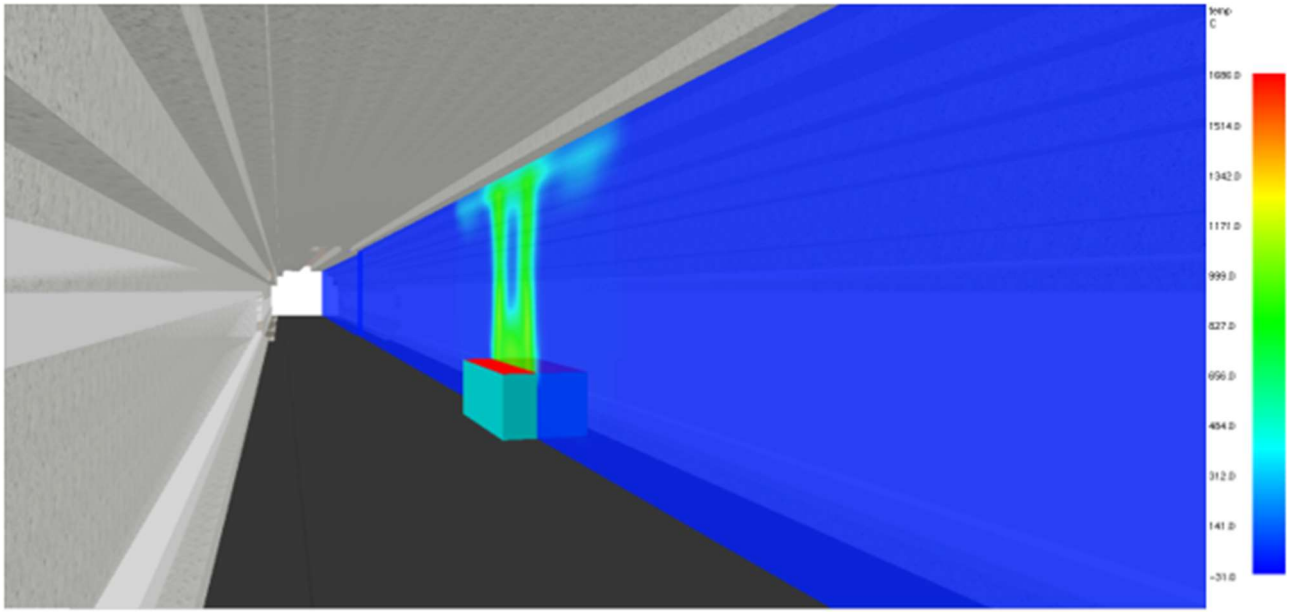

Fig. 4.3.8. 2D temperature map on plane X = 8.42 m at t = 5 s for HFCV with ventilation flow rate Q = 22.5 $\frac{m^3}{s}$.

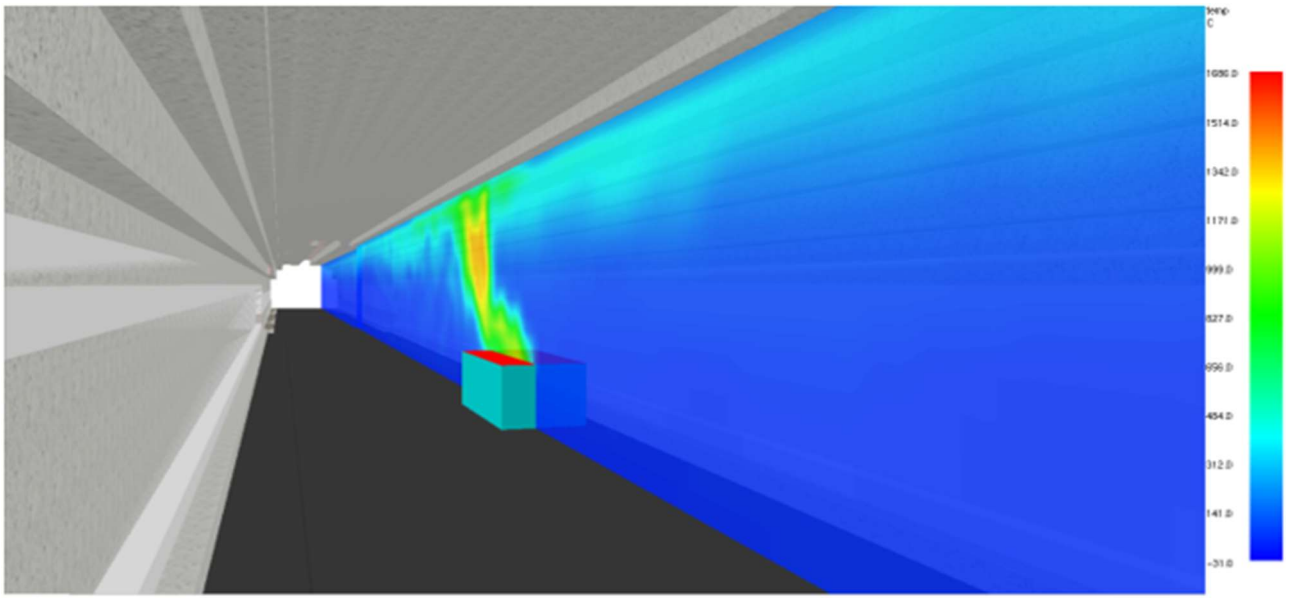

Fig. 4.3.9. 2D temperature map on plane X = 8.42 m at t = 60 s for HFCV with ventilation flow rate Q = 22.5 $\frac{m^3}{s}$.

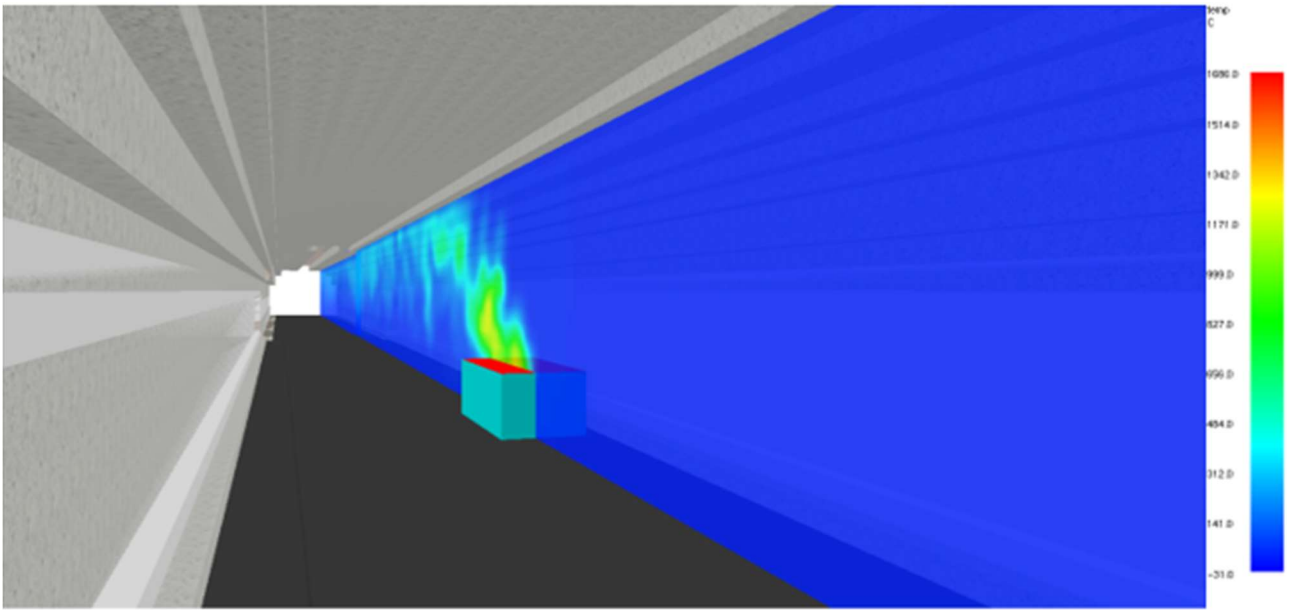

Fig. 4.3.10. 2D temperature map on plane X = 8.42 m at t = 600 s for HFCV with ventilation flow rate Q = 22.5 $\frac{m^3}{s}$.

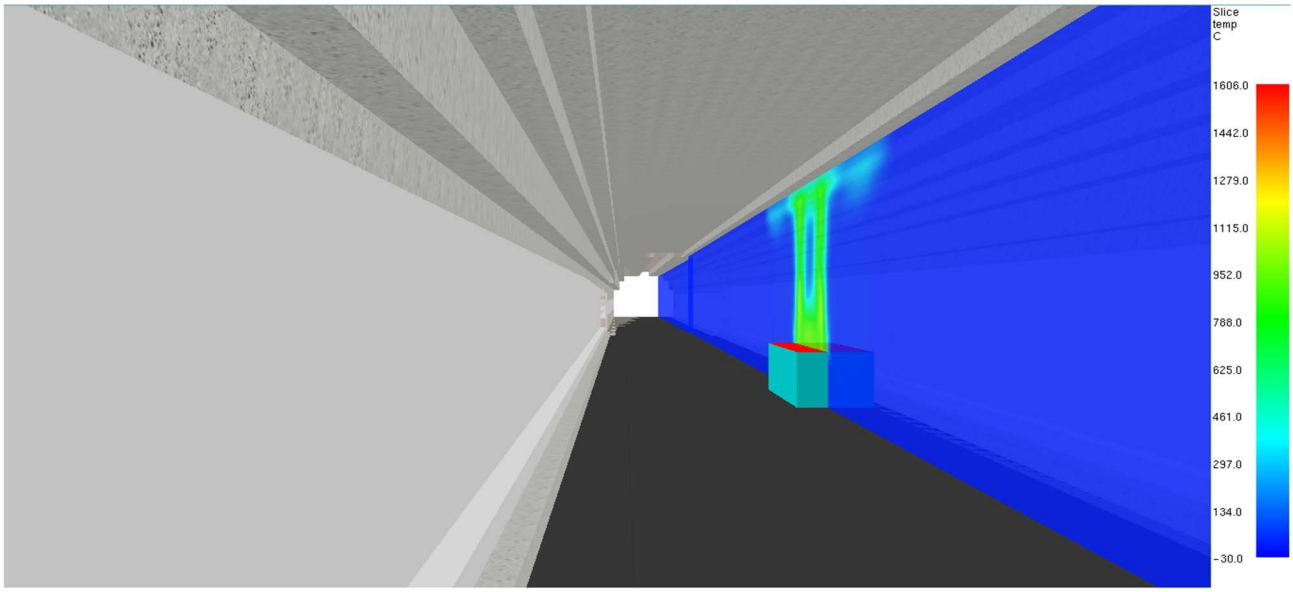

Fig. 4.3.11. 2D temperature map on plane X = 8.42 m at t = 5 s for HFCV with ventilation flow rate Q = 30 $\frac{m^3}{s}$.

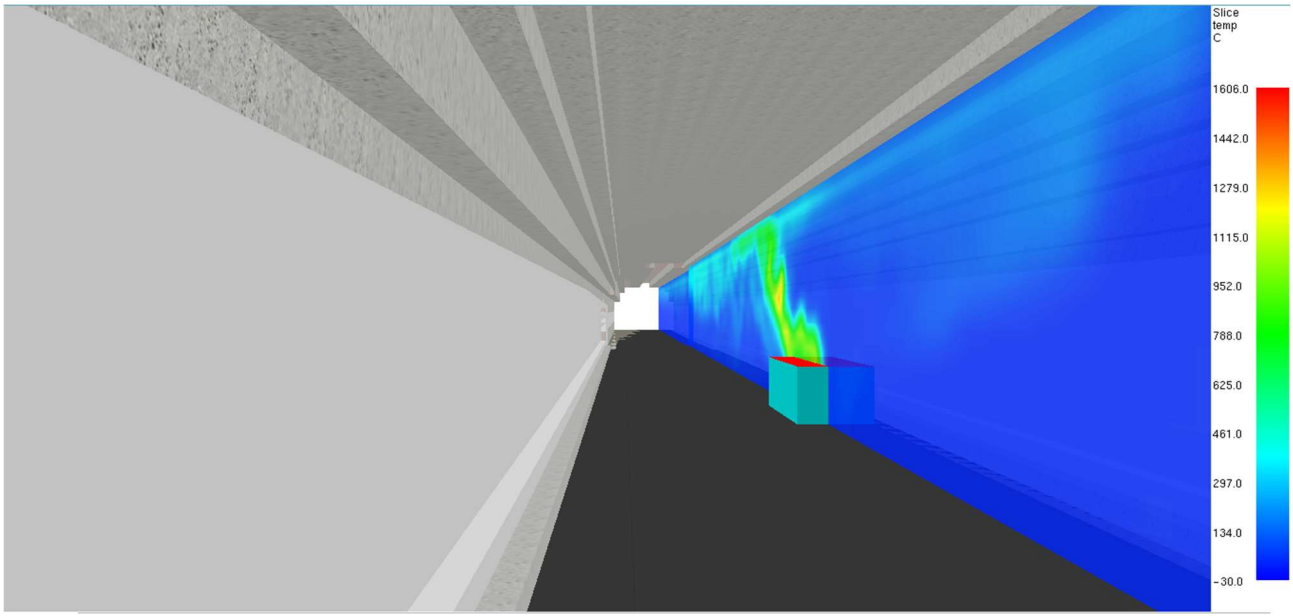

Fig. 4.3.12. 2D temperature map on plane X = 8.42 m at t = 60 s for HFCV with ventilation flow rate Q = 30 $\frac{m^3}{s}$.

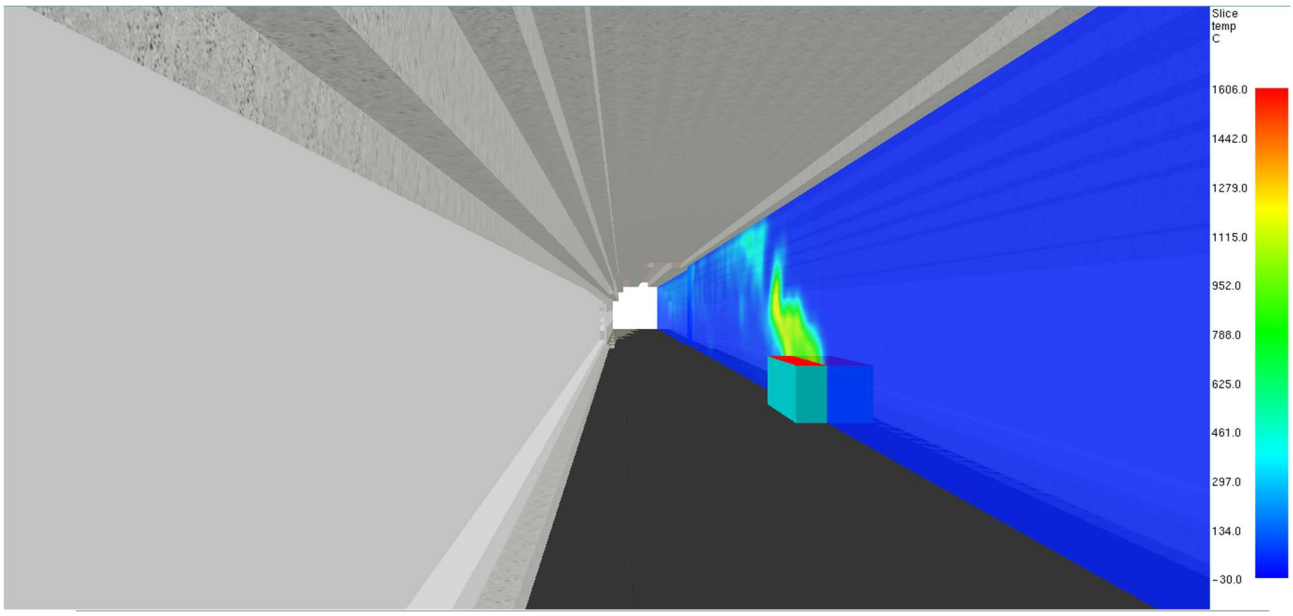

Fig. 4.3.13. 2D temperature map on plane X = 8.42 m at t = 600 s for HFCV with ventilation flow rate Q = 30 $\frac{m^3}{s}$.

As it is possible to appreciate from the previously attached 2D temperature slices evolution, the thermal plume, once arrived at the vault and bounced back, spreads in the downstream direction of the tunnel depending on the ventilation rate. Later on, it is produced a placid monodimensional thermal flow with a consequent heat stratification that, after a critical time even influenced by the jet fans start-up time, stabilises. In the case of lower air flow rates, hence lower ventilation velocities at fire source, this stratification is pretty unambiguous, while for higher ones the heat stratification is less harsh with an interface layer that is not very evident [29]. As the transient time goes by and

the ventilation rate increases, the temperature contour shape rotates in the direction of the tunnel outer section, up to reaching a sort of horizontal alignment. For longitudinal ventilation in the order of the critical velocity value computed with the model adopted for traditional pool fires (figures 4.3.5, 4.3.6, 4.3.7) the heat propagates in the tunnel both upstream and downstream, and the backlayering phenomenon occurs at whatever time during the transient. It is worth pointing out that backlayering refers to the diffusion of hot smokes in the opposite direction to that of the ventilation and travel of a one-way tunnel. With an air volumetric flow rate of 15 $\frac{m^3}{s}$ the fire scenario produced, although still better with respect to the absence of ventilation, is adverse to the tunnel abandonment by the occupants. With a such ventilation rate, in fact, the maximum temperature reached in the tunnel longitudinal plane during the combustion decreases to 1693 °C, therefore roughly 7% compared to the lack of ventilation. However, the backlayering length upstream of the fire location is not eliminated. From this consideration it results that the model proposed by Kennedy is not suitable to predict the critical velocity value in the case of hydrogen jet fires, hence it must be modified, carrying out theoretical and experimental research works on real road tunnel HFCV accidents, to accurately design the ventilation system set up. Increasing the air velocity value with respect to v_{cr}, the temperature at fully developed flow (stationary conditions) reduces up to almost reach the room temperature (initial boundary condition in all the space domain) upstream of the burning car location. The temperature peak in the longitudinal plane section X = 8.42 m, besides being spatially narrower, reduces too as a consequence of the higher ventilation flow rate, assessing to 1686 °C and 1606 °C, respectively for Q = 22.5 $\frac{m^3}{s}$ and Q = 30 $\frac{m^3}{s}$. Looking at figures 4.3.8, 4.3.9, 4.3.10, 4.3.11, 4.3.12, and 4.3.13, it is quite clear that to a higher ventilation rate it corresponds also a closer distribution of the hot gases thickness to the road tunnel ceiling, coupled with an in part riding of the downstream section and, due to the higher velocities of the combustion products, a reduction of the overall tunnel temperatures downstream. Another key result of the simulations carried out with an air ventilation rate greater than the critical one, thus with respect to the volumetric flow rate supply of 15 $\frac{m^3}{s}$, is the elimination of the backlayering. The latter occurrence, in fact, happens for both $4\ \frac{m}{s}$ and 5.8 $\frac{m}{s}$ incoming air velocity values, starting from a time equal to 60 s from the fire ignition. This time is required to bring jet fans at nominal load as well as to allow the air motion to completely develop. What hence differentiates the two simulations with Q = 22.5 $\frac{m^3}{s}$ and Q = 30 $\frac{m^3}{s}$ are the temperature values on slices reached in the road tunnel longitudinal section, smaller in the second case with respect to the other one.

To understand more the effects induced by longitudinal ventilation, in figures 4.3.14 and 4.3.15 it is reported the ceiling temperatures distribution in the road tunnel length, together with their peak values and spatial locations, as a function of the different air flow rates analysed.

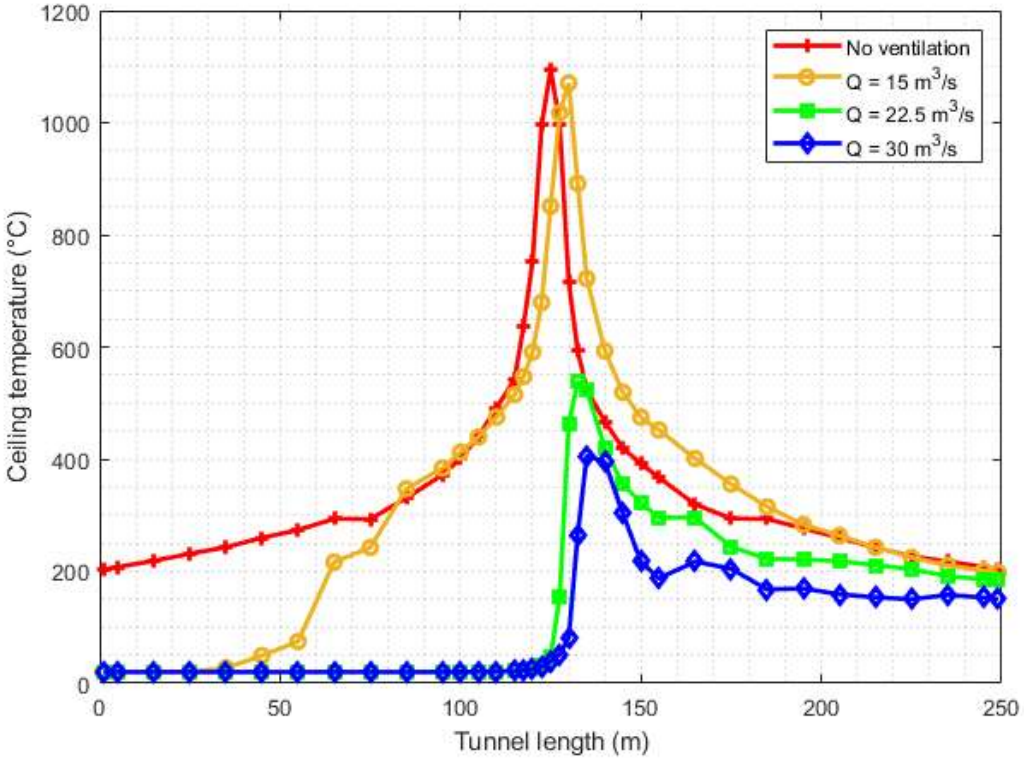

Fig. 4.3.14. Ceiling temperature distribution of the gas phase in the tunnel length at t = 300 s for HFCV for different ventilation flow rates.

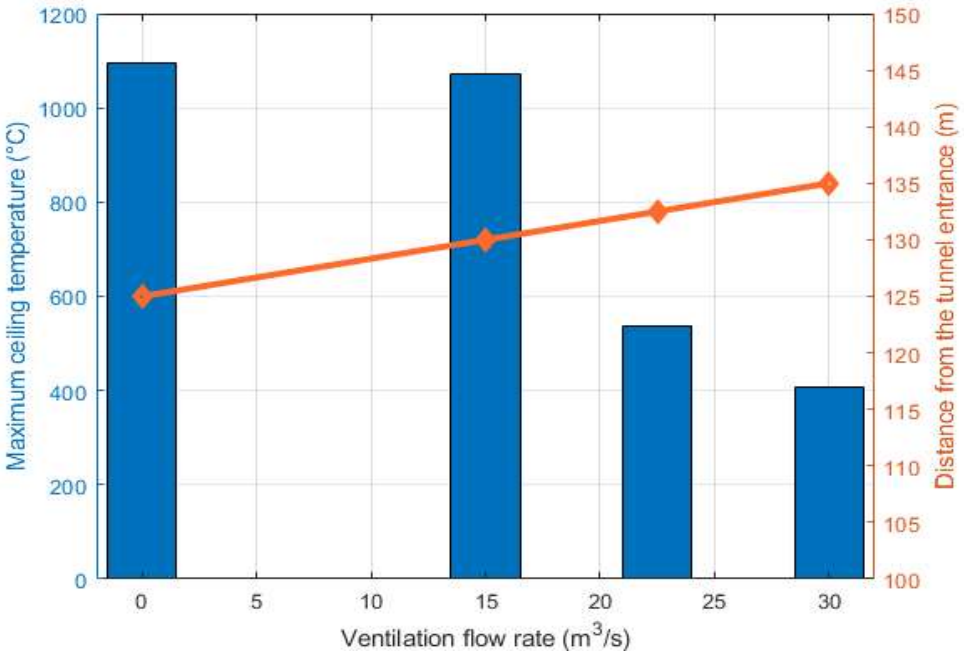

Fig. 4.3.15. Effects of ventilation flow rate on the maximum ceiling temperature and on its location at t = 300 s for HFCV.

Increasing the longitudinal ventilation velocity, due to the dilution effect, the overall ceiling temperature decreases. The ceiling temperature distribution profile in the tunnel length at fully developed flow, hence halfway through the thermal transient, is shifted towards the tunnel downstream section as the air flow rate increases, losing the symmetrical shape that characterized it in the absence of ventilation. Apart from the thermal behaviour of the downstream section, the higher the ventilation velocity the lower also the upstream ceiling temperatures, as a result of the backlayering mitigation or attenuation with hot smokes expulsion only from the outer section of the road tunnel. The maximum steady-state ceiling temperatures are computed in 1070.8 °C, 537.5 °C and 406 °C, respectively for ventilation rates of Q = 15 $\frac{m^3}{s}$, Q = 22.5 $\frac{m^3}{s}$ and Q = 30 $\frac{m^3}{s}$. The greater difference from these peak ceiling temperatures is observed moving from the lower to the intermediate air velocity value, among which it is detected a temperature difference of about half. Furthermore, the maximum ceiling temperature location moves towards downstream the more the higher the ventilation flow rate, hence pointing out the most impacted positions inside the road tunnel by high temperatures. With respect to the lack of ventilation case, in which the maximum ceiling temperature is located exactly on top of the fire source, in the other ones it is computed to be, respectively from the lower to the higher velocity value, at 130 m, 132.5 m, and 135 m from the tunnel entrance, thus increasing linearly as the flow rate increases. The determination of these locations is particularly helpful in the prediction of the activation of sprinklers and detection systems inside the tunnel.
A sum up of the main temperature variations as a consequence of the different longitudinal ventilation velocity values is available below.

Ventilation flow rate $\left(\frac{m^3}{s}\right)$	**Mean ventilation velocity at car location** $\left(\frac{m}{s}\right)$	**Maximum temperature on slices (°C)**	**Maximum steady-state ceiling temperature (°C)**
0	0	1816	1095.3
15	2.2	1693	1070.8
22.5	4	1686	537.5
30	5.8	1606	406

Tab. 4.3.2. Relevant temperatures variation following ventilation for HFCV.

Conclusions

Hydrogen fuel cell vehicles (HFCVs), which are the latest generation of electric vehicles, are spreading very rapidly in recent years, appreciably contributing to the decarbonization of the transport sector. Being a relatively new technology, for their public integration, it is necessary to deeply study the issues related to safety and management of their connected risks, especially in confined spaces such as outdoor parks or road tunnels. In fact, while in open environments an accidental hydrogen release is rapidly dispersed in the air, causing no particular concerns, in restricted ones, due to the lack of oxygen, the accumulation of hydrogen could lead to an explosion, in case of a delayed ignition, or to a hydrogen fire if an immediate ignition occurs. On this behalf, in the present work, CFD simulations through the combined use of the PyroSim software with the Fire Dynamic Simulator were carried out. The case study under investigation, which simulates the fire scenario produced by a HFCV accident in a road tunnel for a time equal to 600 s from the fire ignition, was developed taking as setting reference the 250 m long central stretch of Virgolo road tunnel, located in the autonomous province of Bolzano. The road tunnel reference model was built on the basis of its straight section map, reproduced in a 2D CAD, taking advantage of AutoCAD, and then given in input to the software Rhinoceros to create the 3D CAD Virgolo prototype. The computational domain was discretized adopting a non-uniform mesh, resulting in 950000 cells having a base size of 0.25 m in the fire region, and 0.5 m elsewhere. The car model considered as paradigm to analyse the hydrogen fire related safety hazards was the Mirai, a HFCV produced by Toyota. To make reference with respect to fire scenarios of traditional fossil fuels powered vehicles, simulations of accident on a gasoline car were also conducted. In particular, to model the power deposition, heat release rates of 24.5 MW and 7 MW, respectively for the hydrogen jet fire and traditional pool fire, were considered, with required growth stage times assessed in, respectively, 5 s and 164 s.

The simulations carried out shown that the ceiling temperatures in the case of hydrogen jet fires, as a consequence of a greater heat release rate, are much larger with respect to traditional pool fires, bringing higher fire connected hazards such as the crumbling of the tunnel lining. HFCV based simulation depicted a maximum ceiling temperature, in the almost steady-state part of the transient, of 1175 °C, as compared to 450 °C for traditional fossil fuels powered car fire scenario. Besides the ceiling ones, the overall temperatures in the longitudinal and transversal planes passing through the vehicle location are also higher, with peaks of 1816 °C (longitudinal plane section) and 1814 °C (cross plane section) in regard to 1226 °C (longitudinal plane section) and 1143 °C (cross plane section) observed instead for the traditional pool fire. Moreover, these temperature peaks are also spatially narrower and distributed close to the car top surface for gasoline car fire scenario, with respect to the hydrogen fire one in which they are instead located in the so called reaction zone, at middle-high heights with respect to the tunnel ground level. On the other hand, due to the large amount of carbon contained in the gasoline but absent in the HFCV fuel, i.e. gaseous hydrogen, the traditional pool fire characterizes itself for a greater soot production during the combustion process. This obviously reflects even on the visibility distance inside the road tunnel, considerably lower, especially at low heights, with respect to the hydrogen jet fire case. In the last part of the work, the adoption of a longitudinal ventilation strategy for the HFCV fire, through the installation of Jet-Foil 71 K jet fans, was deeply investigated. It turned out that the traditional models used to

compute the critical ventilation velocity in the case of fossil fuels powered cars fire cannot be adopted to accurately predict even the critical velocity for hydrogen jet fires based simulations. In these lasts, in fact, the required air volumetric flow rate to be supplied to the fire source to eliminate the backlayering phenomenon, thus facilitating the tunnel abandonment, is always greater than the predicted value from theoretical equations, with in particular a minimum air velocity flow estimated in about $4\ \frac{m}{s}$. The longitudinal ventilation has the positive effect of reducing the thermal behavior of the tunnel, minimizing the impacts of the generated heat and smoke during the transient. Increasing the ventilation rate from the nominal one adopted in the Virgolo road tunnel up to doubling it, the maximum steady-state ceiling temperature reduces from 1070.8 °C to 406 °C, further moving its location towards the downstream section of the tunnel as the ventilation velocity becomes greater, i.e. placing, respectively for an air flow rate of 15 $\frac{m^3}{s}$ and 30 $\frac{m^3}{s}$, at 130 m and 135 m from the tunnel entrance.

Bibliography

[1] Pierluigi Leone, Energy Networks course lecture notes, 2022.

[2] SNAM, The hydrogen challenge: the potential of hydrogen in Italy, 2019.

[3] IEA, Hydrogen, 2022.

[4] IEA, World Energy Outlook 2020, 2020.

[5] Hydrogen-news.it, The critical role of hydrogen in the energy transition, 2021.

[6] H2-South Tyrol hydrogen center by IIT, Imagebroschure H2.

[7] Cummins, Five key questions about the next hydrogen injection: hydrogen fuel cells, 2019.

[8] Toyota, New Mirai-hydrogen in its best form.

[9] Close-up Engineering, Fuel cell vehicles: what you need to know about hydrogen and the myths to dispel, 2020.

[10] Close-up Engineering, Hydrogen, The world of storage in fixed and mobile applications, 2020.

[11] Najjar, Y.S., Hydrogen safety: Them Road toward green technology, 2013.

[12] Brock Virtue, Javad Mohammadpour, Fatemeh Salehi, Rouzbeh Abbassi, Safety Assessment of Hydrogen Jet Fire Scenarios within Semi-Confined Spaces, 2023.

[13] HSE. Safety Excellence in Energy Series, In Proceedings of the Safe Net Zero 2021—Hydrogen, 2021.

[14] William G. Houf, Greg H. Evans, Erik Merilo, Mark Groethe, Scott C. James, Releases from hydrogen fuel-cell vehicles in tunnels, 2011.

[15] LaChance J, Houf W, Middleton B, Fluer L., Analysis to support development of risk-informed separation distances for hydrogen codes and standards, 2009.

[16] Codescu Silviu, Panaitescu Valeriu, Popescu Daniela, Chisacof Alexandru, Anghel Ion, Serban Manuel, Study and Improvement of Road Tunnels Fire Behavior using Pyrosim, 2014.

[17] Fire Safety Engineering Italia, Equazioni del moto e procedura risolutiva adottata da FDS, 2022.

[18] R.G. Rehm and H.R. Baum, The Equations of Motion for Thermally Driven, Buoyant Flows, 1978.

[19] NIST, FDS Technical reference guide, 2022.

[20] Ing. Carlo Costa, La galleria Virgolo: caratteristiche strutturali e impiantistiche, 2014.

[21] Ing. Carlo Costa, Piano emergenza gallerie di A22, 2014.

[22] ISPRA ambiente, Caratterizzazione morfologica delle Alpi, 2014.

[23] Serena Minucci, Relazione tra la conducibilità termica e le caratteristiche fisiche meccaniche delle terre, 2020.

[24] Fuh-Sheng Shieu, Kuen-Chang Lin, Jen-Chyang Wong, Microstructure and adherence of porcelain enamel to low carbon steel, 1999.

[25] Centro studi naturalistici, Petrolio – origine e composizione, 2020.

[26] Toyota Motor Italia, Mirai MY23, Scheda Tecnica, 2021.

[27] Karan Bhuwalka, Frank R. Field, III, Robert D. De Kleine, Hyung Chul Kim, Timothy J. Wallington, and Randolph E. Kirchain, Characterizing the Changes in Material Use due to Vehicle Electrification, 2021.

[28] Andrea Dusso, Stefano Grimaz, Ernesto Salzano, Rapid Estimation of the Heat Release Rate of Combustible Items, 2016.

[29] Yongliang Xie, Na Lv, Xujiang Wang, Dejian Wu, Shimao Wang, Thermal and fire characteristics of hydrogen jet flames in the tunnel at longitudinal ventilation strategies, 2021.

[30] Shibani, Fatemeh Salehi, Til Baalisampang, Rouzbeh Abbassi, Numerical modeling towards the safety assessment of multiple hydrogen fires in confined areas, 2022.

[31] Yongliang Xie, Na Lv, Yan Huang, Dejian Wu, Liang Gong, Xufeng Yang, Yikai Zeng, Comparative analysis on temperature characteristics of hydrogen-powered and traditional fossil-fueled vehicle fires in the tunnel under longitudinal ventilations, 2022.

[32] M. K. Cheong, M. J. Spearpoint, C. M. Fleischmann, Design Fires for Vehicles in Road Tunnels, 2008.

[33] Thunderhead engineering, PyroSim User Manual, 2012.

[34] J. Burri, R. Crockett, R. Hany, Gasoline composition determined by ^{1}H NMR spectroscopy, 2004.

[35] Agency for Toxic Substances and Disease Registry, Toxic Substances Portal.

[36] Mukesh Singh Tomar, Shashank Khurana, Investigation of road tunnel fires: challenges and findings, 2019.

[37] United States Nuclear Regulatory Commission, Verification and Validation of Selected Fire Models for Nuclear power Plant Applications (NUREG-1824), 2007.

[38] Law CK, Combustion physics, 2010.

[39] Junmei Li, Yang Tian, Yanfeng Li, Yuhang Zhao, and Youbo Huang, Numerical and Experimental Study on the Effects of the Slope on the Critical Velocity in Titled Tunnels, 2017.

[40] FläktWoods, Jetfoil & Large JM Aerofoil Fans For Tunnel Ventilation.